The Route to Chaos and Turbulence in Annular Electroconvection

by

PEI-CHUN TSAI

A thesis submitted in conformity with the requirements
for the degree of Doctor of Philosophy
Graduate Department of Physics
University of Toronto

Abstract

The Route to Chaos and Turbulence in Annular Electroconvection

PEI-CHUN TSAI

Doctor of Philosophy

Graduate Department of Physics

University of Toronto

2007

Convection is essential and ubiquitous in Nature. For a century, classical thermal convection, or Rayleigh-Bénard convection, has been a central paradigm for laboratory studies. This thesis concerns an electrical analogue of Rayleigh-Bénard convection — electroconvection in a thin fluid film. This complementary system was studied with a combination of experiment, theory, and numerical simulation. The fluid film is driven to convect by a critical applied electric potential interacting with a charge inversion, in direct analogy with the buoyancy inversion that drives thermal convection. As the imposed voltage is increased, electroconvection proceeds from steady, laminar patterns through time-dependent flows and eventually into chaotic and turbulent regimes. The experimental procedure consisted of precise measurements of current-voltage (IV) characteristics when a DC voltage was applied to an annular film between two concentric electrodes. The onset of convection was found by a change in the slope of the IV curve; unsteady flow was indicated by a large increase in current fluctuations. From the IV measurements, the corresponding dimensionless charge transport, or Nusselt number Nu, was determined as a function of the electric forcing, characterized by the dimensionless Rayleigh number $\mathcal{R}$. A power-law relationship $Nu \sim \mathcal{R}^{\gamma}$ was observed in the turbulent convection regime when $\mathcal{R} \gtrsim 10^4$. The influence of the annular geometry, characterized by aspect ratio Γ, on this scaling was investigated. A scaling theory was developed which explains the power law and its

dependence on Γ. The corresponding theory for thermal convection does not account for this Γ dependence. In addition, a direct numerical simulation was constructed using a pseudo-spectral method, based on realistic governing equations. The simulation affords deep insights into the flow dynamics, charge distribution and electric potential of the electroconvection instability and its route to turbulence, including for the case of an externally applied shear.

Acknowledgements

Contents

List of Tables

List of Figures

x

Chapter 1

Introduction

In nature, nonlinear and nonequilibrium processes are so pervasive that they shape a great variety of phenomena. Examples are abundant and ubiquitous; ocean circulation, mantle convection, sand avalanches, earthquakes, food chain cycles in ecosystems, the formation and decay of stars, and many more. The realm of nonequilibrium nonlinear dynamics is interdisciplinary, where physics melts with chemistry, geology, biology, zoology, astronomy, and social science.

To gain some insight at a more controllable level, diverse laboratory studies have been undertaken. The common scenario for these investigations is that a nonlinear, dissipative system is driven out of equilibrium by an experimentally accessible parameter, the so-called *control parameter*. The parameter, for example, can be a temperature difference, a mechanical stress, an electric voltage, or a chemical concentration; it varies for different systems. Under weak driving, the system responds linearly. At a critical value of the parameter, the system undergoes a transition to a new state associated with symmetry breaking, often with some form of spatial or temporal structured pattern emerging. The pattern is the consequence of a developed instability dictated by the nonlinear processes in the system. At an even higher value of the control parameter, secondary instabilities set in, usually involving more

complex patterns that may display spatio-temporal intermittency. Eventually, at a very large parameter value, the system is driven to a chaotic state and successively to a highly nonlinear regime. Ultimately, a turbulent state is reached, and this state remains one of the most important, long-standing unsolved problem in physics.

Convection in fluid dynamics, which conforms to the aforementioned scenario, has long been a playground for researchers of nonlinear dynamics and pattern formation, because of its rigorous mathematical description and the possibility of accurate experimental measurement [2, 3]. Prototypical experiments include Rayleigh-Bénard convection in a pure fluid or binary-fluid mixture [2, 4], Bénard-Marangoni convection [5], Taylor-Couette flow [6], and electrohydrodynamic instability in dielectric liquids and nematic liquid crystals [7]. Recently, highly controlled experiments, accurate simulations, and theoretical analyses have been combined to give a more complete picture of the flow dynamics, particularly in the weakly nonlinear regime [3]. The accumulation of complexity as the driving forces are increased presents an important route to chaotic and eventually to fully turbulent flow. Turbulence—involving strongly chaotic eddies of a variety of sizes that often work in a coherent way—plays a vital role in efficient energy and momentum transfer [8].

The topic of this thesis is a unique convection system, which has several control parameters that can be varied over wide ranges and takes place in two-dimensional annular geometry, complementary to previous convection studies. The laboratory system consists of a thin, weakly conducting, freely suspended, annular liquid crystal film between two concentric electrodes. The film is driven out of equilibrium by a radial electrical force and can simultaneously be driven by an imposed laminar shear flow, made by rotating the inner electrode (see Fig. 1.1). When a small voltage is applied across the film, there is no flow motion due to dissipation, i.e. the diffusion of charge and momentum. At a sufficient voltage drop, the film undergoes a transition from quiescence to convection and a structured pattern emerges. This phenomenon
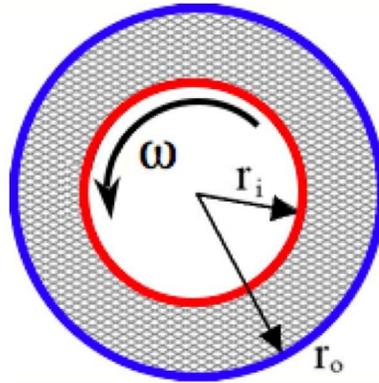
Figure 1.1: A sketch of annular electroconvection under a radial electric force and an azimuthal shear: a liquid crystal thin film suspended between two concentric electrodes, which consists of an anode at the inner radius r_i and a cathode at the outer radius r_o. The film is a thin sheet that occupies the annular area of the film width $d = r_o - r_i$ and extends in the direction normal to the page with the film thickness s. The shear is experimentally generated by rotating the inner anode with an angular rotation frequency ω.

is called electroconvection. As the voltage is gradually increased, flows successively become steady, unsteady, and then turbulent. In this thesis, a combination of experimental, analytical, and numerical tools was employed to understand the various nonlinear stages that electroconvection subsequently undergoes as the electric forcing is increased. Before entering into a more detailed description of electroconvection, and to put the work in context, it is useful to discuss the paradigm case of thermal convection, the topic of next section, to introduce the general feature of convective instability.

1.1   Thermal convection

Thermal or *Rayleigh-Bénard* convection is a classic case of pattern formation and involves the buoyancy-driven instability of a confined viscous fluid heated from below. It has inspired and attracted numerous studies since the first investigation by Henri Bénard in 1900 [9, 10]. The main experimental control parameter is the imposed

temperature difference across the fluid layer, which is parameterized by the dimen-sionless Rayleigh number Ra. Ra describes the strength of the driving force relative to viscous effect and thermal diffusion in a dimensionless form. The other accessible parameters are the Prandtl number Pr and the aspect ratio Γ; Pr is a fluid property, equal to the ratio of kinematic viscosity to thermal diffusivity; Γ describes the ge-ometry of the fluid cell and is defined as the ratio of lateral to vertical dimensions. Stated mathematically, these characteristic dimensionless parameters are [11]:

$$\text{Ra} = \frac{\beta g \Delta T L^3}{\nu \kappa}, \qquad \text{Pr} = \frac{\nu}{\kappa}, \qquad \Gamma = \frac{D}{L}, \tag{1.1}$$

with β the coefficient of thermal expansion, g the magnitude of the gravitational acceleration, ΔT the temperature difference between the top and bottom horizontal plates, L the height of the cell, ν the kinematic viscosity, κ the thermal diffusivity, and D the lateral dimension of the cell. The heat transfer through the fluid layer is measured by the dimensionless Nusselt number Nu, which is the ratio of the total heat flux J to the conductive heat flux J_c:

$$\text{Nu} = \frac{J}{J_c}. \tag{1.2}$$

The convective instability stems from the buoyancy that lifts the warmer—and thus lighter—parcels of fluid, due to thermal expansion. Simultaneously, the cooler parcels of fluid fall to the bottom of the layer and complete the circulation. Fig. 1.2 schematically illustrates this instability mechanism. At low ΔT, dissipation effects balance the energy input and there is no fluid motion, the heat being transported across the layer by conduction, so that Nu = 1. At a threshold temperature differ-ence, the fluid displays a transition from the quiescent state to a laminar flow in a pattern of cellular motion. At this critical and minimum value of the temperature
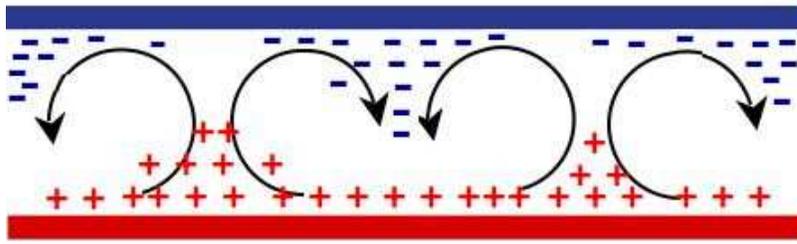
Figure 1.2: A diagram of instability to convection: Rayleigh-Bénard convection occurs in a viscous fluid layer which is heated from below and cooled from above under a gravitational field pointing downwards. The warmer fluid near the bottom (indicated by (+) signs) is less dense than the cooler fluid near the top (indicated by (−) signs); buoyancy forces therefore act to invert the fluid. For electroconvection, an inversion of charge density, corresponding to the positive charges (+) near an anode and negative charges (−) close to a cathode, is unstable to the applied electric field pointing upwards.

gradient, the conducting state becomes unstable to perturbations to the fluid velocity. The corresponding critical Rayleigh number $\mathrm{Ra_c}$ depends on the boundary conditions on the fluid in the convection cell. $\mathrm{Ra_c}$ is approximately 1708 for rigid boundary conditions in a confined fluid box [11]. Convection sets in under a smaller critical temperature difference in a cell with free top surface than in a confined container. As the temperature difference is gradually increased, the fluid undergoes successive bifurcations to periodic oscillations [12], chaotic motion [13], and finally a turbulent state [14]. Many routes or transitions to turbulence have been revealed by experimental measurements of the local velocity and temperature fields. For example, one can observe sub-harmonic bifurcations, intermittent non-periodic motions, quasi-periodic motions of two frequencies that lead to phase locking, and quasi-periodic states characterized by three distinct incommensurate frequencies [13, 15, 16, 17]. Some of these scenarios have been predicted by simple mathematical models and numerical studies with highly truncated normal mode expansions. However, the complicated dependence of scenarios on Γ, Pr, and the mean flow structure is still not well understood [13, 18, 19, 20, 21]. In this thesis, the route to chaos will be explored in the

context of electroconvection.

Turbulent Rayleigh-Bénard convection has been the central paradigm for studies of convective turbulence for about a century. Turbulent convection is ubiquitous in the transfer of energy and heat in the natural world. Much interest in turbulent thermal convection has focused on the efficiency of heat transport because of its important applications in the atmosphere, in ocean, and in stars [14]. Experiments on turbulent Rayleigh-Bénard convection have revealed power laws in the heat transport with the Rayleigh number, in the form $Nu \sim Ra^{\gamma}$. Earlier experiments in air cells showed $\gamma = 1/4$ for relatively small Rayleigh numbers $Ra \lesssim 10^8$ [22, 23]. Later, experiments in water cells with larger Ra were conducted and the power-law exponent γ was found to be larger than $1/4$. Meanwhile, a theoretical marginal stability model predicted $\gamma = 1/3$ [24], which seemed to describe these experimental results. In the late 1980s, more experiments and numerical simulations revealed γ very close to $2/7$, and theoretical models, based on different assumptions, tried to explain this "2/7-scaling" [25, 26, 27]. More recently, a variety of empirical data suggests that the Nu scaling law in the turbulent regime deviates from one single power law and is a more complex function of Rayleigh number Ra, Prandtl number Pr, and aspect ratio Γ, so that $Nu = f(Ra, Pr, \Gamma)$. The key problem then is to understand the dependence f.

In the past decade, as the precision of experimental data has improved, there have been some promising advances in theoretical, numerical, and experimental studies in turbulent Rayleigh-Bénard convection [28]. High precision Nu measurements showed that Nu scaling deviates from a single power-law description [29]. Moreover, Pr dependence of Nu measurements is not consistently accounted for by some existing models [30, 31]. A recent theory by S. Grossmann and D. Lohse, in 2000, systematically predicted various Nu "local" power laws depending on the Ra and Pr parameter regime, and addressed the discrepancies mentioned above [32]. The main idea of Grossmann-Lohse theory is to deduce simple scalings by decomposing

the global thermal and viscous dissipation rates into bulk and boundary layer contributions. Their predictions have been shown to be in a good agreement with much experimental data over a wide parameter range [32, 33]. In this thesis, this scaling theory was adapted for electroconvection in thin films to investigate the relevant Nu scaling, as described in Chapter 4.

Many attempts have been made to better understand turbulent Rayleigh-Bénard convection through experiment, theory, and numerical simulations. Yet turbulent Rayleigh-Bénard convection still remains a fascinating phenomenon with many unresolved problems. So far, the study of turbulent Rayleigh-Bénard convection has mostly focused on $\Gamma \approx 1$, i.e., the geometry of the system has comparable lateral to vertical length scales. In particular, large aspect ratio Rayleigh-Bénard convection experiments have seldom been performed since it is difficult to achieve the strong forcing that is readily reached in $\Gamma \approx 1$ cells. Nevertheless, in nature various systems undergoing turbulent convection extend laterally and have large aspect ratios. As described in detail in Chapter 2, the smectic electroconvection experiment easily allows large aspect ratios with no lateral boundaries.

The next section returns to the discussion of the main subject of this thesis, an electrical analog of Rayleigh-Bénard convection. Many features of Rayleigh-Bénard convection carry over to this new system.

1.2 Electroconvection in thin smectic films

If the transport of heat and the buoyancy force in Rayleigh-Bénard convection are replaced by the transport of electric charge and the electric body force under an applied electric field, the corresponding phenomenon is called *electroconvection*. Similarly, the charge density inversion in electroconvection is akin to the fluid mass density inversion in Rayleigh-Bénard convection; see Fig. 1.2 for a schematic of the analogous insta-

bilities. Unlike the normal, electrically neutral fluids in Rayleigh-Bénard convection, electroconvection experiments often use special working fluids, such as dielectric fluids or liquid crystal materials, which has special electrical properties to facilitate charge transport. The subject of this thesis is only concerned with electroconvection in a two-dimensional smectic liquid crystal film which is isotropic in the plane of the film. This material is different from nematic liquid crystals that are often studied in elec-trohydrodynamic convection and in which the electric driving mechanism relies on the dielectric anisotropy of the materials [7].

Originally, smectic electroconvection was studied with a film suspended in a rect-angular frame [34], as depicted in Fig. 1.2. The suspended film was about $\sim 0.1 \mu m$ thick with free top and bottom surfaces. Convection patterns were observed under a sufficiently high DC voltage or a low-frequency AC voltage by suspending small dust particles in the thin film. As the voltage difference between the wire electrodes was slowly increased from zero, particles which were initially quiescent began to move. The initiation of particle movement was associated with the onset of electroconvection and this critical voltage V_c was measured. At a voltage drop larger than V_c, particles swirled in an array of counter-rotating vortex pairs. The wavelength of these circula-tion pairs was found to be ~ 1.3 times the film width. These early electroconvection experiments studied the dependence of the critical voltage V_c on the film thickness and width. It was observed that V_c increased linearly with the film thickness and was weakly dependent on the film width. Moreover, hysteresis in V_c was not observed when voltage was decreased [34]. In a convecting state, flow velocity was measured by tracing particle movement. However, these crude measurements were qualitative because the tracer particles had a size comparable to the film thickness and affected the electric properties of the film. Thus, direct flow visualization was rather limited.

Subsequently, a rigorous mathematical model that explained electroconvection in-stability was developed [35]. A linear stability analysis was carried out to predict the

critical voltage for onset of convection for various fluid parameters [36]. The electro-convection cell used in the experiment was changed to have an annular shape with a radial DC electric voltage, so as to perform accurate current measurements [37]. Fig. 1.1 shows the setup for annular electroconvection. Compared with a rectangular cell, an annular cell has the advantage that it is free of electric leakage through the lateral boundaries. The imposed shear, which is easily controllable by rotating the inner electrode, offers another advantage.

In annular electroconvection, there are several experimentally accessible control parameters. Their dimensionless forms describe the state of the system. $\mathcal{R}$, the analog of the Rayleigh number in Rayleigh-Bénard convection, is the external driving parameter, and is proportional to the square of the applied voltage. $\mathcal{P}$, the analog of the Prandtl number in Rayleigh-Bénard convection, is the ratio of the charge to viscous relaxation time scales in the film. The annular geometry is uniquely characterized by the radius ratio α. In analytical terms, they are [38]

$$\mathcal{R} = \frac{\epsilon_0^2 V^2}{\sigma \eta s^2}, \qquad \mathcal{P} = \frac{\epsilon_0 \eta}{\rho \sigma s d}, \qquad \alpha = \frac{r_i}{r_o}, \tag{1.3}$$

with ϵ_0 the permittivity of free space, V the applied voltage, σ the bulk electrical conductivity, η the shear viscosity, ρ the mass density of the fluid, s the film thickness, d the film width, and r_i and r_o the inner and outer radii of the film, respectively.

Annular electroconvection can be subjected to an azimuthal shear and the imposed shear generates a laminar Couette flow [11] in the annulus. The strength of the shear is described by the dimensionless Reynolds number Re, which is proportional to the angular rotation frequency $\boldsymbol{\omega}$ applied to the inner electrode:

$$Re = \frac{r_i \boldsymbol{\omega} d \rho}{\eta}. \tag{1.4}$$

The charge transport across the film is described by the dimensionless electric Nusselt number Nu, defined as the ratio of total current I to the conductive current I_c:

$$Nu = \frac{I}{I_c},\tag{1.5}$$

analogous to the Nusselt number which characterizes the dimensionless heat transfer in Rayleigh-Bénard convection.

Previous annular electroconvection studies focused on how $\mathcal{P}, \alpha$, and Re affect the critical Rayleigh number $\mathcal{R}_c$ and on the laminar convection patterns when the electric forcing is slightly above $\mathcal{R}_c$ [37]. Experimental measurements of current-voltage (IV) characteristics, which measure Nu, were used to locate the critical voltage V_c and to monitor the the amplitude of steady convection in the weakly nonlinear regime, typically for the applied voltage $V > V_c$, but within 50 volts. The imposed shear was found to delay the onset of convection. Moreover, these IV data, compared with a phenomenological model of steady-state amplitude equations, revealed and characterized the nature of the primary bifurcation for various parameters. However, because flow visualization is difficult, no quantitative data of flow velocity field or electric potential were available although these physical fields play an essential role in understanding more complex patterns.

Chapter 3 revisits some old territory with a new approach, direct numerical simulation. A new numerical code was developed from scratch to simulate annular electroconvection, based on realistic hydrodynamic equations. Its mathematical model and numerical method are described in detail in Chapter 3. The numerical study provides for the first time the full dynamics of flow velocity, charge distribution, and electric field to understand weakly nonlinear and highly nonlinear realms in the system. The code was validated with previous experimental data and theoretical predictions in the weakly nonlinear regime, as fully discussed in Section 3.4. After the successful vali-

dation of the code, the simulations have explored sheared annular electroconvection to understand various bifurcations observed in previous IV data which, however, had no flow visualization.

New research territory—particularly the higher Rayleigh number regime—in annular electroconvection has been explored. With the applied voltage up to 1000 volts, the voltage-current scaling was discovered for the first time in smectic electroconvection experiments. From these IV data under large imposed voltage, the dependence of Nu on $\mathcal{R}$, $\mathcal{P}$, and α in the high Rayleigh number, $10^4 \lesssim \mathcal{R} \lesssim 10^6$, have been studied. The ranges covered with these parameters are wider than those in previous experiments. Experimental details are discussed in Chapter 2. Furthermore, simulations have been extended for annular electroconvection to the high Rayleigh number regime for the study of convective turbulence. A theoretical treatment has been established by expanding the Grossmann-Lohse theory for turbulent thermal convection to account for the influence of annular geometry on the Nu scaling. This analytical work is described in Chapter 4. The theoretical predictions of the influence of $\mathcal{R}$, $\mathcal{P}$, and α on the Nu scaling have been compared with experimental and numerical data.

The laboratory-sized electroconvection system, with its broad range of fluid parameters and aspect ratios, can complement the conventional Rayleigh-Bénard convection experiments, especially for the study of convective turbulence. The special features of annular electroconvection—being a two-dimensional system free of lateral boundary and with easily controllable experimental parameter of shear—extend various conventional convection experiments to understand the complex, cardinal, nonlinear behavior of convective transport. The next chapter describes the experimental aspects of annular electroconvection.

Chapter 2

Experiment

This chapter first introduces the experimental materials and the convection cell, in Sections 2.1 and 2.2, respectively. Then, the later sections describe the experimental apparatus and its setup, which are designed to perform fast and precise current-voltage measurements of electroconvection in annular liquid crystal films.

The experiment comprises a two-dimensional weakly conducting, sub-micron thick, liquid crystal thin film freely suspended between two concentric electrodes. The overall structure of the experiment is schematically shown in Fig. 2.1. The experimental control parameter is an imposed DC voltage V that drives the current flow across the annular film. The key objective here is to study charge transport phenomena by measuring the current I, as it undergoes various complexity-accumulating bifurcations as the external voltage V varies.

The experimental setup is enclosed in a metallic Faraday cage to eliminate electrical noise. A CCD (charge-couple device) colour video camera is assembled with a low power microscope to view the film during the course of experiment. A Keithley high precision electrometer controlled by a computer imposes a DC voltage V and measures the resulting current I. A detailed description of the experimental design follows in Section 2.3; the experimental procedure and protocol are described in Sec-
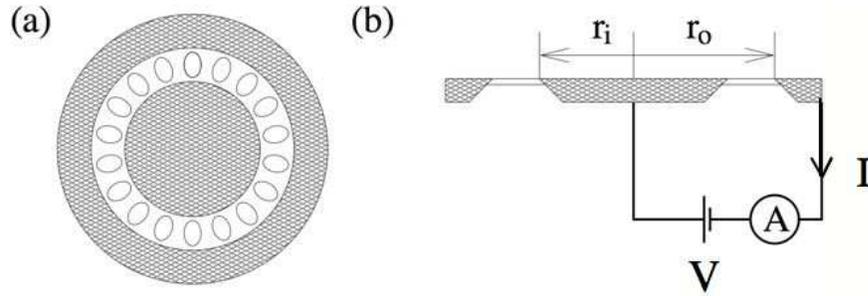
Figure 2.1: A schematic of the annular electroconvection experiment: (a) top-view and (b) side-view.

tion 2.4. The primary experimental data are discussed in Section 2.5 as well as their analyses and the underlying physics.

2.1 The liquid crystal material

The working fluid in the experiment was a liquid crystal thin film freely suspended between two concentric electrodes. The liquid crystal material employed in our experiments was 4-octyl-4'-cyanobiphenyl, hereafter referred to as 8CB, which has rod-like polar molecules. Fig. 2.2 shows the chemical formula of 8CB and its sequence of phases depending on the temperature. At a temperature lower than 21.5^o, 8CB is spatially structured as a solid crystal with long-range positional and rotational order. At the temperature higher than 40.5^o, 8CB arranges spatially randomly as a isotropic fluid with short-range order. Between these two temperatures, 8CB can exhibit short-range correlations in some directions but long-range order in others; for instance, the Smectic-A phase and the Nematic phase. These phases have symmetries intermediate between those of a crystal and a liquid [39].

The experiments were operated at room temperature $24 \pm 2°C$, thereby exploiting a property of Smectic-A phase in 8CB that the constituent molecules maintain one-dimensional ordering [40]. The molecular arrangement for Smectic-A is illustrated in
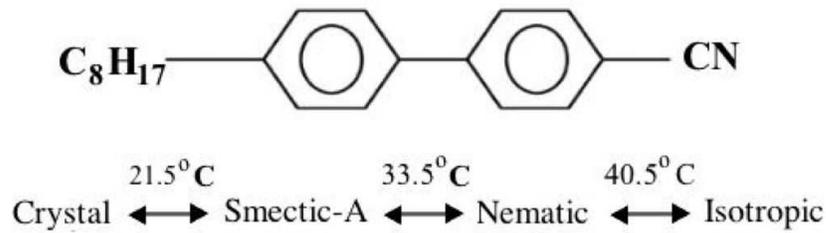
Figure 2.2: The chemical formula and phase sequence of 8CB.
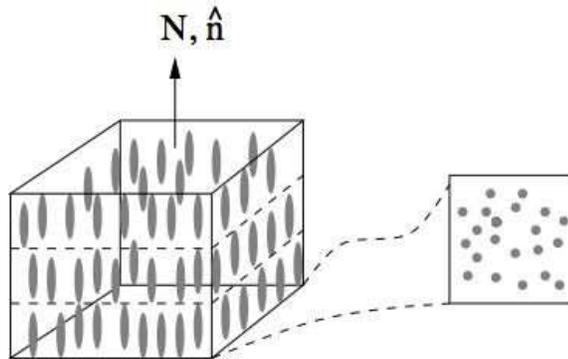
Figure 2.3: A diagram of the spatial structure of the smectic-A phase liquid crystal. The anisotropic molecules form a layered structure with an integer number of layers, and also align on average in a particular direction that is described by the so-called director $\hat{n}$. In contrast to nematic liquid crystals, the director of smectic-A phase is not a hydrodynamic variable [40]. The direction $\hat{n}$ is parallel to the normal direction to the layered planes N. In each plane, the molecules are free to move and act like a two-dimensional fluid.

Fig. 2.3. The anisotropic Smectic-A phase molecules form a layered structure of an integer number layers. Inside each layer, oriented molecules are free to move with no long-range order. Thus, each layer acts as a two-dimensional fluid. In addition, Smectic-A phase 8CB tends to form a freely-standing film which is stabilized mainly by Van der Waals attraction between the liquid crystalline molecules [41].

Pure 8CB as supplied by the manufacturer [42] has a low, uncontrolled electrical conductivity due to residual ionic impurities. Under a DC or low frequency AC voltage, electrochemical reactions at the electrodes may irreversibly destroy normal Ohmic electric conductivity, by either degrading the liquid crystal material or by

driving reactions involving the impurities [43]. To control conductivity, the 8CB was doped with tetra-cyanoquinodimethane (TCNQ) [44], a good electron acceptor. This method of using suitable dopants was commonly used in the design of dynamic scattering liquid-crystal (LC) displays, to prevent LCs from electrochemical degradation [43, 45]. The TNCQ dopants can form charge transfer complexes with the host liquid crystal and have highly reversible electrochemical reactions with electrodes [44]. With a concentration of TCNQ between 5×10^{-5} and 5×10^{-4} by weight in 8CB, the sample has a bulk electrical conductivity in the range 10^{-8} to 10^{-7} $\Omega^{-1}\text{m}^{-1}$. The conductivity of each film was determined from its ohmic response before the onset of convection, as discussed in detail in Section 2.5.

2.2   The cell

The annular liquid crystal film was about 2 cm in diameter and freely suspended between two concentric disk-like electrodes. The electrodes were made of stainless steel and carefully polished to have very sharp edges, so as to reduce the excess wetting layer of 8CB. Fig. 2.4 illustrates the concentric and annular geometry of the electrode assembly. The annular geometry offers precise current measurement by having no electric leakage through a lateral boundary. The radii of inner and outer electrodes, r_i and r_o, respectively, confine the annular film of width $d = r_o - r_i$. The radius ratio is an important parameter and can be easily tuned by changing the radii of the electrodes. Several inner and outer electrodes of different radii were used. Most radii ranged between $r_i = 4.72 \pm 0.01$ mm and $r_i = 8.88 \pm 0.01$ mm and $r_o = 5.49 \pm 0.01$ mm and $r_o = 11.20 \pm 0.01$ mm. In additional to these ranges, the smallest radius of the inner electrode employed was 0.32 mm. Experiments were conducted at 6 different radius ratios; most of them spread between $\alpha = 0.30$ and $\alpha = 0.80$. The smallest value was $\alpha = 0.05$.
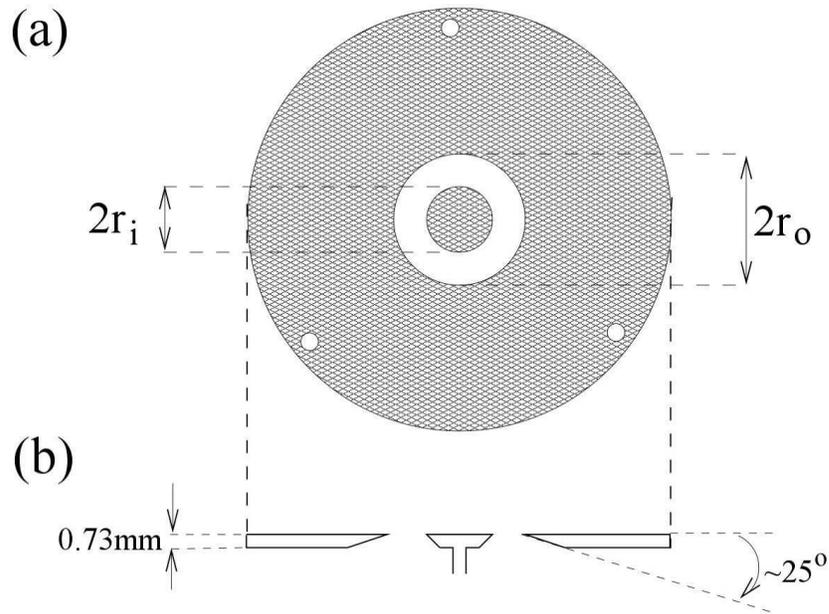
Figure 2.4: The geometry of the electrodes, which support the annular liquid crystal film suspended between the inner and outer diameters, $2r_i$ and $2r_o$, respectively. The electrodes were made of stainless steel. (a) the top view of concentric electrodes; (b) the side view showing the polished sharp edges to hold the thin film. The outer electrode was an annular disk of the outer diameter 9.00 cm with a central hole of diameter $2r_o$ mm. The outer electrode was 0.73 ± 0.01 mm thick.

The film was at atmospheric pressure, and at temperature controlled to yield the Smectic-A phase, with a layered arrangement that restricts fluid motion perpendicular to the layers. In 8CB, each layer is 3.16 nm thick [46]. In all experiments, the used films were uniformly thick between 30 and 85 layers within ± 3 layers. The film thickness is on the order of 0.1 μm and is comparable to the wavelength of visible light. Consequently, the thickness of a film, s, was determined by its interference color under reflected white light, using standard colourimetric functions [47, 48]. The details of the measurement of film thickness are described in Appendix. A. During the course of experiments, the reflected film colour was observed and recorded to obtain the film thickness s.

2.3 Apparatus and setup

This section describes the main features of experimental apparatus, design, and the current-voltage measurements. The apparatus is similar to one used previously for studies of thin-film electroconvection in the weakly nonlinear regime when the imposed voltage is small within ~ 50 volts [37], and has recently been adapted to the turbulent regime [49].

Fig. 2.5 shows the detailed setup schematically. The whole experiment was enclosed by an aluminum box which served as a faraday cage to reduce external electric interference. Experiments were conducted with the film at atmospheric pressure. Previous experiments were carried out both at atmospheric pressure and a reduced ambient pressure of $0.1 - 1.0$ torr. These experiments showed that films at atmospheric pressure suffered less drift in electrical conductivity [37]. Hence, the air was not evacuated in the chamber to stabilize films, especially under large applied voltage. Inside the chamber, the smectic-A film was drawn with a sharp razor blade that was controlled by a motor and suspended between the annulus of stainless electrodes. These electrodes were adjusted to be concentric and were horizontally leveled by a translation stage and tilt adjustment rods, respectively. A effectively white light source using a Tungsten-halogen lamp shone onto the film through a beam splitter and a glass window. The light source was operated at a colour temperature of $\sim 3000\text{K}$ and was assumed to be a black-body radiator. The reflected interference colour of the film was magnified and focused by a low power microscope, recorded by a CCD camera, displayed on a colour monitor, and captured by a frame grabber.

The electronic setup was designed for precise measurement of the current-voltage properties of the freely suspended film. A Kiethley electrometer, computer interfaced through a IEEE GPIB card, served as a voltage source and a picoammeter. The high electric potential provided by the Kiethley electrometer was applied to the inner
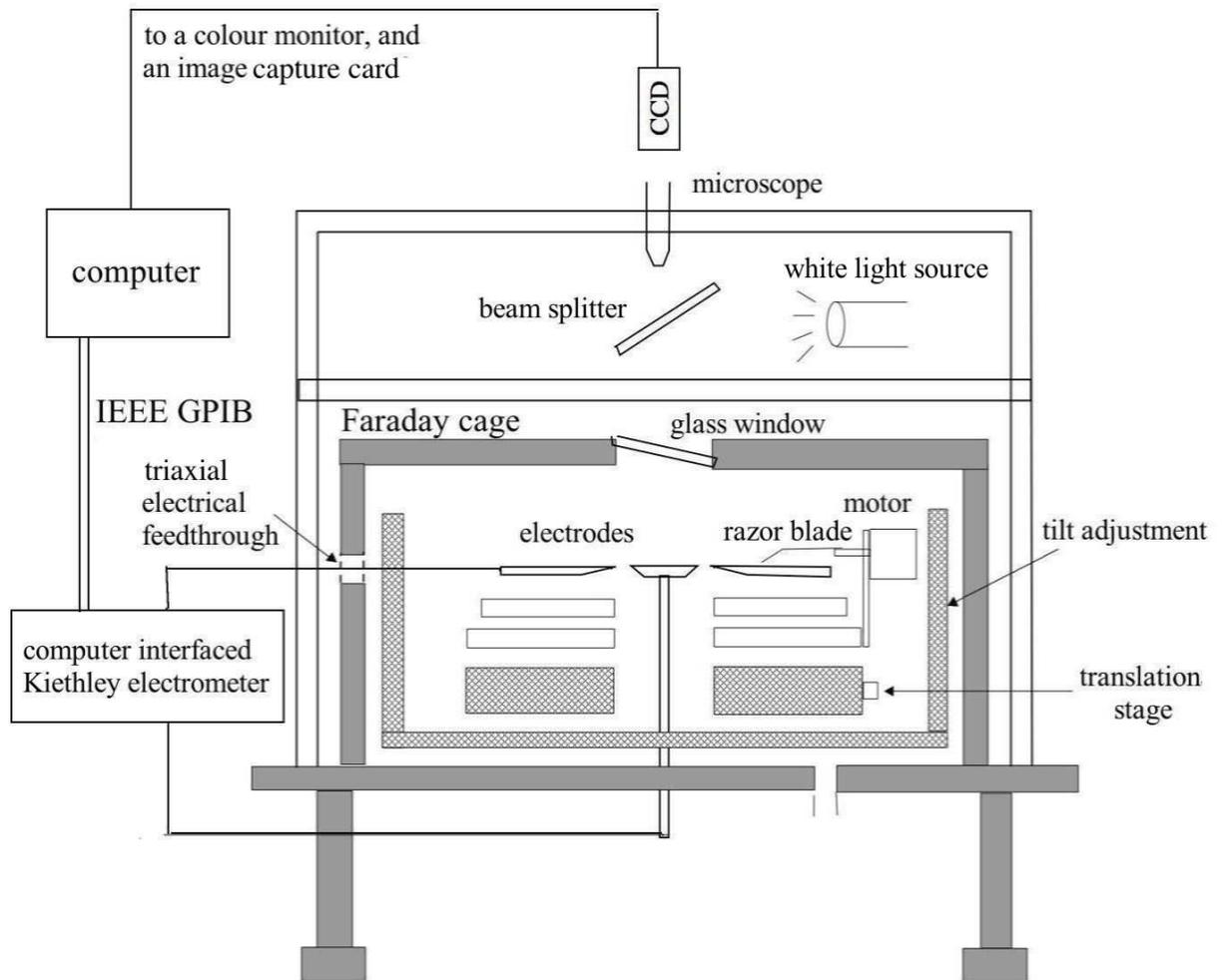
Figure 2.5: Schematic of experimental apparatus.

electrode, whereas a grounded potential was applied to the outer electrodes. However, this ground potential was electrically disconnected from the true earth ground by teflon washers. The measurement connection was made with low noise triaxial cables to reduce electric current leakage. A computer program written in C was first used to interface the electrometer and systematically take data, but later a Labview graphical program was used due to an upgrade of the computer equipment. The typical protocol of the code was to set a voltage and wait for about 10 seconds, then take one hundred measurements of electric current, usually with a sampling rate of 40 Hz. The mean current is the average value of the hundred data points for a given applied voltage. The error in the mean current can be represented by the standard deviation among the hundred measurements.

2.4 Experimental protocol

This section reviews the experimental procedure, including the preparation of liquid crystal samples, the process of making a freely-standing film of uniform thickness, and the key settings and methods to conduct IV measurement.

The procedure for preparing an experimental sample is as follows. First, TCNQ was dissolved in Acetonitrile (ACN), a commonly used solvent, and then added it to the 8CB. Second, ACN was evaporated in a vacuum oven while warming the mixture to mix isotropic 8CB well with TCNQ. The dopant concentrations used in the experiments were 1.91×10^{-4}, 2.96×10^{-4}, 5.8×10^{-4}, and 6.27×10^{-4} by weight in 8CB. From our experience, a much higher or much lower dopant concentration produces non-ohmic response to the applied voltage in the conduction regime. Freshly doped samples with TCNQ have, by themselves, changed colour from the original opaque white to orange, and later to green. The same change in colour was observed in the ACN solution in which TCNQ was dissolved. The duration of time for the

colour change is between weeks to months, however, after a few months the colour of the samples eventually becomes opaque white again. The aged samples used in the experiment were always an off white colour.

A stable freely-standing Smectic-A film of a uniform thickness is essential for accurate IV measurements. The film thickness affects the fluid parameters, such as the Rayleigh and Prandtl numbers, hence all quantitative measurements were performed with uniformly thick films. The protocol to make such a robust film is as follows. First, the electrodes with rather sharp inclines at the edges are crucial to minimize the wetted area of the 8CB film and hence to hold a thin film. Second, all experimental components were cleared in the Faraday chamber in a sequence with acetone, ethanol and deionized water, following by a dried process to remove dust and impurities. Afterward, an extremely tiny amount of the prepared 8CB sample was wetted around both edges of the inner and outer electrodes. The inner and outer electrodes were adjusted to be at the same horizontal level. The film-drawing tool is a very sharp, stainless steel razor blade that is controlled by a stepping motor. By controlling the stepping motor to move the razor blade slowly across the electrodes, an annular smectic-A phase film can be drawn and suspended across the annulus. Films of suitable thickness were obtained by controlling the speed and direction of the stepping motor with different applied voltages. Moving the razor blade back and forth slowly is useful for making a uniform film. After pulling, the razor blade was usually removed or moved far away from the smectic standing film. This ensured that electric perturbation due to the metal blade was negligible when performing an IV measurement.

The main experimental procedure consists of applying a DC voltage V across the film and measuring the resulting electrical current I. The inner electrode is electrically high, and the outer one is grounded. The applied voltage is incremented in small steps from 0 to 1000 V, and then decremented in small steps to zero. At each voltage, the

current is measured with a computer-interfaced electrometer, which is equipped with low noise triaxial cables. The film resistance is on the order of $O(10^{12}\,\Omega)$ and typical currents are ~ 1 pA. An accurate value for the critical voltage V_c at the onset of convection is essential to determine Nu. Hence, a small voltage step, ~ 1 volt, is used to measure V_c in the voltage range between 0 and 50 V, which brackets the typical critical voltage for most of our films. A larger voltage step of ~ 10 V is used in the range 60 to 1000 V. The larger step is necessary to limit the drift in electrical conductivity due to electrochemical reactions in the film. At each applied voltage, 100 current measurements spaced by 25 ms were performed. The averaged values of the current I were used to calculate Nu, as described in detail below. In addition to the IV data, the film thickness s and radius ratio α are measured.

2.5 Data analysis

This section describes the data analysis, focusing on the interpretation of raw experimental IV measurements in terms of the characteristic dimensionless parameters.

A qualitative flow visualization is shown in Fig. 2.6 with a film of uneven thickness at different voltages. When the applied voltage V exceeds the critical voltage V_c, the fluid is organized into convection vortices as shown in Fig. 2.6a. The flow advects electric charge between the electrodes constituting a convection electric current. At higher driving voltage, the flow becomes unsteady while retaining large scale structures of convecting vortices (see Fig. 2.6b). These patterns are reflected by the variation of film thickness, which unfortunately is not ideal for passive flow-tracking. Since the film thickness affects the fluid parameters, all quantitative data were acquired with uniformly thick films in which no flow is visible.

Fig. 2.7 shows a representative IV response of a uniformly thick film. The critical voltage V_c is identified by the upward kink in the IV curve at $V \sim 40$V, after which
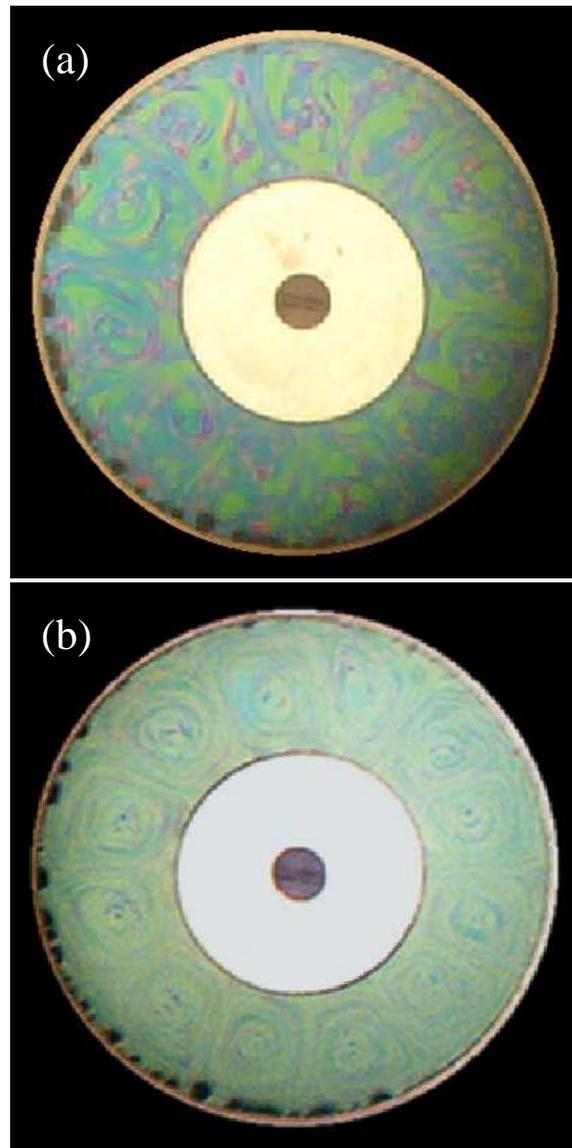
Figure 2.6: Qualitative visualization of electroconvective flows, characterized by a film of uneven thickness: At (a) $V = 100$ volts and (b) $V = 250$ volts. Data, however, were acquired only from uniformly thick films and thus flow visualization is not available.
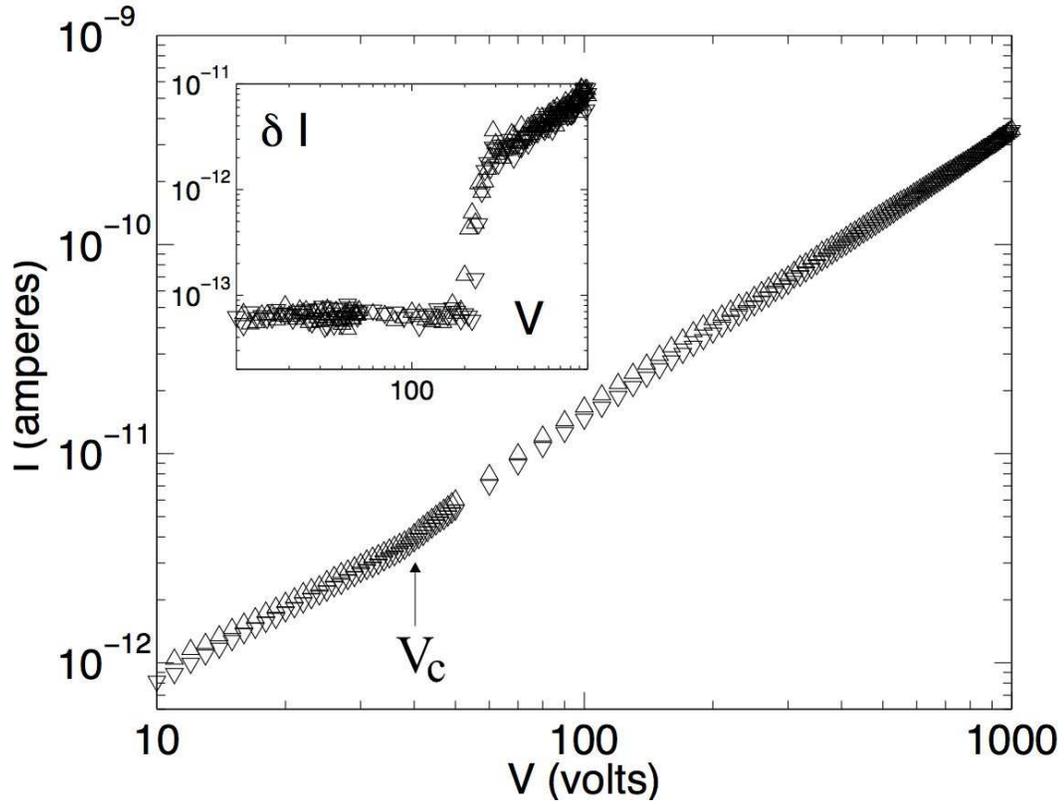
Figure 2.7: A representative current-voltage curve for an annular film, showing the onset of electroconvection. Data obtained for increasing (decreasing) voltages are shown in $\triangle(\triangledown)$. The inset shows the rms fluctuations of the current, δI vs. the applied voltage, V. Here $\alpha = 0.37 \pm 0.01$ and $\mathcal{P} = 23 \pm 2$.

the film makes a transition from conduction to convection. When $V < V_c$, the fluid is motionless and charge is carried by ohmic conduction. When $V > V_c$, the electrical driving force overcomes dissipation and the film flows in a series of counter-rotating vortices, which are laminar for small $V > V_c$. The fluid circulation carries an additional current by convection, as is apparent by the increase in the slope of the IV curve above V_c. At higher voltages, the vortices become unsteady. The transition to unsteady flow is identified by a sudden jump in the current fluctuations at $V \sim 200$V, as shown in the inset of Fig. 2.7. With even higher driving voltage $V \gtrsim 600$V, the flow becomes turbulent. It is in this highest range of V that $Nu - \mathcal{R}$ power law scalings were observed in the experiments.

The Rayleigh number $\mathcal{R}$ (the main control parameter) and the Prandtl number $\mathcal{P}$ (the fluid parameter) can be directly obtained from the IV measurements. They are previously described in Eqn.1.3, in terms of experimentally measurable parameters. The derivations of $\mathcal{R}$ and $\mathcal{P}$ are described in Section 3.2. This section focuses on determining them from the experimental data. The 3D bulk electrical conductivity σ was obtained by measuring the ohmic conductance C of the film, via the following equation:

$$C = \frac{2\pi s \sigma}{\ln\left(1/\alpha\right)} = \frac{I}{V} \quad \text{for} \quad V < V_{c}, . \tag{2.1}$$

C can be directly determined from the slope of the IV curve in the conductive regime for voltages below the critical voltage V_c. Here, α is the radius ratio and s is the film thickness. The 3D shear viscosity has been measured to be $\eta = 0.19 \pm 0.05 \ kg/ms$ at atmospheric pressure by previous experiments [37]. The 8CB fluid density ρ at room temperature is $1.0 \times 10^3 \ kg/m^3$ [50]. As previously mentioned, the film thickness s is determined by matching the observed reflection color of the film to a color chart; this method is described in Appendix A. After finding the film conductance C, the dimensionless Nusselt number Nu can be directly calculated from IV data, following Eqn. 1.5:

$$Nu = \frac{I}{I_c} = \frac{I}{CV}. \tag{2.2}$$

In summary, the raw IV data can be interpreted in terms of the key dimensionless parameters Nu, $\mathcal{R}$ and $\mathcal{P}$, which play similar roles to those in Rayleigh-Bénard convection. The main error in determining Nu, $\mathcal{R}$ and $\mathcal{P}$ is attributed to the drift of the film conductance C, as will be discussed later in this section.

In the experiments $\mathcal{R}$ varied between 0 and $\sim 10^5$. This is moderate compared with the very high Rayleigh numbers achievable in Rayleigh-Bénard convection. However, the critical value $\mathcal{R}_c$ of $\mathcal{R}$ at the onset of electroconvection is about a factor of 10 smaller than that for Rayleigh-Bénard convection [11, 37, 49]. A higher $\mathcal{R}$ could

be attained by simply increasing the applied voltage V. However, large electric fields will eventually lead to dielectric breakdown, destroying the film. Estimated with the present material parameters, the maximum accessible $\mathcal{R}$ is about 10^6. The Prandtl number $\mathcal{P}$ was in the range of $5 < \mathcal{P} < 250$.

Fig. 2.8 is a representative plot of Nu vs $\mathcal{R}$. For $Nu = 1$, the film's dissipation smoothes out the small electrical body force so that the fluid is still. The onset of convection, the critical Rayleigh number $\mathcal{R}_c$, locates at the transition from $Nu = 1$ to $Nu > 1$, with the additional current carried by the convection process. Previous studies only focused on the influences of $\alpha, \mathcal{P}$, and Re on the onset of convection [51, 52, 38]. Right above $\mathcal{R}_c$, organized vortex patterns of a critical number of pairs emerge, strongly depending on α [38]. When $\mathcal{R} \gtrsim 10^4$, a scaling law between charge transport and the control parameter $\mathcal{R}$ was observed for the first time in smectic electroconvection. A least squares fit, $Nu = A\,\mathcal{R}^\gamma$, was performed to the $Nu-\mathcal{R}$ data in the region where $\mathcal{R} \gtrsim 100\,\mathcal{R}_c$, where $\mathcal{R}_c$ is the critical Rayleigh number at the onset of convection. For the data depicted in Fig. 2.8, the $Nu - \mathcal{R}$ scaling exponent γ was found to be 0.23 ± 0.01. In this thesis, the charge transport scaling is of main interest in the turbulent regime, particularly how the Nu power-law depends on $\mathcal{P}$ and α. The data under various parameters are listed in Table 5.2 and discussed in detail in Section 5.3.

The error in the scaling exponent γ in the relation $Nu \sim \mathcal{R}^\gamma$ stems from uncertainties in the film thickness s, the critical voltage V_c, and the film conductance C. The main source of error is the drift in the film conductance C. The drift results in slightly different slopes for the IV curves in the conductive regime between the increasing voltage and decreasing voltage sweeps in a single experiment. The cause of the conductance drift is not well understood, but is presumably due to electrochemical changes in the liquid crystal material. The total DC charge flow is quite large; approximately $0.4\mu C$ over a time interval of about one hour. A large drift in the
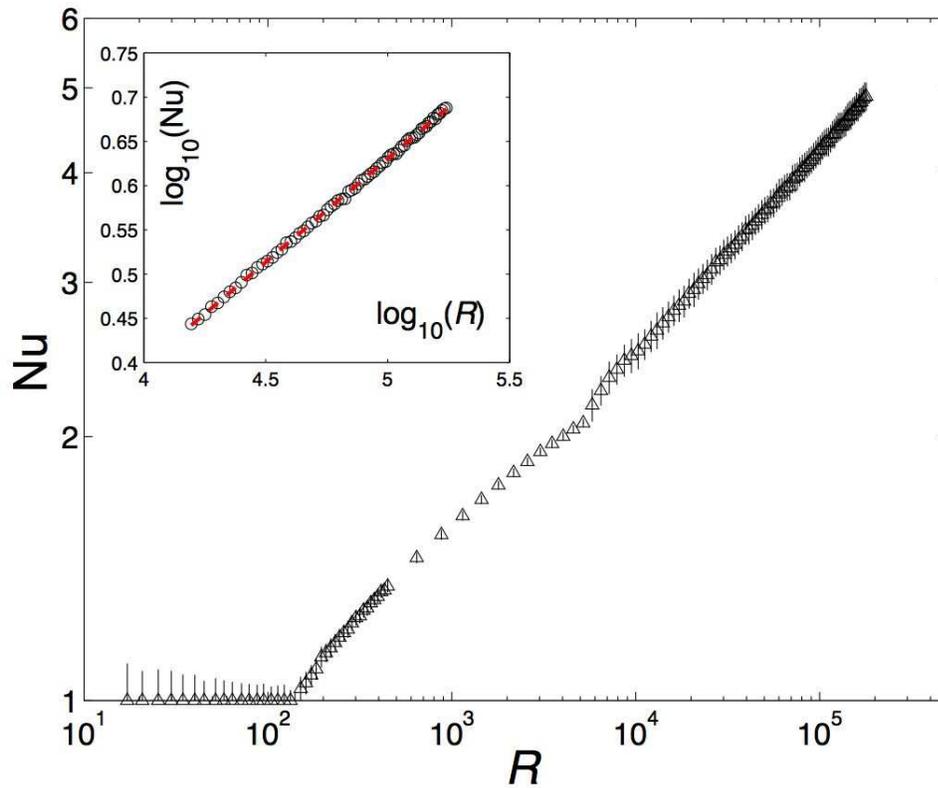
Figure 2.8: Variation of Nusselt number with Rayleigh number for annular electro-convection for $\mathcal{P} = 35$ and $\alpha = 0.51 \pm 0.01$, showing the existence of a power-law in the high Rayleigh region. The dashed line on the inset is the least square fit for the scaling, for $\mathcal{R} \gtrsim 1.5 \times 10^4$. Here, $\gamma = 0.23 \pm 0.01$, for the fitting function $Nu = A \, \mathcal{R}^{\gamma}$.

film conductance can lead to a significant uncertainty in the $Nu - \mathcal{R}$ scaling and an uncontrolled variation of both $\mathcal{R}$ and $\mathcal{P}$. In principle, this drift could be completely compensated for if C were known for every IV measurement. Unfortunately, the conductance C cannot be independently determined from the data while the film is convecting. Thus C was calculated with the IV data in the conduction regime, which occurs before and after the convection regime during one voltage sweep.

In order to bracket the drift, the data were analyzed using two methods, which are referred to as the piecewise Method A and the linear Method B for conduction correction. From a fit to the ohmic response at the beginning and end of each sweep, two conductances, C_{up} and C_{down} were determined. In piecewise Method A, C_{up} was used to reduce the data obtained when incrementing the voltage and C_{down} was employed to reduce the data obtained when decrementing the voltage. This method concentrates the conductance error at the maximum voltage, and thus overestimates the effect of drift at the highest voltages. In the second method, which we refer to below as linear Method B, we instead assume that the conductance C varies linearly between C_{up} and C_{down} while the fluid is convecting. This method can be thought of as a linear approximation to the unknown evolution of C while the film is convecting. It probably underestimates the true drift. By comparing the results using methods A and B, the overall effect of the drift can be gauged. In some runs, particularly large drifts made compensating for the drift essentially impossible. Hence, the runs in which the difference in C_{up} and C_{down} exceeded 30% were discarded. All the data were analyzed using both methods and the results will be discussed in Section 5.3.

Experiments in high Rayleigh number with no imposed shear have been undertaken. As the applied voltage was increased, a large current fluctuation was observed beyond the steady laminar convective state, the main focus of previous studies. However, experiments with no flow visualization reach the limit of explaining the causes of current fluctuation, which can be linked to the complex flow dynamics. Consequently,

during the course of this research, a direct numerical simulation for the first time has been carried out to investigate more complicated, nonlinear states of annular electroconvection. Next chapter describes the method and validation of this simulation code.

Chapter 3

Direct numerical simulation

3.1 Introduction

This chapter presents the first direct numerical study of annular smectic electrocon-
vection in a thin film. This simulation code was developed from scratch to complement
the experimental investigations for the reasons described below. Smectic electrocon-
vection has previously attracted detailed experimental [1, 49, 52, 53, 54, 55, 56] and
theoretical [36, 38, 51] treatments, however these studies have focused on the flow
regime close to the onset of convection and used limited flow visualization. When the
electric driving force is not strong, electroconvection is steady in the weakly nonlinear
regime. Previous experimental work in this regime has shown that the amplitude of
convection just above onset is well modeled by a Landau amplitude equation with a
cubic nonlinearity [54]. In addition, previous theoretical analyses, using amplitude
equations derived from first principles, showed good agreement between experiment
and theory in this slightly perturbed state [55]. Nevertheless, both linear stability
theory and experimental data with no flow visualization reach their limit when the
complexity gradually accumulates as the driving forces are increased. Direct numeri-
cal simulation not only allows a broader range of parameter values, but also provides

the flow field which benefits the understanding of complex dynamics as $\mathcal{R}$ is increased.

Direct numerical simulations offer complementary insights into this system with the dynamics of all the basic fields: velocity field, charge distribution, and electric potential. After the simulation codes was validated, the early numerical investigations focused on the primary bifurcation over a wide parameter range in the weakly nonlinear regime, i.e., under small electric driving forces. The numerical data with no applied shear showed supercritical bifurcation near the onset of convection and agreed well with theoretical predictions and most early experimental data [38]. These results are discussed in detail in Section 5.1. Then, the numerical studies of sheared convection were performed. Hopf and subcritical bifurcations were observed after the primary bifurcation. These bifurcations in sheared convection reveal new and interesting flow dynamics which was not available in previous experiments (as will be fully discussed in Section 5.2). Furthermore, the simulation code has been extended to the highly nonlinear, turbulent regime where Nu scaling behavior was observed experimentally [49, 56], as described in the preceding chapter.

The chapter is organized as follows: first, the mathematical model and underlying physics are introduced. Then, a pseudo-spectral numerical method, the detailed numerical methods, and the employed parameters are described. Finally, the numerical data are shown as the control parameter $\mathcal{R}$ is increased, in particular the data for the critical Rayleigh number $\mathcal{R}_c$ and the critical mode number m_c—the most unstable azimuthal mode at $\mathcal{R}_c$—which are benchmarked against previous theoretical predictions to validate the simulation code.

3.2 Mathematical model

In the experiment, the physical thickness of the film, $s \approx 0.1\mu$m, is much smaller than the width of the annulus $d \approx 1$ mm. This, and the layered structure of the smectic,

allows us to accurately model the film as a two-dimensional (2D), Newtonian fluid confined to an annular space between infinitely thin electrodes which lie in the xy plane. The rest of the three-dimensional computational space is empty and free of charges. The film is essentially surface dominated, as the ratio of bulk to surface forces on the film are $O(s/d) \approx 10^{-4}$ [51]. The constant thickness also means that the fluid is effectively incompressible.

The annular film is a two dimensional sheet that spans the region $r_i \leq r \leq r_o$ at $z = 0$ in a cylindrical coordinate system (see Fig. 1.1). On the plane $z = 0$, the inner electrode occupies the region $0 \leq r \leq r_i$ and the outer one spans the region of $r_o \leq r \leq \infty$. The film is a Newtonian, incompressible, electrically conducting fluid with 2D density $\tilde{\rho}$, molecular viscosity $\tilde{\eta}$, and electric conductivity $\tilde{\sigma}$. These 2D quantities are related to their 3D counterparts by the film thickness s:

$$\tilde{\rho} = \rho s, \qquad \tilde{\eta} = \eta s, \qquad \tilde{\sigma} = \sigma s, \tag{3.1}$$

where ρ is the bulk mass density, η is the 3D shear viscosity, and σ is the bulk electrical conductivity.

We write the equations governing the fluid and charge in the annular film using 2D differential operators, field variables and material parameters. The governing equations are comprised of the mass, momentum and charge conservation equations, with one additional Maxwell equation relating the charge density q to the electric potential ψ. Magnetic and polarization effects are negligible [35].

The governing equations are, in full:

$$\nabla \cdot \vec{\mathbf{u}} = 0, \tag{3.2}$$

$$\tilde{\rho} \left[\frac{\partial \vec{\mathbf{u}}}{\partial t} + (\vec{\mathbf{u}} \cdot \nabla)\vec{\mathbf{u}} \right] = -\nabla P + \tilde{\eta}\nabla^2 \vec{\mathbf{u}} + q\vec{\mathbf{E}}, \tag{3.3}$$

$$\frac{\partial q}{\partial t} = -\nabla \cdot (\tilde{\sigma}\vec{\mathbf{E}} + q\vec{\mathbf{u}}), \tag{3.4}$$

$$q = -2\epsilon_0 \partial_z \psi|_{z=0^+}, \tag{3.5}$$

$$(\nabla^2 + \partial_{zz})\psi = 0, \tag{3.6}$$

$$\psi_2 = \psi(z = 0), \tag{3.7}$$

where $\vec{\mathbf{u}}$ is the fluid velocity, P is the areal pressure, q is the surface charge density, and $\vec{\mathbf{E}} = -\nabla\psi|_{z=0}$ is the electric field in the film plane. ϵ_0 is the permittivity of free space.

The equation of mass conservation and the incompressibility condition yield a solenoidal velocity field $\vec{\mathbf{u}}$, by Eqn. 3.2. The flow velocity is determined from the conservation of momentum using Eqn. 3.3, which is the 2D Navier-Stokes equations with an electrical body force $q\vec{\mathbf{E}}$. The conservation of charge is expressed by a continuity equation, Eqn. 3.4, containing an ohmic conductive current density $\tilde{\sigma}\vec{\mathbf{E}}$ and a convective current density $q\vec{\mathbf{u}}$. Finally, the 2D charge density q obeys Eqn. 3.5, a Maxwell equation that describes the nonlocal relationship between the surface charge q and the electric potential ψ. The factor of 2 in Eqn. 3.5 arises because the film has two free surfaces. Outside the film, there are no free charges, so the 3D electric potential ψ obeys the Laplace equation, Eqn. 3.6. Eqn. 3.7 expresses the fact that the electric potential is everywhere continuous; its value ψ_2 on the film acts as a boundary condition on the potential ψ which fills the space outside the film.

The fluid velocity is subject to a no-slip boundary condition $u_r = u_\theta = 0$ at the inner and outer radii of the annulus, $r = r_i$ and $r = r_o$, respectively. The potential

ψ_2 is required to be V, the applied voltage on the inner electrode, $r \leq r_i$, and zero on the outer electrode $r \geq r_o$. $\psi = 0$ at infinity. The potential on the film itself can be found by specifying q for $r_i < r < r_o$ and solving the mixed boundary value Laplace problem given by Eqns. 3.5 and 3.6 for ψ. Alternatively, ψ_2 can be specified on the film, and ψ found self-consistently by solving the Dirichlet Laplace problem given by Eqn. 3.6. The charge density q then follows from Eqn. 3.5.

The streamfunction-vorticity formulation was employed for the primitive variables in the simulation. The streamfunction ϕ is given by $\vec{u} = \nabla\phi \times \hat{z}$. In two dimensions, the vorticity ω is a scalar obeying $\nabla \times \vec{u} = \omega\hat{z}$. In terms of the streamfunction ϕ, the velocity field follows the following equations:

$$\vec{u} = u_r\hat{r} + u_\theta\hat{\theta} = \frac{1}{r}\frac{\partial\phi}{\partial\theta}\hat{r} - \frac{\partial\phi}{\partial r}\hat{\theta}. \tag{3.8}$$

The advantages of using the streamfunction-vorticity formulation are the elimination of the pressure P and the replacement of the vector velocity by two simpler scalar fields, ϕ and ω.

Starting from the streamfunction-vorticity formulation, we rescaled length with the film width d, time with the charge relaxation time $\tau_c = \epsilon_0 d/\tilde{\sigma}$, and electric potential by the applied voltage V at r_i. The dimensionless streamfunction ϕ and charge density q are then scaled by $\tilde{\sigma}d/\epsilon_0$ and $\epsilon_0 V/d$, respectively. Then, the dimensionless governing equations correspond to:

$$\nabla^2\phi = -\omega, \tag{3.9}$$

$$\frac{\partial\omega}{\partial t} + (\vec{u}\cdot\nabla)\omega = \mathcal{P}\nabla^2\omega + \mathcal{P}\,\mathcal{R}\,(\nabla\psi_2 \times \nabla q), \tag{3.10}$$

$$\frac{\partial q}{\partial t} + (\vec{u}\cdot\nabla)q = \nabla^2\psi_2, \tag{3.11}$$

$$(\nabla^2 + \partial_{zz})\psi = 0, \qquad q = -2\partial_z\psi|_{z=0^+}, \tag{3.12}$$

where the important dimensionless parameters are

$$\mathcal{R} \equiv \frac{\epsilon_0^2 V^2}{\tilde{\sigma}\tilde{\eta}} = \frac{\epsilon_0^2 V^2}{\sigma\eta s^2}, \quad \text{and} \tag{3.13}$$

$$\mathcal{P} \equiv \frac{\epsilon_0\tilde{\eta}}{\tilde{\rho}\tilde{\sigma}d} = \frac{\epsilon_0\eta}{\rho\sigma s d}. \tag{3.14}$$

The main control parameter, the Rayleigh number $\mathcal{R}$, is a measure of the relative strength of applied electric forcing to viscous dissipation. The Prandtl number $\mathcal{P}$ is a fluid parameter which characterizes the ratio of charge relaxation time to the viscous relaxation time. Note that $\mathcal{R}$ and $\mathcal{P}$ in 2D electroconvection depend on the film thickness s and the film width d, in contrast to the Rayleigh-Bénard case in which Pr is independent of the dimensions of the cell.

The geometry of the annulus is characterized by the the radius ratio $\alpha \equiv r_i/r_o$. In dimensionless terms, the inner and outer radii are

$$r_i' = \frac{r_i}{d} = \frac{\alpha}{1-\alpha} \quad \text{and} \quad r_o' = \frac{r_o}{d} = \frac{1}{1-\alpha}. \tag{3.15}$$

The computational domain is mainly the annulus $r_i' \leq r \leq r_o'$ and $0 \leq \theta < 2\pi$. The solutions are decomposed into an axisymmetric base state component (denoted by superscript zero) and a perturbation or a deviation from the base state (denoted by superscript one) as follows:

$$\phi(r,\theta) = \phi^{(0)}(r) + \phi^{(1)}(r,\theta), \tag{3.16}$$

$$\omega(r,\theta) = \omega^{(0)}(r) + \omega^{(1)}(r,\theta), \tag{3.17}$$

$$q(r,\theta) = q^{(0)}(r) + q^{(1)}(r,\theta), \tag{3.18}$$

$$\psi_2(r,\theta) = \psi_2^{(0)}(r) + \psi_2^{(1)}(r,\theta), \tag{3.19}$$

$$\psi(r,\theta,z) = \psi^{(0)}(r,z) + \psi^{(1)}(r,\theta,z). \tag{3.20}$$

The charge and potential distributions in the base state, in which the fluid is quiescent, can be analytically solved. When the fluid velocity field is zero everywhere under no external shear, the base state solutions are as follows [38]:

$$\phi^{(0)}(r) = 0, \tag{3.21}$$

$$\omega^{(0)}(r) = 0, \tag{3.22}$$

$$\psi_2^{(0)}(r) = \begin{cases} 1 & \text{for} \quad 0 \leq r \leq r_i \\ \frac{1}{\ln(\alpha)}[\ln(1-\alpha) + \ln(r)] & \text{for} \quad r_i \leq r \leq r_o \\ 0 & \text{for} \quad r \geq r_o \end{cases} \tag{3.23}$$

$$\psi^{(0)}(r, z) = \int_0^\infty dk\ e^{-kz} J_0(kr) A(k), \tag{3.24}$$

$$q^{(0)}(r) = 2\int_0^\infty dk\ k^2 J_0(kr) \left[\int_0^\infty d\zeta \zeta \psi^{(0)}(\zeta, 0) J_0(k\zeta)\right] \tag{3.25}$$

$$= \frac{2}{\ln\alpha} \left[\frac{1}{r} F\left(\frac{1}{2}, \frac{1}{2}; 1; \frac{r_o^2}{r^2}\right) - \frac{1}{r_i} F\left(\frac{1}{2}, \frac{1}{2}; 1; \frac{r^2}{r_i^2}\right)\right], \tag{3.26}$$

where F is the hypergeometric function $_2F_1$ [38], J_0 is the zeroth order Bessel function, and

$$A(k) = k \int_0^\infty dr\ r\psi^{(0)}(r, 0) J_0(kr). \tag{3.27}$$

The base state surface charge $q^{(0)}$ reveals an unstable inverted charge configuration in which positive charges accumulate close to inner electrode of high electric potential while negative charges do so close to the outer electrode of voltage ground. This unstable surface charge distribution gives rise to the convective mechanism, similar to inverted density profile in thermal convection. Note that in the case of an applied shear, the base state of the streamfunction, instead of Eqn.3.21, changes to

$$\partial_r\phi^{(0)}(r) = \frac{\alpha^2\Omega}{1-\alpha^2}\left(r - \frac{1}{r(1-\alpha)^2}\right), \tag{3.28}$$

where α is the radius ratio, and Ω is the dimensionless angular rotation frequency

of the inner electrode. Here, $\Omega = \tau_c \boldsymbol{\omega}$, where $\boldsymbol{\omega}$ is the applied angular rotation frequency, and τ_c is the charge relaxation time defined previously. The strength of the imposed shear is described by the dimensionless Reynolds number Re, with the velocity characterized by the angular velocity of the rotating inner electrode and the length by the film width d; it follows:

$$Re = \frac{r_i' \Omega}{\mathcal{P}}, \qquad (3.29)$$

with r_i' in the dimensionless form of r_i using Eqn. 3.15, and $\mathcal{P}$ the Prandtl number. The centrifugal and Coriolis forces due to the imposed shear in 2D can be dealt with by introducing a new form of the fluid pressure term in Eqn. 3.3. The base state of electric potential and surface charge do not alter even under an influence of a shear.

Although the base state potential $\psi_2^{(0)}$ is everywhere single valued and continuous, its derivatives with respect to r are discontinuous at the edges of the film, where the potential on the film changes over to the constant imposed potential on the electrodes. This causes the base state charge density $q^{(0)}$, given analytically in terms of hypergeometric functions [38], to be divergent at the edges of the film.

With the above decompositions, the unknowns to be computed are the deviation parts (denoted as superscripts (1)), which are solutions of the the following set of equations:

$$\nabla^2 \phi^{(1)} = -\omega^{(1)}, \qquad (3.30)$$

$$\frac{\partial q^{(1)}}{\partial t} + \mathcal{J}_{q,\phi} - \nabla^2 \psi_2^{(1)} = 0, \qquad (3.31)$$

$$\frac{\partial \omega^{(1)}}{\partial t} + \mathcal{J}_{\omega,\phi} = \mathcal{P} \, \nabla^2 \omega^{(1)} + \mathcal{P}\mathcal{R} \, \mathcal{J}_{\psi,q}, \qquad (3.32)$$

$$(\nabla^2 + \partial_{zz})\psi^{(1)} = 0, \quad q^{(1)} = -2\partial_z \psi^{(1)}|_{z=0}, \qquad (3.33)$$

where $\mathcal{J}_{q,\phi}$, $\mathcal{J}_{\omega,\phi}$, and $\mathcal{J}_{\psi,q}$ are the nonlinear Jacobian terms:

$$\mathcal{J}_{q,\phi} = \frac{1}{r}\left[\frac{\partial q^{(0)}}{\partial r}\frac{\partial \phi^{(1)}}{\partial \theta} + \frac{\partial q^{(1)}}{\partial r}\frac{\partial \phi^{(1)}}{\partial \theta} - \frac{\partial \phi^{(0)}}{\partial r}\frac{\partial q^{(1)}}{\partial \theta} - \frac{\partial \phi^{(1)}}{\partial r}\frac{\partial q^{(1)}}{\partial \theta}\right], \quad (3.34)$$

$$\mathcal{J}_{\omega,\phi} = \frac{1}{r}\left[\frac{\partial \omega^{(0)}}{\partial r}\frac{\partial \phi^{(1)}}{\partial \theta} + \frac{\partial \omega^{(1)}}{\partial r}\frac{\partial \phi^{(1)}}{\partial \theta} - \frac{\partial \phi^{(0)}}{\partial r}\frac{\partial \omega^{(1)}}{\partial \theta} - \frac{\partial \phi^{(1)}}{\partial r}\frac{\partial \omega^{(1)}}{\partial \theta}\right], \quad (3.35)$$

$$\mathcal{J}_{\psi,q} = \frac{1}{r}\left[\frac{\partial \psi_2^{(0)}}{\partial r}\frac{\partial q^{(1)}}{\partial \theta} - \frac{\partial q^{(0)}}{\partial r}\frac{\partial \psi_2^{(1)}}{\partial \theta} + \frac{\partial \psi_2^{(1)}}{\partial r}\frac{\partial q^{(1)}}{\partial \theta} - \frac{\partial q^{(1)}}{\partial r}\frac{\partial \psi_2^{(1)}}{\partial \theta}\right]. \quad (3.36)$$

The variables $\phi^{(1)}, \psi_2^{(1)}$ and $\psi^{(1)}$ satisfy the following boundary conditions for $r = r_o'$ and r_i':

$$\phi^{(1)}(\theta) = \partial_r \phi^{(1)}(\theta) = \psi_2^{(1)}(\theta) = 0, \quad (3.37)$$

$$\psi^{(1)}(r, \theta, z = 0) = \begin{cases} 0 & 0 \leq r \leq r_i' \\ \psi_2^{(1)}(r, \theta) & r_i' \leq r \leq r_o' \\ 0 & r \geq r_o'. \end{cases} \quad (3.38)$$

The Jacobians $\mathcal{J}_{q,\phi}$ and $\mathcal{J}_{\psi,q}$ each contain terms proportional to $\partial q^{(0)}/\partial r$, which diverges at the edges of the film. In each case these terms multiply quantities that are zero at the edges of the film and the overall expressions remain finite. Similarly, the piecewise continuous nature of the boundary conditions on $\psi^{(1)}$, given by Eqn. 3.38, implies that $\partial q^{(1)}/\partial r$ diverges at the edges of the film, but in Eqns. 3.34 and 3.36, these divergences multiply zero quantities.

We now turn to the numerical solution and the scheme of these perturbed Eqns. 3.30-3.33.

3.3 A pseudo-spectral method

A time-stepping, pseudo-spectral code was constructed to calculate the solutions for the deviations governed by Eqns. 3.30 - 3.33. Two different time discretization

schemes were employed and their results were compared to estimate the accuracy of the solutions. Then, the solutions were used to calculate integrated physical quantities of interest, such as kinetic energy and charge transport, which are directly related to the experimental measurements.

3.3.1 Time discretization schemes

The first time discretization method is the Adams-Bashforth and Backward Differentiation (AB/BDI2) scheme [57]. In this method, the time derivative was modeled by $\partial_t U \approx (3U^{k+1} - 4U^k + U^{k-1})/(2\Delta t)$, where the superscript k denotes the time-stepping index and Δt was a properly chosen discrete time-stepping size. The diffusion term f was approximated by f^{k+1}, using a backward scheme. The nonlinear Jacobian terms and the external forcing terms F were estimated with the first order Adams-Bashforth scheme: $AB_1\{F\} = 2F^k - F^{k-1}$. The combination of these two first-order approximation scheme gives the discretized equations second order accuracy. The corresponding discretization equations are listed below (we denote the unknown deviations without the notations of superscripts one):

$$\nabla^2 \phi^{k+1} = -\omega^{k+1},, \tag{3.39}$$

$$\frac{3q^{k+1} - 4q^k + q^{k-1}}{2\Delta t} + AB_1\{\mathcal{J}_{q,\phi}\} = \nabla^2 \psi_2^{k+1}, \tag{3.40}$$

$$\frac{3\omega^{k+1} - 4\omega^k + \omega^{k-1}}{2\Delta t} + AB_1\{\mathcal{J}_{\phi,\omega}\} = \mathcal{P}\nabla^2\omega^{k+1} + \mathcal{PR} \cdot AB_1\{\mathcal{J}_{\psi,q}\}, \tag{3.41}$$

$$\nabla_3^2 \psi^k = 0, \quad q^k = -2\{\partial_z \psi|_{z=0^+}\}^k, \tag{3.42}$$

where

$$
\{\mathcal{J}_{q,\phi}\}^k = \frac{1}{r}\left[\frac{\partial q^{(0)}}{\partial r}\frac{\partial \phi^{(1)}}{\partial \theta} + \frac{\partial q^{(1)}}{\partial r}\frac{\partial \phi^{(1)}}{\partial \theta} - \frac{\partial \phi^{(0)}}{\partial r}\frac{\partial q^{(1)}}{\partial \theta} - \frac{\partial \phi^{(1)}}{\partial r}\frac{\partial q^{(1)}}{\partial \theta}\right]^k,
$$

$$
\{\mathcal{J}_{\omega,\phi}\}^k = \frac{1}{r}\left[\frac{\partial \omega^{(0)}}{\partial r}\frac{\partial \phi^{(1)}}{\partial \theta} + \frac{\partial \omega^{(1)}}{\partial r}\frac{\partial \phi^{(1)}}{\partial \theta} - \frac{\partial \phi^{(0)}}{\partial r}\frac{\partial \omega^{(1)}}{\partial \theta} - \frac{\partial \phi^{(1)}}{\partial r}\frac{\partial \omega^{(1)}}{\partial \theta}\right]^k,
$$

$$
\{\mathcal{J}_{\psi,q}\}^k = \frac{1}{r}\left[\frac{\partial \psi_2^{(0)}}{\partial r}\frac{\partial q^{(1)}}{\partial \theta} - \frac{\partial q^{(0)}}{\partial r}\frac{\partial \psi_2^{(1)}}{\partial \theta} + \frac{\partial \psi_2^{(1)}}{\partial r}\frac{\partial q^{(1)}}{\partial \theta} - \frac{\partial q^{(1)}}{\partial r}\frac{\partial \psi_2^{(1)}}{\partial \theta}\right]^k.
$$

The second time discretization method is the semi-implicit first order Euler differentiation scheme [58]. In this method, the time derivative is approximated by $\partial_t U \approx (U^{k+1} - U^k)/(\Delta t)$. The nonlinear terms and external forcing terms were estimated by the forward Euler scheme, $i.e.$ using the values F^k at current time step k, while the diffusion term was approximated by f^{k+1}, using a backward Euler scheme.

These two discretization methods yielded consistent simulation results, particularly in the weakly nonlinear regime. However, for the higher Rayleigh number regime, the AB/BDI2 scheme was more preferable for its higher order accuracy.

3.3.2 Numerical solution of the time-discretized equations

The time-discretized equations was solved by a pseudo-spectral method. The streamfunction ϕ, the vorticity ω, the 2D electric potential ψ_2 and the surface charge density q were approximated by a truncated Fourier series in the $\hat{\theta}$ direction and by Chebyshev polynomials in the $\hat{r}$ direction,

$$
\phi^{(1)}(r,\theta,t) = \sum_{m=-K}^{K} \widehat{\phi}_m(r,t)e^{im\theta}, \tag{3.43}
$$

$$
\omega^{(1)}(r,\theta,t) = \sum_{m=-K}^{K} \widehat{w}_m(r,t)e^{im\theta}, \tag{3.44}
$$

$$
\psi_2^{(1)}(r,\theta,t) = \sum_{m=-K}^{K} \widehat{\psi}_{2m}(r,t)e^{im\theta}, \tag{3.45}
$$

$$q^{(1)}(r,\theta,t) \;=\; \sum_{m=-K}^{K} \widehat{q}_m(r,t)e^{im\theta}. \tag{3.46}$$

The variables ϕ, ω, ψ_2, and q are all real so in practice we solve for $m = 0, 1, ..., K$ and use the complex conjugate relationship $\widehat{\phi}_{-m} = \widehat{\phi}_m^*$ for $m < 0$.

The 2D electric potential ψ_2 and the surface charge density q are not freely evolving, independent variables. They evolve simultaneously so that at each time step they are linked by the nonlocal coupling described in Sec. 3.2. The next section describes the numerical calculation for this nonlocal relationship between $\widehat{\psi}_{2m}(r)$ and $\widehat{q}_m(r)$, using Eqns. 3.5 and 3.6. This instantaneous relationship can be computed separately and then applied at each time step, which greatly simplifies the time stepping procedure.

The partial differential equations (PDEs) given by Eqns. 3.30 - 3.33 were converted into ordinary differential equations (ODEs) in r by substituting Eqns. 3.43—3.46 and using the orthogonality of the Fourier modes. The Chebyshev collocation method [59, 60] was employed to solve the ODEs with the Fourier coefficients as unknowns. There were $N_c + 1$ grid points in the radial direction, where N_c is the order of highest Chebyshev polynomial included. The radial range from r_i' to r_o' is linearly mapped onto a new variable x using

$$x = 2r - \left[\frac{1+\alpha}{1-\alpha} \right], \tag{3.47}$$

such that $-1 \leq x \leq 1$ spans the film. The collocation method approximates the solution as a truncated Chebyshev polynomial series and makes the residuals at collocation points $x_j = \cos(\pi j/N_c)$, $j = 0, 1, 2, ..., N_c$ equal to zero. The unknowns are then the Fourier spectral values of the variables of interest at the $N_c + 1$ collocation points, i.e. $\widehat{\phi}^k(x_j)$, $\widehat{\omega}^k(x_j)$ and $\widehat{\psi}_2^k(x_j)$, for $j = 0, 1, ..., N_c$, and at each time step k.

The nonlinear terms in Eqns. 3.30—3.33 were calculated using the pseudo-spectral technique [59], which consists of performing the differentiations in spectral space and

the products in physical space. Both spaces are connected computationally by a Fast Fourier Transform (FFT). Then Eqn.3.39 can be simplified to an ODE:

$$
\left(4\frac{d^2}{dx^2} + \frac{2}{\frac{x_i}{2} + (r'_i + \frac{1}{2})}\frac{d}{dx} - \frac{m^2}{[\frac{x_i}{2} + (r'_i + \frac{1}{2})]^2} \right) \widehat{\phi}_m^{k+1}(x_i) = -\widehat{\omega}_m^{k+1}(x_i), \qquad (3.48)
$$

where $r'_i = \frac{\alpha}{1-\alpha} = r_i/d$ and $x_i = \cos\frac{\pi i}{N_c}$, $i = 0,\ 1,\ 2, ..., \ N_c$. We can express the derivatives of variables, denoted by the superscripts, at the collocation points by an algebraic matrix representation [59]:

$$
u_N^{(p)}(x_i) = \sum_{j=0}^{N} d_{ij}^{(p)} u_N(x_j), \ \ i = 0, 1, ..., N.
$$
$$
U^{(1)} = DU, \quad U^{(2)} = D^2 U, \quad U = (u_N(x_0), \ \ ..., \ u_N(x_N))^T,
$$

where D is the Chebyshev spectral differentiation matrix of $(N+1)\times(N+1)$ elements and the entries are

$$
\begin{aligned}
D_{00} &= \frac{2N^2+1}{6}, \quad D_{NN} = -\frac{2N^2+1}{6}, \\
D_{jj} &= \frac{-x_j}{2(1-x_j^2)}, \quad j = 1, ..., N-1, \\
D_{ij} &= \frac{c_i}{c_j}\frac{(-1)^{i+j}}{(x_i-x_j)}, \quad i \neq j, \quad ij = 0, ..., N, \\
c_i &= 2, \quad \text{for} \quad i = 0 \text{ or } N, \quad c_i = 1, \quad \text{otherwise.}
\end{aligned}
$$

With the above differentiation matrix, the Laplace differentiation operator $\mathcal{L}_{op}$ in cylindrical coordinates is approximated as follows:

$$
\begin{aligned}
\mathcal{L}_{op} &\equiv 4\frac{d^2}{dx^2} + \frac{2}{\frac{x_i}{2} + (r'_i + \frac{1}{2})}\frac{d}{dx} - \frac{m^2}{[\frac{x_i}{2} + (r'_i + \frac{1}{2})]^2} \\
&\approx 4D^2 + \frac{2}{\frac{x_i}{2} + (r'_i + \frac{1}{2})}D - \frac{m^2}{[\frac{x_i}{2} + (r'_i + \frac{1}{2})]^2}.
\end{aligned} \qquad (3.49)
$$

Hence, the continuous differential Eqn.3.39 for the streamfunction can be simplified

to a set of algebraic equations of the unkowns $\widehat{\phi}_m^k, \widehat{\omega}_m^k, \widehat{q}_m^k$ and $\widehat{\psi}_{2m}^k$, at the collocation points x_i ($i = 0, 1, ..., N_c$), for each Fourier mode m at each time step k:

$$\mathcal{L}_{op} \, \widehat{\phi}_m^{k+1}(x_i) = -\widehat{\omega}_m^{k+1}(x_i). \tag{3.50}$$

By the same token, the corresponding ODEs for 2D electric potential and vorticity for each Fourier mode m, using the AB/BDI2 time discretization scheme, are

$$\widehat{q}_m^{k+1}(x_i) - \frac{2\Delta t}{3}\mathcal{L}_{op}\widehat{\psi}_m^{k+1}(x_i) = \frac{4}{3}\widehat{q}_m^k(x_i) - \frac{1}{3}\widehat{q}_m^{k-1}(x_i) - \frac{2\Delta t}{3}\left(2\widehat{\mathcal{J}}_{q,\phi}^k - \widehat{\mathcal{J}}_{q,\phi}^{k-1}\right)_{x=x_i}^m \tag{3.51}$$

$$\left(\mathcal{I} - \frac{2\mathcal{P}\Delta t}{3}\mathcal{L}_{op}\right)\widehat{\omega}_m^{k+1}(x_i) = \frac{4}{3}\widehat{\omega}_m^k(x_i) - \frac{1}{3}\widehat{\omega}_m^{k-1}(x_i) - \frac{2\Delta t}{3}\left(2\widehat{\mathcal{J}}_{\omega,\phi}^k - \widehat{\mathcal{J}}_{\omega,\phi}^{k-1}\right)_{x=x_i}^m$$
$$+ \frac{2\Delta t}{3}\mathcal{P}\mathcal{R}\left(2\widehat{\mathcal{J}}_{\psi,q}^k - \widehat{\mathcal{J}}_{\psi,q}^{k-1}\right)_{x=x_i}^m, \tag{3.52}$$

where $\mathcal{I}$ is the identity matrix and $\widehat{\mathcal{J}}^k|_{x=xi}^m$ is the Fourier spectral coefficient of Jacobian terms of mode m at the collocation point x_i at current time step k.

Alternatively, the semi-implicit first order Euler differenentiation scheme (described in the previous section) was used. With the Fourier-Galerkin and Chebyshev collocation methods, the corresponding ODEs are

$$\widehat{q}_m^{k+1}(x_i) - \Delta t\mathcal{L}_{op}\widehat{\psi}_m^{k+1}(x_i) = \widehat{q}_m^k(x_i) - \Delta t\left(\widehat{\mathcal{J}}_{q,\phi}^k\right)_{x=x_i}^m, \tag{3.53}$$

$$(\mathcal{I} - \mathcal{P}\Delta t \, \mathcal{L}_{op})\widehat{\omega}_m^{k+1}(x_i) = \widehat{\omega}_m^k(x_i) - \Delta t\left(\widehat{\mathcal{J}}_{\omega,\phi}^k\right)_{x=x_i}^m + \Delta t \, \mathcal{P}\mathcal{R}\left(\widehat{\mathcal{J}}_{\psi,q}^k\right)_{x=x_i}^m \tag{3.54}$$

$$\mathcal{L}_{op}\widehat{\phi}_m^{k+1}(x_i) = -\widehat{\omega}_m^{k+1}(x_i). \tag{3.55}$$

The ODEs, together with Maxwell's equation, are numerically solved for the local flow fields, surface charge and electric potential, to shed light onto the dynamics of electroconvection. The simulation protocol includes the nonlocal simultaneous mapping between electric potential and surface charge via Maxwell equations. Unlike the temperature field in thermal convection, the dynamics of surface charge is not only

coupled to flow motion but also determined by the 2D electric potential. Thus, the numerical calculations for smectic electroconvection is more complicated than those for Rayleigh-Bénard convection. An approach, fully described in the next section, was established to work out the simultaneous mapping between q and ψ_2.

With the proper initial conditions, boundary conditions, and time-stepping size, the 2D electric potential ψ_2 is first calculated. Simultaneously, the surface charge q via the nonlocal mapping is obtained. Then, the vorticity ω field can be obtained using newly found q and ψ_2, and finally the streamfunction ϕ can be found via Eqn.3.50. When dealing with the nonlinear Jacobian terms, we perform the 3/2-rule aliasing removal technique to remove aliased Fourier spectral coefficients [59].

3.3.3 The closure relation between surface charge and electric potential

Smectic electroconvection deals with a nonlocal, coupled electrical body force which involves a Maxwell's equation connecting the surface charge q with the electric potential ψ (as described by Eqns. 3.5—3.7). The buoyancy force in Rayleigh-Bénard convection is merely a local relationship between gravity and the density differences due to the imposed temperature gradient. As a consequence, the details and procedures of the numerical simulations for electroconvection are more complicated than those for Rayleigh-Bénard convection problems. This section presents a crucial intermediate calculation of the simultaneous mapping between q and ψ_2 to simplify the implementation of the simulation code for smectic electroconvection.

The surface charge density q and the 2D electric potential on the film ψ_2 are nonlocally related. Either of these two quantities, plus the 2D potential on the electrodes, form the boundary conditions for the 3D Laplace equation that determines the potential outside the film. The remaining 2D quantity must be determined self-

consistently from the solution of the 3D Laplace problem. This nonlocal relationship makes the simulation of electroconvection more difficult than that of thermally driven Rayleigh-Bénard convection. The additional complication is evident by the coupling of four unknown quantities in the governing equations, instead of the usual three for Rayleigh-Bénard convection problem. Fortunately, the additional potential and charge fields are coupled instantaneously by a Maxwell equation, so that the nonlocal calculation involves no additional time derivatives, and can thus be solved once and for all before time stepping the other fields. This calculation must ultimately be done numerically, but the Laplace problem can first be solved implicitly in integral form. The calculation is made more straightforward by the decomposition of the fields into Fourier modes in the pseudo-spectral technique.

The 3D potential ψ satisfies the Laplace Equation $\nabla^2 \psi = 0$ with appropriate boundary conditions (BCs) on the film and electrodes because no free charge exists outside of the film. The surface charge density q is determined by the discontinuity of ψ in the $\hat{\mathbf{z}}$ direction on the surface of the film. The BCs require that ψ in charge-free space is finite for $z \geq 0$ and vanishes for $z \to \infty$. General solutions for $z \geq 0$ are

$$\psi(r, \theta, z) = \sum_{m=-\infty}^{\infty} \int_0^{\infty} e^{-kz} J_m(kr) \, A_m(k) e^{im\theta} \, dk, \tag{3.56}$$

$$\begin{aligned} q(r, \theta) &= -2\partial_z \psi|_{z=0^+} \\ &= 2 \sum_{m=-\infty}^{\infty} \int_0^{\infty} k \, e^{-kz} J_m(kr) \, A_m(k) e^{im\theta} \, dk \Big|_{z=0^+}, \\ &= \sum_{m=-\infty}^{\infty} \widehat{q}_m(r) e^{im\theta} \approx \sum_{m=-K}^{K} \widehat{q}_m(r) e^{im\theta}, \end{aligned} \tag{3.57}$$

where J_m is the Bessel function of the first kind [61]. In the above, the pseudo-spectral expansion in the azimuthal modes was used to numerically estimate the surface charge using modes m in the finite range $-K \leq m \leq K$. K is selected to be sufficiently large that spectral contribution of modes with $m > K$ is negligible.

The BC for the electric potential on the surface of the film is $\psi_2(r, \theta) = \psi(r, \theta, z = 0)$, and

$$
\begin{aligned}
\psi_2(r, \theta) &= \sum_{m=-\infty}^{\infty} \int_0^{\infty} J_m(kr) \, A_m(k) e^{im\theta} \, dk, && (3.58) \\
&= \sum_{m=-\infty}^{\infty} \widehat{\psi}_{2m}(r) e^{im\theta} \approx \sum_{m=-K}^{K} \widehat{\psi}_{2m}(r) e^{im\theta}.
\end{aligned}
$$

The coefficients $A_m(k)$ can be calculated with the aid of the Hankel transform,

$$
\int_0^{\infty} x J_m(kx) J_m(k'x) \, dx = \frac{1}{k}\delta(k' - k). \tag{3.59}
$$

Using Eqn. 3.59, one can solve for the coefficient

$$
A_m(k) = k \int_0^{\infty} \rho \, \widehat{\psi}_{2m}(\rho) \, J_m(k\rho) \, d\rho. \tag{3.60}
$$

Using the above formulation, the nonlocal relationship between the Fourier coefficients of the surface charge q and the 2D electric potential ψ_2 is given by the following integral equation:

$$
\widehat{q}_m(r) = 2 \int_0^{\infty} k^2 \, J_m(kr) \int_0^{\infty} \rho \, \widehat{\psi}_{2m}(\rho) \, J_m(k\rho) \, d\rho \, dk. \tag{3.61}
$$

This expression is simplified by the fact that $\widehat{\psi}_{2m}(\rho) = 0$ for $\rho < r_i$ and $\rho > r_o$, so the range of the ρ integration can be restricted to $r_i \leq \rho \leq r_o$.

Looking back to Eqn. 3.56, we see that the wave number k describes how rapidly the integrand of ψ_3 exponentially decreases in the z direction. Therefore, the k integration in Eqn. 3.61 can be approximated with a large but finite upper limit k_{max}. To carry out the k integral numerically, one can approximate it as a Riemann sum using a small step δk, with $k_n = n\delta k$ and $0 \leq n \leq N_k = k_{max}/\delta k$.

In the pseudo-spectral method, we only need to evaluate Eqn. 3.61 at the $N_c +$ 1 Chebyshev collocation points in the radial direction. As described previously in Section 3.3.2, $N_c + 1$ radial positions r are mapped onto x positions using Eqn. 3.47, with $x_j = \cos(\pi j/N_c)$, $j = 0,\ 1,\ 2, ...,\ N_c$. The ρ integration in Eqn. 3.61 can be similarly approximated by a sum so that

$$\widehat{q}_m(x_i) \approx 2 \sum_{n=0}^{N_k} k_n^2\ J_m(k_n x_i) \sum_{j=0}^{N_c} r_j\ \widehat{\psi}_{2m}(x_j)\ J_m(k_n x_j)\ \delta r_j\ \delta k, \tag{3.62}$$

where δr_j is an appropriately chosen variable interval. Carrying out the sum over n, this can be expressed as a nonlocal, linear transformation between the Fourier-Chebyshev coefficients of $\widehat{q}_m$ and $\widehat{\psi}_{2m}$,

$$\widehat{q}_m(x_i) = \sum_{j=0}^{N_c} T_{ij}^m \widehat{\psi}_{2m}(x_j). \tag{3.63}$$

The used k-stepping size was $\delta k = 10^{-3}$. It remains to select an appropriate cutoff k_{max}. The best value of k_{max} was found to be related to the choice of maximum Fourier mode $m = K$. We found that $k_{max} \sim (1.5 - 2) \times K$ was sufficient. Varying k_{max} introduces only very small errors. The integrated charge transport Nu differs by $\leq 0.3\%$ at $\mathcal{R} = 160$ for simulations with $k_{max} = 40,\ 50,\ 58$ and 70. The typically used value of k_{max} is 50 to calculate the matrices T_{ij}^m for each Fourier mode m. The matrix elements depend only on α, N_c and k_{max}, and were calculated once at the beginning of the time stepping loop. Eqn. 3.63 was used thereafter to convert $\widehat{\psi}_{2m}$ to $\widehat{q}_m$.

The calculation of the simultaneous mapping of $\widehat{\psi}_{2m}$ and $\widehat{q}_m$ is specific and essential to the simulation for smectic electroconvection. This step effectively simplifies the problem (of originally four unknowns) to have three freely variables and an instantaneous dependent field. Therefore, after this numerical calculation, the implementation

of the simulation code becomes more straightforward and the rest of calculations can resemble standard simulations for Rayleigh-Bénard convection.

Next section describes the employed key numerical parameters, such as initial conditions, boundary conditions, grid resolution, convergent criteria, and the integrated physical quantities of interest.

3.3.4   Numerical parameters

The simulation mimics the procedure of electroconvection experiment by gradually increasing $\mathcal{R}$ in small increments separated by many time steps, starting from the conduction state, passing through the onset of convection at $\mathcal{R}_c$. For $\mathcal{R} < \mathcal{R}_c$, the implemented initial conditions such that $\phi = 0$, so that the fluid was quiescent. The electric potential ψ_2 was given by random white noise with amplitude in the range $10^{-5} - 10^{-4}$. For $\mathcal{R} > \mathcal{R}_c$, the initial conditions were the converged, statistically steady numerical solutions at the previously calculated $\mathcal{R}$. To avoid a numerical instability in the computation, the time-stepping interval Δt was limited to be smaller than $9/(Nc+1)^2$, where N_c is the number of Chebyshev grids [59]. Typically, the employed Δt is around 10^{-3} in the laminar convection regime, whereas $\Delta t \sim 10^{-7} - 10^{-6}$ for $\mathcal{R} \approx 10^4$, which is more restricted, in the turbulent regime .

The radial boundary conditions applied to the Fourier coefficients for all modes m were

$$\widehat{\phi}_m = \frac{d}{dr}\widehat{\phi}_m = \widehat{\psi}_{2m} = 0, \quad \text{for} \quad r = r_o', \, r_i' \tag{3.64}$$

To enforce the rigid boundary condition on the streamfunction ϕ in Eqn. 3.64, we used the influence matrix method [58, 59] to calculate the corresponding Dirichlet boundary condition on the vorticity ω. This method remedies the doubly-specified boundary conditions for streamfunction (its value and its derivative at the boundary). The concept and the technique of the influence matrix method are comprehensively

explained in Appendix B.

3.3.5 Integrated physical quantities of interest

The electric Nusselt number Nu is a dimensionless measure of the ratio of the total current to the conductive current transported by diffusion process. It is the electrical analog of the thermal Nusselt number which characterizes the total heat transport in Rayleigh-Bénard convection [2].

Nu is defined to be the ratio of the total current to the conductive current. The azimuthal components of the current density average to zero around the annulus, leaving only the radial contribution, which can be integrated to give

$$Nu \equiv \frac{\oint \mathbf{J} \cdot \hat{\mathbf{r}} \, dl}{\oint \mathbf{J_{cond}} \cdot \hat{\mathbf{r}} \, dl} = \frac{\int_0^{2\pi} (u_r q - \partial_r \psi_2) \, r d\theta}{\int_0^{2\pi} (-\partial_r \psi_2^{(0)}) \, r d\theta}, \tag{3.65}$$

where $\mathbf{J}$ is the current density containing convective and conductive contributions and $\mathbf{J}_{cond}$ is the conductive current density. Taking advantage of the zero radial velocity at the boundaries to simplify Eqn. 3.65, Nu can be computed numerically from

$$Nu = 1 + \left[r \log(\alpha) \frac{d}{dr} \widehat{\psi}_{2m=0}^{(1)}(r) \right]_{r=r_i}. \tag{3.66}$$

The term in the square brackets can be taken at either r_i or r_o. Nu is directly related to the physical currents that can be measured experimentally [1, 49, 52, 54, 55, 56]. It is also a direct measure of the amplitude of the convective velocity.

We also calculated the mean area density of the kinetic energy

$$E_{kin} = \frac{1}{2a} \int_{r_i}^{r_o} \int_0^{2\pi} \vec{\mathbf{u}} \cdot \vec{\mathbf{u}} \, r dr d\theta, \tag{3.67}$$

where a is the dimensionless area of the annulus. E_{kin} is a useful diagnostic of the strength of convection.

To test the convergence of the time stepping code onto a statistically steady state solution, we calculated the changes in Nu and E_{kin}, as well as the norm of the change in Fourier coefficients between one time step and the previous one. The solutions in the weakly nonlinear regime were considered converged not only when the norm was less than 10^{-5} but also the changes in Nu and E_{kin} were $\leq 0.05\%$. In the chaotic regime, the numerical solutions were calculated with different Δt and spatial resolutions, and Nu and E_{kin} were also checked to ensure they reached statistically steady values.

3.3.6 Grid resolution

Overall, the numerical method described above is extremely conservative and stable, yet is still efficient enough that we can reach $\mathcal{R} \sim 1000$ with only modest computational effort. For instance, in the laminar convection regime, very good spatial resolution is achieved with moderate Fourier modes between $K = 16$ and $K = 32$ and the Chebyshev order $16 \leq Nc \leq 39$. However, to resolve fine flow structures in the turbulent regime, appropriate grid sizes needed to be comparable to the Kolmogorov scale which represents the finest vortex scales. The Kolmogorov dissipation length scale δ is given by

$$\frac{\delta}{d} = \frac{1}{d} \left(\frac{\tilde{\nu}^3}{\epsilon_u} \right)^{1/4}, \tag{3.68}$$

where d is a characteristic length scale such as the length of a convection cell, $\tilde{\nu}$ is the 2D kinematic viscosity, and ϵ_u is kinetic dissipation rate [62]. In electroconvection, the kinetic dissipation rate, as discussed in detail in the next chapter, Section 4.3.2, is

$$\epsilon_u = \frac{\tilde{\nu}^3 \mathcal{R} \mathcal{P}^{-2} (Nu - 1)}{F(\alpha) \cdot d^4}, \quad F(\alpha) = \ln\left(\frac{1}{\alpha}\right) \frac{1 + \alpha}{1 - \alpha} \sim O(1). \tag{3.69}$$

Hence, to resolve the finest dissipation scale, we estimate a suitable grid size in accordance with [63]

$$\frac{\delta}{d} = \frac{1}{d}\left(\frac{\tilde{\nu}^3}{\epsilon_u}\right)^{1/4} \sim \left(\frac{\mathcal{P}^2}{\mathcal{R}Nu}\right)^{1/4}. \tag{3.70}$$

In electroconvection, the experimental measurements of Nu and the parameters $\mathcal{R}$ and $\mathcal{P}$ for high $\mathcal{R} \approx 10^6$ suggest the appropriate grid numbers d/δ are 40 in the radial direction and between 40 and 64 in the azimuthal directions, respectively. 1.5 times higher resolution than the aforementioned grid numbers was employed first and then various even higher order modes were computed and compared as well. In addition, the Nu calculations with different grid resolutions were checked to reach statistically steady values and to make sure the simulations were well resolved.

3.4 Validation of simulation codes

The code was validated by simulating weakly forced conditions near the onset of convection. The quantitative numerical results for the critical Rayleigh number $\mathcal{R}_c$ at onset were benchmarked and found to be in better than 2% agreement with the predictions of linear stability theory [38].

The annular geometry, described by the radius ratio α, has various profound effects on the critical Rayleigh number $\mathcal{R}_c$ and the critical number of vortex pairs m_c at the onset of convection, both of which were predicted by linear theory [38] and measured experimentally [54]. For $\mathcal{R} > \mathcal{R}_c$, nonlinear effects are manifest. For zero applied shear, the base state for annular electroconvection has reflection symmetry and a continuous symmetry under azimuthal rotations. Based on the symmetry argument described below, a generic Landau amplitude equation describes the neighborhood of the primary bifurcation in the weakly nonlinear regime [3]. The appropriate amplitude equation A of an underlying physical field for smectic electroconvection is invariant under the transformations of rotation $\theta \to \theta + \theta'$, $A \to A\exp(im\theta')$ and of reflection

$\theta \to -\theta$, $A \to A^*$. Here, θ is an azimuthal angle and A^* is the complex conjugate of the amplitude A. The amplitude A of an underlying physical field is usually a complex number. Its real and imaginary parts are often treated separately. One can also derive the corresponding amplitude equation from microscopic field equations starting from the Navier-Stokes equations [55]. In general, the complex Ginzburg-Landau equation describes the evolution of amplitudes of unstable modes for smectic electroconvection. This complex amplitude description can display rich dynamical patterns and it is used for a variety of physical systems including superconductivity, nonlinear waves, second-order phase transitions, and some convection systems (see Ref. [64] for a good review). The application of the amplitude description for annular electroconvection is described below.

The amplitude equation for steady electroconvection in the absence of shear—describing a stationary bifurcation—is real and time independent:

$$\partial_t A = \epsilon A - gA|A|^2 - hA|A|^4 + f = 0, \tag{3.71}$$

where A is the amplitude of the underlying fields; for example, the amplitude of convection which is proportional to to the magnitude of radial velocity. The amplitude A can be expressed in terms of the reduced Nusselt number [36] so that $|A|^2 = Nu - 1$. Alternatively, $|A|^2 \propto E_{kin}$ or A can directly be the Fourier amplitude of the physical field of interest for the unstable modes (with some appropriate rescaling). $\epsilon = (\mathcal{R}/\mathcal{R}_c) - 1$ is the reduced control parameter. It is a convenient measure of the distance from the critical threshold at which convection sets in. The value of ϵ should be small to fulfill the Landau amplitude description near a bifurcation—a sharp transition (at $\epsilon = 0$) from the state $A = 0$ for $\epsilon < 0$ to the state $|A| > 0$ for $\epsilon > 0$. The coefficient g of the cubic nonlinear term determines whether the bifurcation to electroconvection is continuous (supercritical) for $g > 0$, discontinuous (subcritical) for $g < 0$, or tricritical

for $g = 0$. The quintic term h models a nonlinear saturation for stationary patterns such that $h > 0$. For a subcritical bifurcation ($g < 0$), a positive quintic term ensures a steady, spatially organized pattern. The simulation data revealed that the primary bifurcation is supercritical for wide parameter ranges of α and $\mathcal{P}$. Thus, the quintic term h plays a minor role here and its value was found by simulation to be $h \approx 5$. The field term f allows for some imperfection in the bifurcation and was found to be necessary to realistically model small symmetry-breaking imperfections in the real laboratory experiment [54]. In contrast, in simulations f was found to be essentially zero.

Mimicking the analysis used previously on real experimental data [54], $\mathcal{R}_c$, g, h and f are determined by fitting the numerical data for $Nu - \mathcal{R}$ to Eqn. 3.71 using a nonlinear least squares method. The $\mathcal{R}_c$ found with this method agrees well with the $\mathcal{R}_c$ estimated with a linear approximation, using the growth rates of convection at some Rayleigh numbers $\mathcal{R}$ very close to $\mathcal{R}_c$. The dependence of $\mathcal{R}_c$, m_c, and g was numerically investigated over a broad parameter space of α and $\mathcal{P}$, large compared to the accessible range in previous theoretical and experimental work.

3.4.1 Dependence on the Rayleigh number $\mathcal{R}$

The numerical model follows the experimental protocol of ramping $\mathcal{R}$ slowly up and down through onset. Experimentally, this is done by increasing and decreasing the applied voltage.

Fig. 3.1a shows the dimensionless current carried by convection, $Nu - 1$, as the control parameter $\mathcal{R}$ varies. Zero convective current indicates the conduction regime in which dissipation effects dominate and prevent convection even under the electric forcing. As $\mathcal{R}$ slowly increased, we observed a critical threshold showing the onset of convection at $\mathcal{R}_c$. A critical slowing down, indicated by extremely long convergence times, occurs near this bifurcation. A slight hysteresis due to dynamical effects was

observed . It is well known both analytically and experimentally that a bifurcation point is shifted when a control parameter is swept through a bifurcation at a finite rate [65]. We allow for critical slowing down by greatly increasing the computational time allotted to reach the convergence criterion. However, a small residual delay in the bifurcation with increasing $\mathcal{R}$ is still observable in Fig. 3.1b, which shows the amplitude of convection A vs. $\mathcal{R}$.

Above $\mathcal{R}_c$ a pattern of stationary convective vortices forms carrying extra current and breaks the continuous symmetry under azimuthal rotation. Convection remains steady in the weakly nonlinear regime up to $\mathcal{R} \sim 5\mathcal{R}_c$. Fig. 3.2 shows surface charge distribution and the corresponding velocity field for steady convection in which the laminar flow provides a constant contribution to the electric current. The corresponding streamfunction ϕ and perturbed electric potential $\psi_2^{(1)}$ are shown in Fig. 3.3. From these figures, we see positively charged regions which are being carried by the flow towards the grounded outer electrode, separated by negatively charged regions returning. These local convective currents add to the total current and act to reduce the applied potential gradient. The simulation provides insightful visualizations of the local fields that nicely complement the physical experiments in which these fields could not be visualized. This new insight will play an important role in understanding more complicated bifurcations at higher $\mathcal{R}$, eventually into the turbulent regime [49, 56], and the complex rotating states that occur under an applied shear [1, 54, 55].

3.4.2 The critical Rayleigh number $\mathcal{R}_c$

$\mathcal{R}_c$, which indicates the onset of convection, was calculated in order to validate the simulation code by benchmarking numerical data against $\mathcal{R}_c$ and the critical azimuthal mode m_c found by previous theoretical calculations. Fig. 3.4a shows the α dependence of $\mathcal{R}_c$ from numerical computations and from linear stability theory [38]. The trend of $\mathcal{R}_c$ in the numerical data is increasing overall as a function of the radius
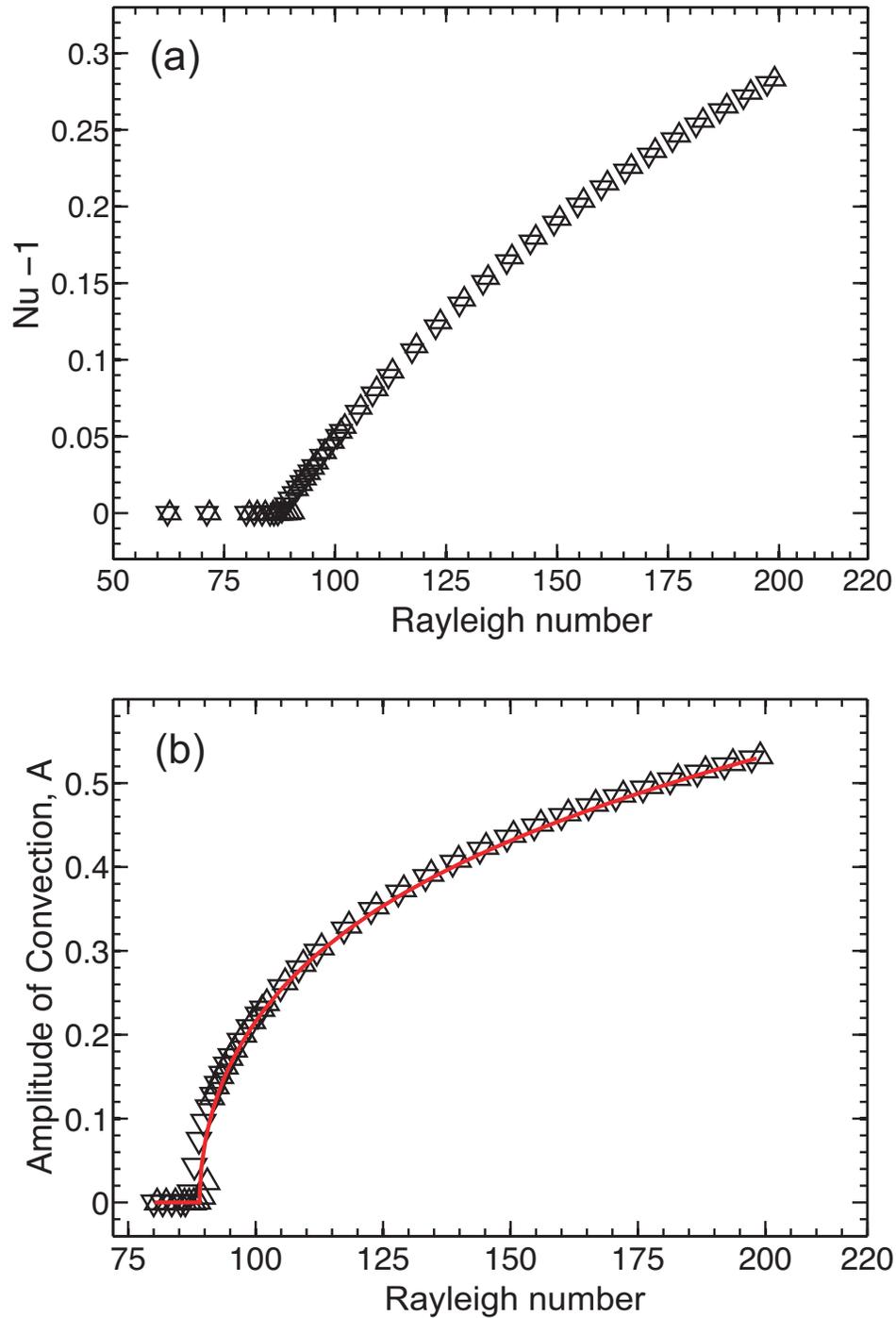
Figure 3.1: Numerical data for the dimensionless convective current, Nu − 1, as a function of the Rayleigh number $\mathcal{R}$, for $\alpha = 0.56$ and $\mathcal{P} = 10$. Data obtained for increasing (decreasing) $\mathcal{R}$ are shown as $\triangle$ ($\triangledown$). (b): The corresponding amplitude of convection $A = \sqrt{Nu - 1}$ as a function of $\mathcal{R}$. The solid line is a nonlinear least-squares fit of the data to the Landau equation given by Eqn. 3.71.
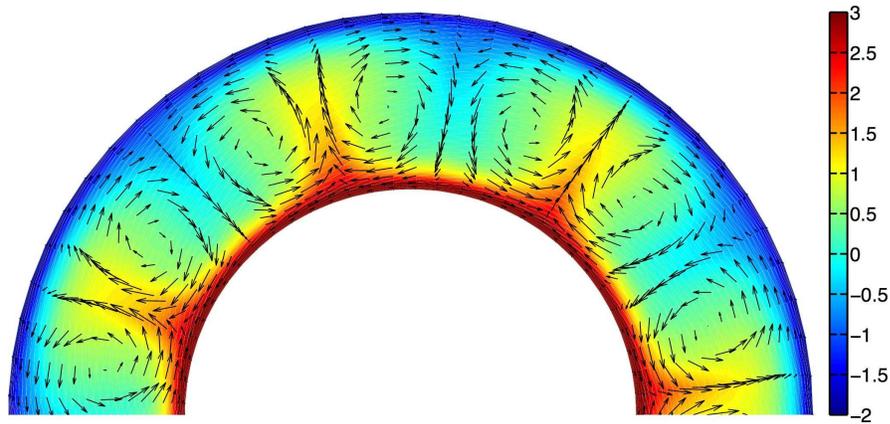
Figure 3.2: The basic fields for steady convection at $\mathcal{R} = 199.8$, $\alpha = 0.56$, $\mathcal{P} = 10$: the total electric charge density q (colour) and the velocity field (black). Only the upper half of the annular cell is shown. Positive charge moves away from the high potential electrode at the inner radius, while negative charge moves away from the grounded outer electrode.
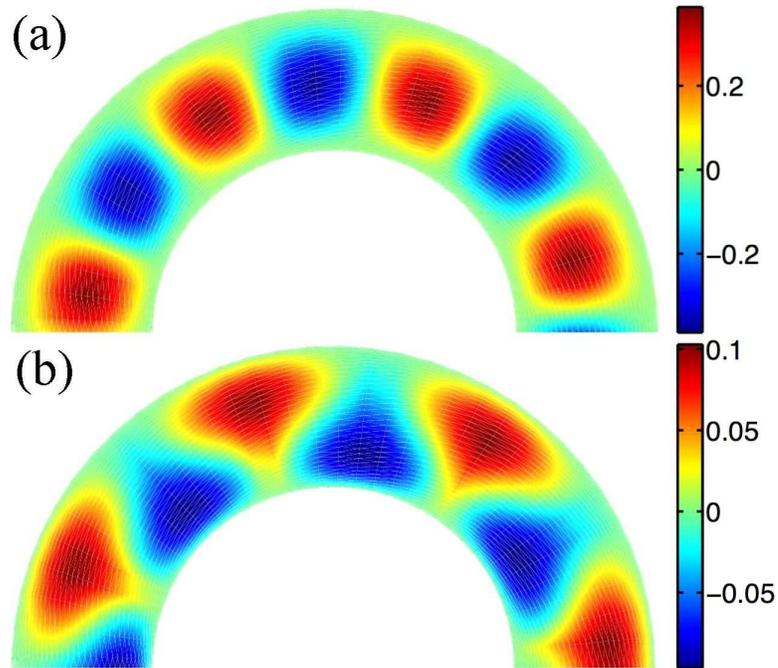
Figure 3.3: (a) The streamfunction and (b) the perturbed 2D electric potential $\psi_2^{(1)}$, for the same control parameters are as in Fig. 3.2. For this specific α, the state is dominated by the $m = 7$ Fourier mode and there are seven counter-rotating vortex pairs.

ratio and quantitatively agrees with a fully nonlocal theory calculation shown by the solid line [38].

Several values for the Chebyshev orders N_c and the Fourier modes K were used in the simulations; they range between 29 and 45 and between 32 and 64, respectively. Numerical data with different values of N_c and K agree with each other to within a small scatter. The error bars in Fig. 3.4a were obtained from the spread of numerical data and were calculated using different time step sizes, random initial conditions, grid sizes, and time discretization approximations. Each data point consists of at least three complete sets of numerical runs, sweeping the voltage up and down.

The calculation becomes more difficult for small α, due the increasing asymmetry between the inner and outer electrodes. The smallest α range explored with reasonable accuracy is down to $\alpha = 0.1$. This is well below the minimum radius reached by previous experiments in the weakly nonlinear regime, which corresponded to $\alpha = 0.33$. Various truncations also limit the range of the nonlocal linear stability theory [38] to $0.33 \leq \alpha \leq 0.8$. Although its accuracy is somewhat compromised, the numerical code remains very stable and can be thus used to broaden the range of α accessible. At the smallest α, $m_c = 2$ and there are just four vortices around the annulus.

In general, the main effect of varying α is to select the overall azimuthal mode, which is quantized to fit an integer number of vortex pairs around the perimeter of the annular cell. Fig. 3.4b shows critical mode number m_c from the simulation, linear theory, and experiment [38]. For special values of α, two adjacent values of azimuthal mode number are simultaneously unstable at onset and $\mathcal{R}_c(\alpha)$ exhibits a cusp, giving it a scalloped structure. These are the special co-dimensional two (CoD2) points which we discuss in detail in Chapter 5, Section 5.1.3.

The code has been validated and showed an excellent agreement on $\mathcal{R}_c$ and m_c found by previous linear stability theory. In Chapter 5, we use this code to study the dependence of steady laminar convection on α and $\mathcal{P}$ and to investigate various

bifurcations in sheared convection. We also extended the code to study turbulent convective states in which Nu scaling, as observed in experiment, is expected. The next chapter describes a theory for this scaling in the high Rayleigh number regime.
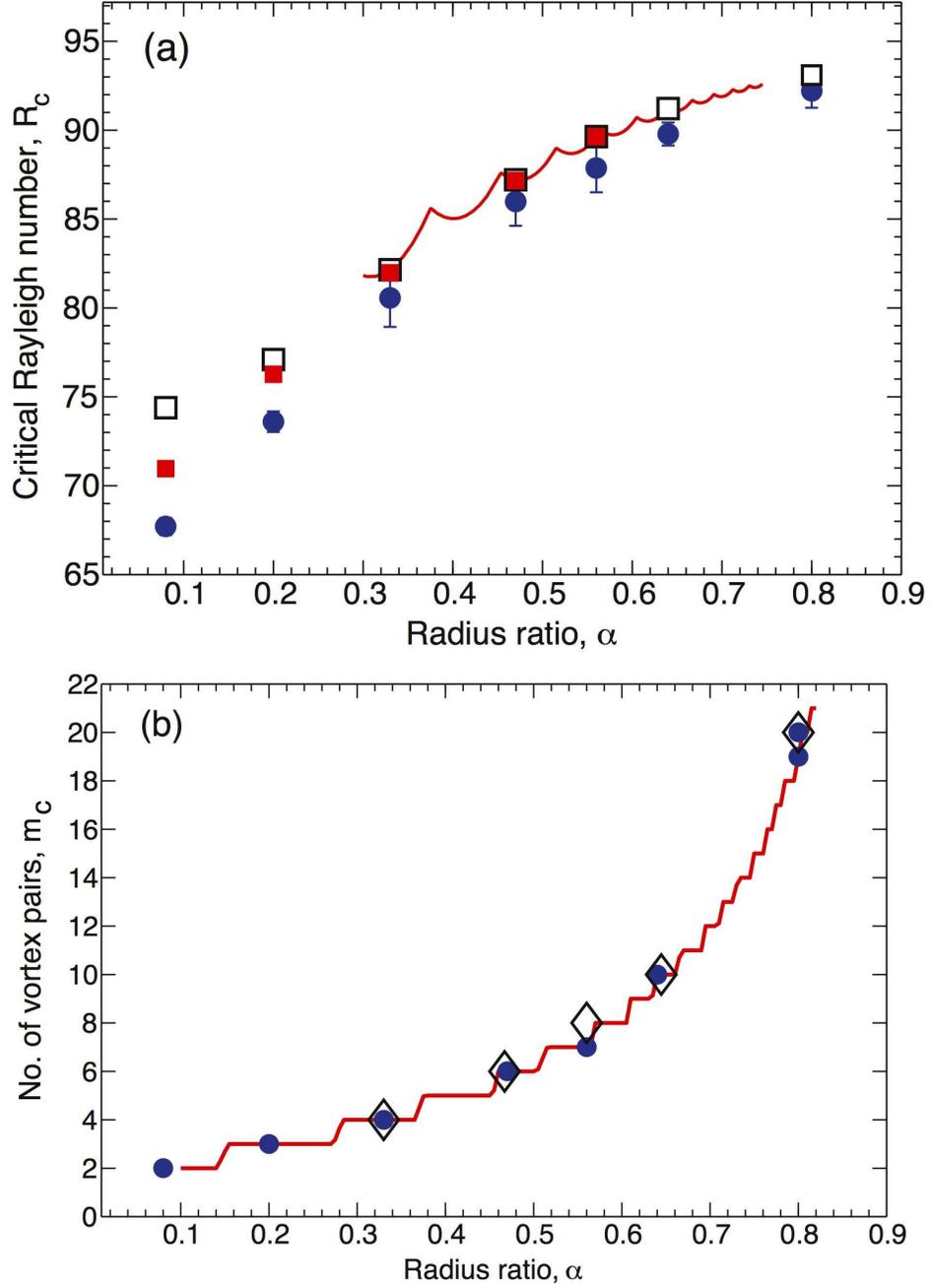
Figure 3.4: The radius ratio dependence of the critical Rayleigh number $\mathcal{R}_c$ in (a). The solid circles ($\bullet$) are the results of the numerical simulation. Open and filled boxes ($\square$) are the theoretical predictions of nonlocal linear stability analysis by V. B. Deyirmenjian, using third order and sixth order expansions in the radial direction, respectively. (b) The critical number of counter-rotating vortex pairs m_c. All the simulation data ($\bullet$) are for a fixed $\mathcal{P} = 10$. The solid lines are the predictions of fully nonlocal linear stability theory and $\diamondsuit$ are experimental results from Ref. [54].

Chapter 4

Scaling theory

4.1 Introduction

This chapter describes a scaling theory for charge transport in turbulent electro-convection. The theoretical investigation aims at understanding the scaling relation between Nu and $\mathcal{R}$ found in the electroconvection experiment, described in Chapter 2, by adapting a modern systematic theory for turbulent Rayleigh-Bénard convection.

For a century, theories of turbulent Rayleigh-Bénard convection have focused on understanding the globally averaged heat transport, described by the dimensionless Nusselt number Nu. The development of models has been inspired by improved experimental measurements of the heat current, which have revealed unexplained discrepancies with existing theories. In response, mathematical models have become increasingly sophisticated during the past five decades [25]. Good reviews on earlier experimental, theoretical, and numerical work can be found in Ref [25, 26, 27]. In recent years, ambitious experimental, theoretical, and numerical projects have been undertaken and the study of turbulent Rayleigh-Bénard convection has been considerably reinvigorated and actively ongoing. Among various theories, a contemporary unifying theory by S. Grossmann and D. Lohse in 2000 (hereafter referred to as the

GL theory) has shown to be in good agreement with many experimental data over a wide parameter range [32].

The GL theory systematically predicts the scaling of the Nusselt number Nu and of the Reynolds number Re in strong thermally driven Rayleigh-Bénard convection. The main idea underlying the theory is the decomposition of global thermal and viscous dissipation rates, which are balanced with their dominant contribution from the boundary layers or the bulk. It assumes the existence of a large scale turbulent wind stirring the bulk, which is observed in various experiments [25, 30, 66, 67, 68, 69, 70]. The effect of this large scale circulation is twofold: (1) the turbulent wind stirs the fluid in the bulk so that the velocity fluctuations here are influenced by the turbulent wind; (2) shear flow boundary layers build up between the wind and the cell walls. Several regimes of local power-laws $\text{Nu} \propto \text{Ra}^\gamma \text{Pr}^\beta$ and $\text{Re} \propto \text{Ra}^{\gamma*} \text{Pr}^{\beta*}$ are predicted, depending on the parameter space of Rayleigh (Ra) and Prantl (Pr) numbers. As described in Chapter 1, Ra is the control parameter, proportional to the imposed temperature gradient ΔT, and Pr is a fluid parameter. These regimes are identified by whether the boundary layer or the bulk dominates the global kinetic and thermal dissipation, respectively.

As part of thesis work, the charge transport scaling theory for turbulent annular electroconvection was constructed by applying the GL theory and extending it to account for geometric effects. The idea of this theoretical study rests upon the close similarity of the convective instabilities found in electroconvection and thermal convection. The charge transport in electroconvection under an applied voltage is analogous to the heat flux in Rayleigh-Bénard convection with an imposed temperature difference. Hence, annular electroconvection is a good analog to test and apply the GL scaling theory. In the following, the GL theory, which only considers the unit aspect ratio case, is briefly reviewed and discussed in Section 4.2. Then, Section 4.3 fully describes the electrical version of the scaling theory for turbulent

annular electroconvection with an arbitrary aspect ratio.

4.2 Heat transport scaling in turbulent thermal convection

This section first describes the phenomenological observations of turbulent Rayleigh-Bénard convection, which are the main ingredients in the GL theory. This theory is then described with the focuses on its assumptions, methods, and predictions. Later on, the theoretical results are compared with various recent experimental and numerical data. This section ends with further implications and some limitations of the GL theory.

Turbulent Rayleigh-Bénard convection is described in terms of several organizing phenomenological structures which are experimentally observed. Fig. 4.1 illustrates these different working structures that consist of boundary layers, plumes, jets, and coherent large-scale circulation. The convecting fluid has sharp thermal boundary layers at its top (cool) and bottom (hot) surfaces. Plumes grow erratically from these surfaces and spontaneously organize into a noisy but coherent wind. This large scale circulation, or turbulent wind, advects the plumes so that hot thermals rise along a laterally bounding wall while cold plumes sink along the opposite wall. The shear motion of large scale circulation in turn builds up viscous boundary layers around the walls. The interior of the cell away from the large scale circulation is typically assumed to be well-mixed, isotropic, and homogeneous. This picture is partially corroborated by measurements using containers with approximately equal height and width, and these working zones serve as the main physical ingredients in the GL theory.

The existence of large scale circulation, manifest experimental evidence, is one of the central assumptions in the GL theory. This large scale turbulent wind stirs the
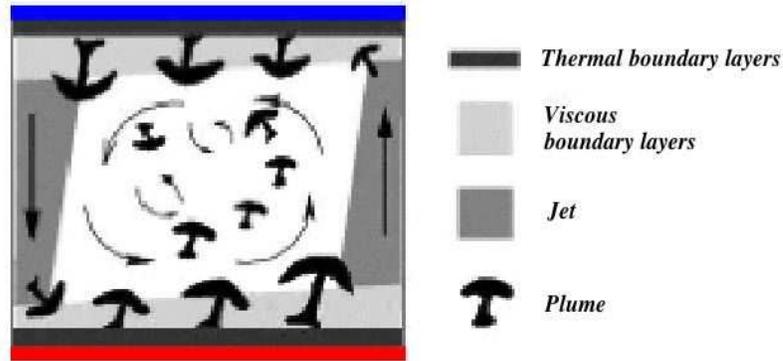
Figure 4.1: Different working structures in turbulent RBC: thermal and viscous boundary layers, plumes, jets, and coherent large-scale circulation. The illustration is adapted from Ref. [28].

bulk of the fluid and thus generates a velocity fluctuation. Therefore, in this case the Reynolds number Re is based on the velocity U of the large scale circulation, the depth of the cell L, and the kinetic viscosity of the fluid ν: $\mathrm{Re} = UL/\nu$. In addition, the large scale circulation applies shear to the fluid near the walls and induces viscous boundary layers of thickness λ_ν. By assuming that the sheared flow is laminar of Blasius type [71], λ_ν can be estimated by Re: $\lambda_\nu \sim L\mathrm{Re}^{-1/2}$. In addition to the viscous boundary layers, thermal boundary layers of thickness λ_T develop due to the hot bottom and cold top plates. The thermal boundary layer thickness λ_T is connected to the Nusselt number by assuming a thermal short circuit, i.e., no temperature drop in the bulk because of the turbulent convective transport: $\lambda_T = L/2\mathrm{Nu}$. These boundary layer thicknesses (λ_ν and λ_T) are in general different, and they essentially determine the Prandtl number $\mathrm{Pr} = \nu/\kappa$, with the thermal diffusivity κ and the kinematic viscosity ν. It is well known that a mathematically rigorous derivation of Nu or Re as a function of $(\mathrm{Ra}, \mathrm{Pr})$ is hardly possible. Nevertheless, the GL theory tries to be systematic and uses the dynamical equations for the velocity field $\mathbf{u}(\mathbf{x}, t)$, the kinematic pressure field $p(\mathbf{x}, t)$, and the temperature field $T(\mathbf{x}, t)$. The global averages of the kinetic and thermal dissipation rates in Rayleigh-Bénard convection,

denoted by ϵ_U and ϵ_T respectively, can be rigorously calculated using the Boussinesq approximation [25]:

$$\epsilon_U \equiv \langle \nu(\partial_i u_j(\mathbf{x}, t))^2 \rangle_v = \frac{\nu^3}{L^4}(\mathrm{Nu} - 1)\mathrm{Ra}\mathrm{Pr}^{-2}, \tag{4.1}$$

$$\epsilon_T \equiv \langle \kappa(\partial_i T(\mathbf{x}, t))^2 \rangle_v = \kappa\frac{\Delta T^2}{L^2}\mathrm{Nu}. \tag{4.2}$$

These dissipation processes take place both in the bulk of the flow and in the boundary layers, and thus can be decomposed into their contributions from the bulk and boundary layers:

$$\epsilon_U = \epsilon_{U,bulk} + \epsilon_{U,BL}, \tag{4.3}$$

$$\epsilon_T = \epsilon_{T,bulk} + \epsilon_{T,BL}. \tag{4.4}$$

The GL theory estimated the different partial dissipation rates using dimensional analysis, and balances ϵ_U (Eqn.4.1) and ϵ_T (Eqn.4.2) with their dominant parts from either the bulk or boundary layer contribution respectively, depending on the parameter regime of $(\mathrm{Ra}, \mathrm{Pr})$. As a result, the regime-dependent balances give rise to the $(\mathrm{Ra}, \mathrm{Pr})$-dependent local powers-laws of Nu and Re [32]. With the same approach and spirit, the GL theory has been also extended towards the very large Pr-regime, where much Rayleigh-Bénard convection data is available [33].

Table 2 in Ref. [32] and Table 1 in Ref. [33] summarize the different regime-dependent power-laws for Nu and Re predicted by GL. These references also thoroughly compare the GL predictions with various experimental data as of 2001. Here we add a comparison with newer experimental and numerical results, and highlight some remarks of the GL predictions. In particular, we focus on the Nu − Ra scaling. First, for small Pr and relatively small Ra in the turbulent regime, GL predicts Nu $\sim$ Ra$^\gamma$, with $\gamma = 1/4$, in agreement with various experimental results: $\gamma = 0.247$

by Rossby (1969) [72], $\gamma = 0.26 \pm 0.02$ by Cioni et al. (1997) [26], and $\gamma = 0.25$ by Ho-ranyi et al. (1999) [73]. Second, recent precise Nu-measurements spanning on a wide Ra-range are inconsistent with a pure single power law [29], as predicted by earlier models (see Ref. [25]). The data, however, are consistent with the cross-over power-law: $\mathrm{Nu} = \mathcal{A}\,\mathrm{Pr}^{-1/12}\mathrm{Ra}^{1/4} + \mathcal{B}\,\mathrm{Pr}^{-1/7}\mathrm{Ra}^{3/7}$ proposed by the GL theory for $Pr \gtrsim 2$ [29]. Third, there are several robust observations of $\mathrm{Nu} \sim \mathrm{Ra}^{2/7}$, spreading over about ten decades in Ra, by many experiments and simulations [27, 74, 75]. While, some other measurements show the breakdown of 2/7 scaling at higher Ra [26, 76, 77]. The GL theory suggests a linear combination of the 1/4 and the 1/3 Nu-power laws that effectively yields a 0.289 scaling exponent and mimics this $2/7 = 0.286$ power-law exponent. Forth, the GL theory accounts for the Pr dependence of Nu in several regimes. There are different theoretical predictions in the regime $\mathrm{Pr} \geq 1$ as to whether Nu is independent of Pr or a decreasing function of it [25, 26, 30]. Recent experiments conducted in four fluids using the same unity aspect-ratio cell show that Nu decreases $\sim 20\%$ over the Pr-range from 4 to 1350 for Ra from 2×10^7 to 3×10^{10} [78]. The data, alternatively, may be described by a power law in Pr with an exponent ~ -0.03, and agree well with the GL prediction. Similarly, another recent experiment that studied the Pr dependence of Nu over the range of Pr from 4 to 34 (for Ra from 3×10^7 to 10^{11}) supports the extended GL theory [79], in that Nu very slightly decreases with Pr for $\mathrm{Pr} \geq 1$ [33].

Good agreement between various experimental data and the GL predictions have been observed. The GL theory has many strengths, such as its systematic approach and generality without assuming the heat transport mechanism or the dimensionality of the system. Based on the assumptions, however, the GL theory has some limitations on its validity. For instance, for very large Ra, large scale circulation may be so vigorous as to drive the kinetic boundary layers to become turbulent rather than laminar as assumed. Moreover, the prefactors of Nu scaling in the GL prediction are not

an outcome of the theory, but rather a fitted result from experimental data. Thus, the values of these prefactors, the linear coefficients in Nu scaling, are not independently determined but influenced by the input data. As we will see in the next section, the GL theory has been extended for the electroconvection; the new results show that the prefactor in the charge transport scaling is affected by the aspect-ratio Γ of the convection cell. The GL theory only considers unity aspect-ratio cells. In addition, a very recent numerical study with a slender cylindrical cell of aspect-ratio 1/2 and Pr = 0.7 found that one large scale circulation breaks up into two counter-rotating asymmetric unity-aspect ratio rolls at large Ra > 10^{10} [80]. These recent studies imply that the parameter-dependent Nu scaling laws may span in three-dimensional parameter space of $(\mathrm{Ra}, \mathrm{Pr}, \Gamma)$.

The next Section shows how Γ affects the charge transport scaling for annular electroconvection in the turbulent regime.

4.3 Charge transport scaling in turbulent electro-convection

4.3.1 Background

The basic equations for annular electroconvection are previously discussed in Section 3.2. The close similarity of the convective instability mechanisms between electroconvection and thermal convection makes it possible to develop the scaling law theory based on the GL theory for Rayleigh-Bénard convection. This theoretical work was collaborated with Z. A. Daya.

The starting point of the scaling theory is the dynamical equations for the velocity field and surface charge. These equations, stated in Eqns. 3.3 and 3.4, are governed by the conservation of momentum and charge. Alternatively, the surface charge q can

be calculated with the Dirichlet Green function $G(r, \theta, z; r', \theta', z')$, in accordance with the Dirichlet boundary conditions of the electric potential. Then, Eqns. 3.5 and 3.6 for the surface charge density can be solved via the following equation:

$$
\begin{aligned}
q(r, \theta) &= \frac{\epsilon_0}{2\pi} \left[\oint da' \; \psi(r', \theta', z' = 0) \frac{\partial^2 G}{\partial z \partial z'} \bigg|_{z'=0} \right]_{z=0^+}, \\
&\equiv g[\Psi], \quad \Psi = \psi_2 = \psi(r, \theta, z = 0).
\end{aligned}
\tag{4.5}
$$

To make the following expressions simpler, the 2D electric potential ψ_2 is denoted by Ψ.

Using the above relation of g, and denoting the kinematic pressure field by $p = P/\tilde{\rho}$ and kinematic viscosity by $\tilde{\nu} = \tilde{\eta}/\tilde{\rho}$, the dynamical Eqns. 3.3-3.4 reduce to the following pair:

$$
\partial_t \mathbf{u} + \mathbf{u} \cdot \nabla \mathbf{u} = -\nabla p + \tilde{\nu} \nabla^2 \mathbf{u} - \frac{g[\Psi]}{\tilde{\rho}} \nabla \Psi,
\tag{4.6}
$$

$$
\partial_t \Psi + \mathbf{u} \cdot \nabla \Psi = \frac{\tilde{\sigma} \nabla^2 \Psi}{\partial_\Psi g}.
\tag{4.7}
$$

Written in this way, the Eqns. 4.6 and 4.7 bear striking similarity to the Boussinesq equations for turbulent Rayleigh-Bénard convection [32] with the scalar temperature T and electric potential fields Ψ assuming similar roles:

$$
\partial_t \mathbf{u} + \mathbf{u} \cdot \nabla \mathbf{u} = -\frac{\nabla p}{\rho_0} + \nu \nabla^2 \mathbf{u} + \beta \, \hat{\mathbf{g}} T,
\tag{4.8}
$$

$$
\partial_t T + \mathbf{u} \cdot \nabla T = \kappa \nabla^2 T.
\tag{4.9}
$$

Here ρ_0 is the fluid mass density, ν is the kinematic viscosity, β is the isobaric thermal expansion coefficient, $\hat{\mathbf{g}}$ is the gravitational acceleration, and κ is the thermal diffusivity.

However, the complicated nonlocal functional relationship $g[\Psi]$ between q and

Ψ given in Eqn. 4.5 makes it difficult to carry out the analogous GL argument for electroconvection. Fortunately, by splitting the integrand in Eqn. 4.5 into local and nonlocal parts, g can be expanded as

$$g[\Psi] = \frac{\epsilon_0}{r_o - r_i}\Psi + \text{nonlocal terms}. \qquad (4.10)$$

To a first order approximation, the functional $g[\Psi]$ can be approximated as a linear function $g(\Psi)$, so that the surface charge density and the electric potential on the film are related *locally*. Then $\partial_\Psi g$ is constant and Eqn. 4.7 is identical to the heat equation in Rayleigh-Bénard convection, with electric potential in place of temperature. Nonetheless, in Eqn. 4.6 the approximated driving body force $\sim \Psi\nabla\Psi$ does not identically correspond to the buoyancy force $\sim \nabla T$ when replacing Ψ by T in the Rayleigh-Bénard convection equations.

The critical parameters and the critical mode numbers at the onset of electroconvection have been successfully captured using the exact base state and the aforementioned local approximation for the perturbations, as is described in detail in Ref. [38]. The critical $\mathcal{R}$ in electroconvection has been found both theoretically and experimentally to be $\lesssim 100$, smaller than the corresponding $\text{Ra}_c = 1708$ in RBC. The reasons for the difference are, first, the two convection systems have different base states [38] and, secondly, their driving body forces do not identically correspond to each other, even under the local approximation. However, one would expect the same critical Rayleigh number in the case of identical driving forces and similar geometry. Indeed, a study of 2D annular Rayleigh-Bénard convection [81] showed a critical Rayleigh number ~ 2000.

In the following calculations, the relation $g \propto \Psi$ is assumed at much higher forcing to develop the GL theory for turbulent electroconvection within the local approximation, which makes Eqns. 4.6 and 4.7 very similar to the Boussinesq equations for

thermal convection.

4.3.2   Global averages

In this section, exact expressions for various globally averaged quantities are derived. These quantities, according to the GL procedure, will be balanced against scaling estimates, as discussed below.

As in the GL theory for Rayleigh-Bénard convection, the kinetic and electric dissipation rates, denoted by $\epsilon_\mathbf{u}$ and ϵ_ψ respectively, are calculated:

$$\epsilon_\mathbf{u}(r, \theta, t) \quad = \quad \tilde{\nu}(\nabla \mathbf{u})^2, \tag{4.11}$$

$$\epsilon_\psi(r, \theta, t) \quad = \quad \tilde{\sigma}(\nabla \Psi)^2. \tag{4.12}$$

The averages of the above dissipations over the fluid volume v are denoted as

$$\epsilon_\mathbf{u} \quad = \quad \langle \epsilon_\mathbf{u}(r, \theta, t) \rangle_v = \langle \tilde{\nu}(\nabla \mathbf{u})^2 \rangle_v \tag{4.13}$$

$$\epsilon_\psi \quad = \quad \langle \epsilon_\Psi(r, \theta, t) \rangle_v = \langle \tilde{\sigma}(\nabla \Psi)^2 \rangle_v. \tag{4.14}$$

Here, the angular brackets $\langle \cdots \rangle_v$ denote averages over the fluid volume v (actually its annular area), as the expressions below:

$$\langle \cdots \rangle_v = \frac{\int \ \cdots \ r dr d\theta}{\int \ r dr d\theta} = \frac{\int_0^{2\pi} \int_{r_i}^{r_o} \ \cdots \ r dr d\theta}{\pi(r_o^2 - r_i^2)} \ . \tag{4.15}$$

The velocity and electric potential fields share the azimuthal periodicity of the annulus and thus permit the calculation of the globally-averaged kinetic and electric dissipation rates in Eqns. 4.13 and 4.14. Assuming time-stationarity for the spatial averaging and the local approximation $g \propto \Psi$, multiplying Eqn. 4.6 by $\mathbf{u}$ and Eqn. 4.7 by Ψ, the following rigorous relations of globally averaged dissipation rates

are calculated:

$$\epsilon_{\mathbf{u}} = \frac{\tilde{\nu}^3 \mathcal{R} \mathcal{P}^{-2}(Nu - 1)}{\ln(1/\alpha)(r_o^2 - r_i^2)(r_o - r_i)^2}, \tag{4.16}$$

$$\epsilon_\psi = \frac{2\tilde{\sigma}V^2 \ Nu}{\ln(1/\alpha)(r_o^2 - r_i^2)}, \tag{4.17}$$

where the Nusselt number Nu, defined in Eqn. 3.65, can be written in the following explicit form:

$$Nu = \frac{\int_0^{2\pi} (u_r q - \tilde{\sigma}\partial_r \Psi) \ r d\theta}{2\pi\tilde{\sigma}V/\ln(1/\alpha)} . \tag{4.18}$$

The above relations have interesting similarities and differences to those for the corresponding quantities in Rayleigh-Bénard convection, listed in Eqns. 4.1 and 4.2: The differences between Eqns 4.16-4.17 and Eqns 4.1-4.2 are entirely due to the annular geometry of the electroconvection system. In the narrow gap limit, in which the radius ratio $\alpha \to 1$ while the film width $d = r_o - r_i$ remains constant, Eqns. 4.16 and 4.17 recover the familiar forms for Rayleigh-Bénard convection between parallel plates.

4.3.3   Grossmann-Lohse scalings

In this section, several assumptions about the spatial organization of the turbulent flow are made, in the same manner as in the scaling theory of Grossmann and Lohse (GL), as they explain in Section 2 of Ref. [32]. In particular, GL assumed that a turbulent wind, or a large scale circulation, comprising a single cell occupies the entire $\Gamma \sim 1$ Rayleigh-Bénard convection container. The wind is driven by plumes from the boundary layers and it in turn drives the interior or bulk. With the boundary layers and bulk conceptually distinguished, GL estimate the relative boundary and bulk dissipations. Here, the analogous assumptions are made for turbulent electro-convection. As shown in Fig. 2.6b, the turbulent flow consists of counter-rotating

convection vortices around the annulus. The vortices, which are unsteady, have fluctuating boundaries that are defined by the averaged turbulent large scale circulation. Each vortex is assumed to be roughly square with the film width $d = r_o - r_i$. Near the electrodes, well developed viscous and electric boundary layers with respective thicknesses $\lambda_{\mathbf{u}}$ and λ_ψ are assumed. Away from the electrodes, the vortex interior, or bulk, is taken to be well mixed. We do not account for the slight differences between the boundary layer dimensions at the inner and outer electrodes due to the annular geometry. This asymmetry diminishes with increasing aspect ratio and is assumed to be always small.

The total dissipations calculated in Eqns. 4.16 and 4.17 are decomposed into contributions from the boundary layer (BL) and bulk regions of the convection cells as in Eqns.4.16 and 4.17:

$$
\begin{aligned}
\epsilon_{\mathbf{u}} &= \epsilon_{\mathbf{u}}^{BL} + \epsilon_{\mathbf{u}}^{bulk}, \\
\epsilon_\psi &= \epsilon_\psi^{BL} + \epsilon_\psi^{bulk}.
\end{aligned}
\tag{4.19}
$$

The contribution $\epsilon_{\mathbf{u}}^{BL}$ of the boundary layer kinetic dissipation is defined as

$$
\begin{aligned}
\epsilon_{\mathbf{u}}^{BL} &= \langle \epsilon_{\mathbf{u}}(\mathbf{r} \in BL, t) \rangle_v = \langle \tilde{\nu}(\nabla \mathbf{u}(\mathbf{r} \in BL, t))^2 \rangle_v, \\
&= \frac{\int_0^{2\pi} \int_{r_i}^{r_i+\lambda_{\mathbf{u}}} \tilde{\nu}(\nabla \mathbf{u})^2 \ rdrd\theta}{\int_0^{2\pi} \int_{r_i}^{r_o} \ rdrd\theta} + \frac{\int_0^{2\pi} \int_{r_o-\lambda_{\mathbf{u}}}^{r_o} \tilde{\nu}(\nabla \mathbf{u})^2 \ rdrd\theta}{\int_0^{2\pi} \int_{r_i}^{r_o} \ rdrd\theta}.
\end{aligned}
\tag{4.20}
$$

The electric dissipation from the bulk contribution ϵ_ψ^{bulk} is defined as

$$
\begin{aligned}
\epsilon_\psi^{bulk} &= \langle \epsilon_\psi(\mathbf{r} \in bulk, t) \rangle_v = \langle \tilde{\sigma}(\nabla \Psi(\mathbf{r} \in bulk, t))^2 \rangle_v, \\
&= \frac{\int_0^{2\pi} \int_{r_i+\lambda_\psi}^{r_o-\lambda_\psi} \tilde{\sigma}(\nabla \Psi)^2 \ rdrd\theta}{\int_0^{2\pi} \int_{r_i}^{r_o} \ rdrd\theta}.
\end{aligned}
\tag{4.21}
$$

The other two boundary and bulk dissipations are similarly defined. Assume that

$$Nu = \mathrm{F}(\Gamma)\mathrm{f}(\mathcal{R},\mathcal{P}); \qquad (4.22)$$

the key purpose here is to determine the as yet unspecified functions F and f. This calculation starts with the estimations for the bulk and boundary layer dissipations. As in GL theory [32], in what follows numerical factors of $O(1)$ are ignored.

Kinetic dissipations

The turbulent wind or the large scale circulation sets the velocity scale U for both the boundary and bulk regions. A viscous or kinetic boundary layer, assumed to be laminar, scales as $\lambda_{\mathbf{u}} \sim (r_o - r_i)\mathrm{Re}^{-1/2}$. Here Re is the Reynolds number based on the large scale circulation velocity U and film width $r_o - r_i$: $\mathrm{Re} \equiv U(r_o - r_i)/\tilde{\nu}$. $\lambda_{\mathbf{u}} \ll r_i$, $\lambda_{\mathbf{u}} \ll r_o$ and $\lambda_{\mathbf{u}} \ll r_o - r_i$, were assumed; this greatly simplifies the averaging in Eqns. 4.20 and 4.21. For the boundary layer, the kinetic dissipation was estimated by

$$
\begin{aligned}
\epsilon_{\mathbf{u}}^{BL} &= \langle \tilde{\nu} \left(\nabla \mathbf{u}(\mathbf{r} \in BL, t) \right)^2 \rangle_v \\
&\sim \tilde{\nu} \left(\frac{U}{\lambda_{\mathbf{u}}} \right)^2 \frac{\lambda_{\mathbf{u}}}{r_o - r_i} \sim \frac{\tilde{\nu}^3}{(r_o - r_i)^4} \mathrm{Re}^{5/2} ,
\end{aligned} \qquad (4.23)
$$

where U/λ_u characterizes the order of magnitude of $|\nabla \mathbf{u}|$ in the boundary layers, and the factor $\lambda_u/(r_o - r_i)$ accounts for the boundary layer regime to the total volume.

The bulk (areal) kinetic dissipation rate is estimated with the main assumption of the GL theory, i.e., that the large scale circulation stirs the interior. In 3D Rayleigh-Bénard convection, GL theory estimates the bulk kinetic dissipation rate with the convective term of the large scale circulation. The kinetic energy which is injected at the largest scale, that of the large scale circulation, is assumed to be dissipated

at small scales via the forward turbulent energy cascade in the bulk [32]. However, forced and freely decaying 2D turbulence differs markedly from 3D turbulence [62, 82]. The absence of the vortex stretching term in 2D leads to vorticity conservation along fluid particle paths in an unforced, inviscid system. Notwithstanding this difference, numerical simulations of 2D Rayleigh-Bénard turbulence [75, 83] show remarkably similar phenomenology and heat-transport scalings to those of 3D turbulent Rayleigh-Bénard convection systems. Hence, the key assumption of the GL theory, that the large scale circulation drives the bulk, is valid for both 2D and 3D systems [75]. Thus, we assume that we may directly use the convective term of the large scale circulation to estimate the dissipation rate. This leads to the following expression;

$$
\begin{aligned}
\epsilon_{\mathbf{u}}^{bulk} &= \langle \tilde{\nu}(\nabla\mathbf{u}(\mathbf{r} \in bulk, t))^2 \rangle_v \sim \mathbf{u} \cdot (\mathbf{u} \cdot \nabla)\mathbf{u} \\
&\sim \frac{U^3}{r_o - r_i} \sim \frac{\tilde{\nu}^3}{(r_o - r_i)^4}\mathrm{Re}^3 \, .
\end{aligned}
\tag{4.24}
$$

The relations 4.23 and 4.24 are identical to their counterparts for turbulent Rayleigh-Bénard convection, given in Section 2.3 of Ref. [32].

Electric dissipations

The applied potential V drops over the electric potential boundary length λ_ψ, which we assume is small such that $\lambda_\psi \ll r_i$, $\lambda_\psi \ll r_o$ and $\lambda_\psi \ll r_o - r_i$. As with the kinetic dissipations, these requirements greatly simplify the averaging prescribed by Eqns. 4.20 and 4.21. Since most of the applied potential drops over λ_ψ at the inner and outer electrodes, there is effectively an electrical short *i.e.* a constant potential, in the bulk. Invoking the standard arguments of turbulent Rayleigh-Bénard convection, where the thermal short determines a relation between the thermal boundary layer

and the heat transport, we find that

$$\lambda_\psi \sim \frac{(r_i + r_o)\ln(1/\alpha)}{Nu} \, .$$

(4.25)

Here, it is assumed that half the applied potential drops over the potential boundary layer at the inner electrode and half at the outer electrode. The electric potential boundary layer thicknesses are assumed to be the same at the inner and outer electrodes. This symmetry is exact for radius ratio $\alpha \to 1$ or aspect ratio $\Gamma \to \infty$. The derivation implicitly assumes that the role of the asymmetry is not crucial at smaller Γ.

In the boundary layer, the electric dissipation is given by

$$\epsilon_\psi^{BL} = \langle \tilde{\sigma}(\nabla \Psi \in BL)^2 \rangle_v \sim \tilde{\sigma}\left(\frac{V}{\lambda_\psi}\right)^2 \frac{\lambda_\psi}{r_o - r_i} \, .$$

(4.26)

By balancing the latter two terms in Eqn. 4.7

$$\mathbf{u} \cdot \nabla \Psi \approx \frac{\tilde{\sigma}\nabla^2 \Psi}{\partial_\Psi g} \, ,$$

(4.27)

The corresponding expression, up to a linear expansion of $g(\Psi)$, follows

$$\frac{V}{\lambda_\psi} \sim \frac{\tilde{\sigma}(r_o - r_i)V}{\epsilon_0 U \lambda_\psi^2} \, .$$

(4.28)

Using U as the velocity scale, we have implicitly assumed that $\lambda_\psi \le \lambda_\mathbf{u}$. Substituting in Eqn. 4.26 for V/λ_ψ from Eqn. 4.28 and for λ_ψ from Eqn. 4.25 we get

$$\epsilon_\psi^{BL} \sim \left(\frac{1+\alpha}{1-\alpha}\right)\frac{\ln(1/\alpha)\,\mathrm{Re}\,\mathcal{P}\tilde{\sigma}V^2}{Nu\,(r_o - r_i)^2} \, .$$

(4.29)

The dissipations estimated in Eqns. 4.23, 4.24 and 4.29 are sufficient to define the

two relevant regimes for turbulent electroconvection. In one scenario, we assume that both the electrical and kinetic dissipations occur primarily in the boundary. Then Eqn. 4.19 will be written as

$$\epsilon_{\mathbf{u}} \approx \epsilon_{\mathbf{u}}^{BL}, \quad \epsilon_{\psi} \approx \epsilon_{\psi}^{BL}. \tag{4.30}$$

This corresponds to the I$_l$ regime of Ref. [33]. For the left-hand-sides in the above equations, we use the globally averaged dissipations derived from the equations of motion given in Eqns. 4.16 and 4.17. For the right-hand-sides we use the boundary layer estimates given in Eqns 4.23 and 4.24. After some algebraic manipulation, the result yields

$$Nu \propto F(\Gamma)\mathcal{R}^{1/4}\mathcal{P}^{1/8} \quad \text{(regime I$_l$ of Ref. [32]).} \tag{4.31}$$

Repeating the above procedure for

$$\epsilon_{\mathbf{u}} \approx \epsilon_{\mathbf{u}}^{bulk}, \quad \epsilon_{\psi} \approx \epsilon_{\psi}^{BL}, \tag{4.32}$$

which corresponds to regime II$_l$ of Ref. [33], it is found that

$$Nu \propto F(\Gamma)\mathcal{R}^{1/5}\mathcal{P}^{1/5} \quad \text{(regime II$_l$ of Ref. [32]).} \tag{4.33}$$

In general, this procedure gives a power law dependence for f in Eqn. 4.22 of the form

$$f \sim \mathcal{R}^{\gamma}\mathcal{P}^{\delta}. \tag{4.34}$$

It also follows that the Reynolds number Re of the vortices, based on the radial velocity of the fluid and the separation between the electrodes $r_o - r_i$, scales as

$$Re \sim \mathcal{R}^{\gamma_*}\mathcal{P}^{\delta_*}. \tag{4.35}$$

The same set of exponents $\gamma, \delta, \gamma_*, \delta_*$ is found as the GL theory for turbulent Rayleigh-Bénard convection. The I_l and II_l regimes are relevant to the relatively low $\mathcal{R}$ in the turbulent regime and broad $\mathcal{P}$ range that can be accessed by smectic electroconvection.

4.3.4 Aspect ratio dependence

After balancing the dominant contributions, as in Eqns. 4.30 and 4.32, the power law $\mathcal{R}^\gamma \mathcal{P}^\delta$ has a common algebraic prefactor F that is only a function of the aspect ratio Γ. The aspect ratio Γ in annular electroconvection can be defined by the ratio of the circumference of the film measured at the inner electrode to the film width;

$$\Gamma = \frac{2\pi r_i}{r_o - r_i} = \frac{2\pi\alpha}{1 - \alpha}. \tag{4.36}$$

Stated in this way, this aspect ratio spans the same Γ-range of $0 \leq \Gamma \leq \infty$ as Rayleigh-Bénard cells so as to make a direct comparison with Rayleigh-Bénard results.

Unlike in previous studies of Rayleigh-Bénard convection in Cartesian geometry [25, 31], $F(\Gamma)$ is not itself a power law. Instead, it is given by

$$F(\Gamma) = \frac{\Gamma + \pi}{\pi} \ln\left(\frac{\Gamma + 2\pi}{\Gamma}\right). \tag{4.37}$$

$F(\Gamma)$ specifies the aspect ratio dependence of the global charge or heat transport, as contained in the Nusselt number Nu. The Reynolds number Re of the large scale circulation, however, is local to each vortex and is independent of Γ.

In the next chapter, this theoretical prediction $F(\Gamma)$ is discussed and compared with experimental and numerical data in the high Rayleigh number regime in Section 5.3.

Chapter 5

Results and discussion

In this chapter, experimental data, numerical results, and theoretical predictions, to-gether with their comparisons, are presented and discussed; the sections are organized according to the states of electroconvection as the strength of the electrical forcing is increased from weak to strong. Section 5.1 focuses on the laminar steady convection, including the impacts of the radius ratio α and the Prandtl number $\mathcal{P}$ and the flow dynamics near a codimensional-two point at which two probable azimuthal modes are equally unstable. In Section 5.2, numerical investigations are extensively discussed for sheared convection, simultaneously subjected to a radial forcing and an azimuthal shear. The last but not the least, Section 5.3 is devoted to the results of turbulent electroconvection under strong forcing as well as the influences of α and $\mathcal{P}$ on the Nu scaling.

5.1 Convection in the weakly nonlinear regime

As the applied electrical forcing $\mathcal{R}$ is gradually increased beyond a threshold $\mathcal{R}_c$, the film undergoes the first transition from a quiescent conductive state to a laminar con-vective state. This primary bifurcation is associated with symmetry breaking, and is

well modeled by the steady Landau amplitude equation in Eqn. 3.71 when the forcing is not far above the onset. Similarly, a Landau phenomenological description based on a symmetry argument is commonly used for the order parameter at a phase transition for systems in thermodynamic equilibrium. A *supercritical* or *forward* bifurcation means that the amplitude of the emerging pattern grows continuously from zero with no hysteresis as the control parameter is increased. This is analogous to a second order phase transition in thermodynamic equilibrium. On the other hand, a *subcritical* or *backward* bifurcation indicates that the amplitude jumps discontinuously and exhibits hysteresis, similar to a first order phase transition in thermal equilibrium, as the control parameter is changed.

This section is devoted to the numerical results with no applied shear at the primary bifurcation which is quantitatively described by the cubic nonlinearity coefficient g in the Landau amplitude equation, Eqn. 3.71. In particular, the effects of geometry and Prandtl number on g are the main emphases when the reduced control parameter $\epsilon = \mathcal{R}/\mathcal{R}_c - 1$ ranges from -0.5 to 1.0. Furthermore, the simulation results are compared with perviously published experimental data and theoretical calculations.

Below the critical forcing $\mathcal{R}_c$, the film remains still because the forcing is not vigorous enough to overcome the electric and viscous dissipation. Fig. 5.1 shows the base states of the 2D electric potential ψ_2 and the charge configuration q for a film with $\alpha = 0.33$, $\mathcal{P} = 10$, which is quiescent. These base states are obtained by solving a Laplace equation for the electric potential in the polar coordinates and a Maxwell equation for charge density, Eqns. 3.5-3.7. Fig. 5.1b, which shows the base state of q, clearly reveals the inverted charge configuration that is unstable to the applied voltage; positive charges accumulate near the inner electrode which has electrically high potential whereas negative charges accumulate close to the outer grounded electrode. Clearly, a purely conductive film preserves symmetries under
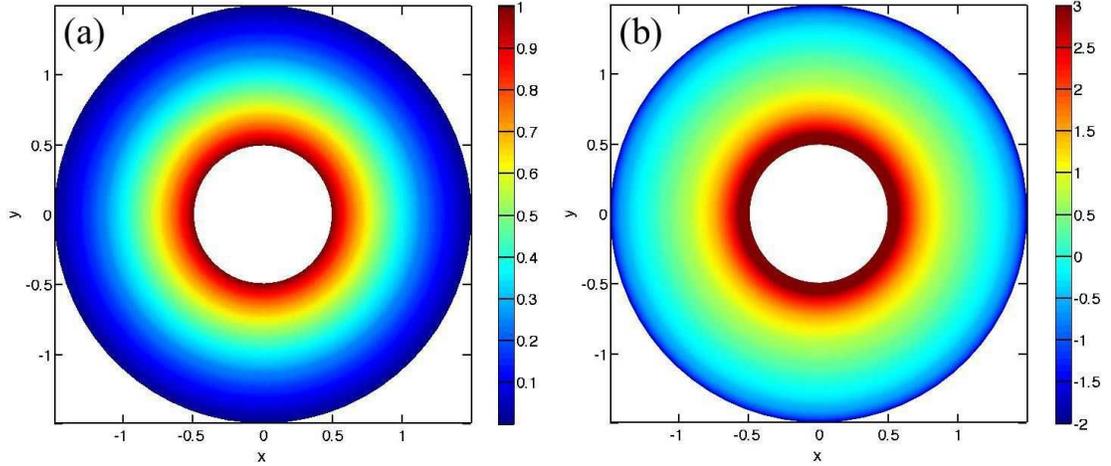
Figure 5.1: The base states of 2D electric potential ψ_2 in (a) and the charge distribution q in (b), due to pure conduction for $\alpha = 0.33, \mathcal{R} = 75.7, \mathcal{P} = 10$, when forcing is not too strong to overcome viscous dissipation and thus the film stays still.

reflection and any azimuthal rotation.

At $\mathcal{R}_c$, a symmetry-breaking process sets in by a cellular flow motion. Fig. 5.2 shows the simulation results of basic fields for the same α and $\mathcal{P}$ as in Fig. 5.1, but at $\epsilon = 1.48$ in the steady convection regime. The total electric potential ψ_2 in Fig. 5.2a now preserves some symmetries under discrete rotations by an angle of $\pi/2$, at $\alpha = 0.33$. The total charge q in Fig. 5.2b, compared with its base state in Fig. 5.1b, includes additional charge carried by counter-rotating swirls. Fig. 5.2c shows the perturbed electric potential $\psi_2^{(1)}$, resulting from the steady convection, and corresponds to Fig. 5.2a with the base state $\psi_2^{(0)}$ subtracted off. The corresponding flow fields are shown in Fig. 5.2d: the streamfunction contours ϕ (colour) and velocity field (black).

5.1.1   Dependence on geometry

The radius ratio α strongly influences the critical Rayleigh number $\mathcal{R}_c$, the critical mode number m_c and, to a lesser extent, the nonlinear cubic coefficient g.
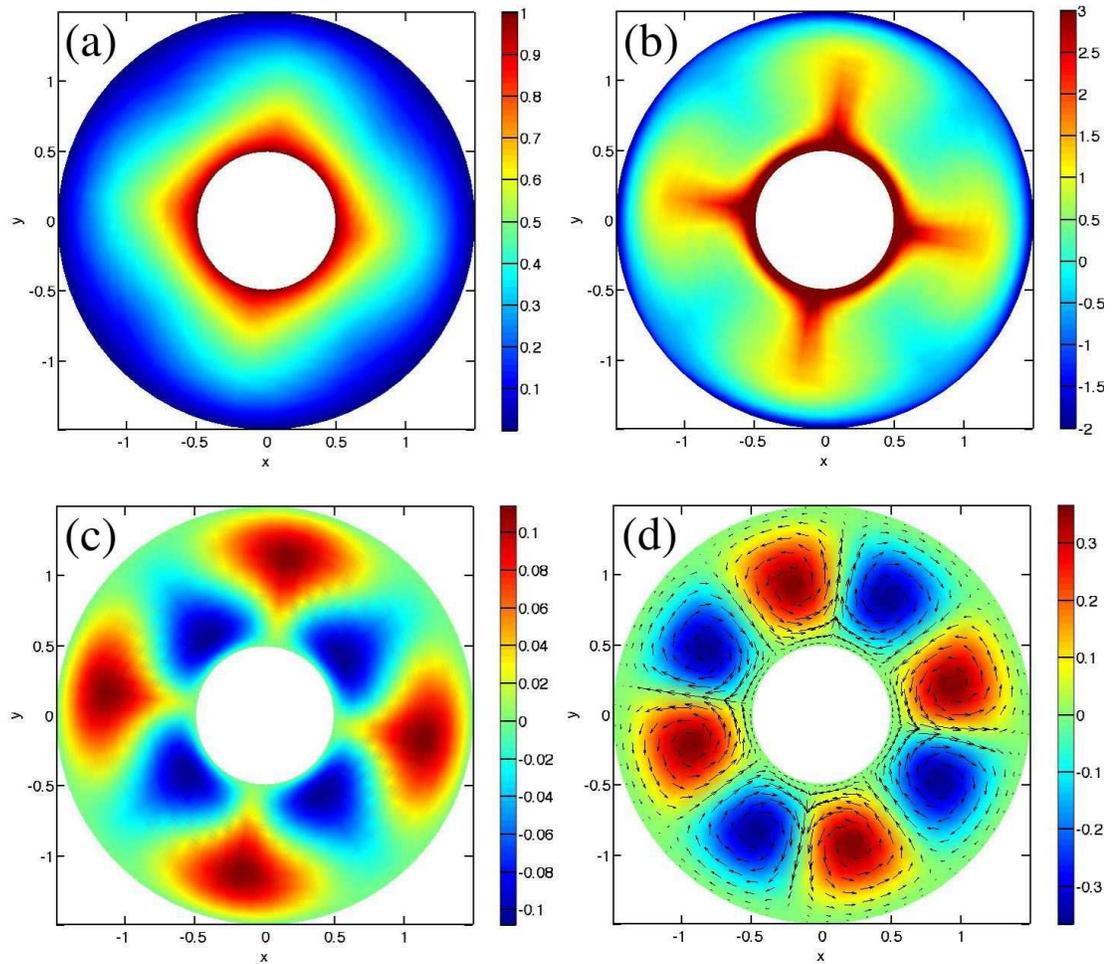
Figure 5.2: Numerical results of basic electric and flow fields under steady convection at $\alpha = 0.33, \mathcal{R} = 186.8, \mathcal{P} = 10$: 2D electric potential ψ_2 in (a), the charge distribution q in (b), the perturbed electric potential $\psi_2^{(1)}$ due to the laminar flow in (c), and the corresponding streamfunction ϕ (colour) and velocity field (black) in (d).

Numerical simulations reveal that the primary bifurcation is continuous or super-critical for $\mathcal{P} = 10$ over a broad range of α, as shown in Fig. 5.3. Values of g are found between 2.0 and 2.6. These values are in excellent agreement with calculations of g for $0.60 \leq \alpha \leq 0.80$ from a local, weakly nonlinear theory [55]. Both numerical and theoretical data therefore suggest only a weak dependence of g on α.

These results can be compared to experimental measurements in which g was extracted by fitting current-voltage data [54]. Even though the experimental results show a considerable scatter, as can be seen in Fig. 5.3, they generally show supercritical bifurcations for various $\mathcal{P} > 1$. For the larger α, these agree with simulation and weakly nonlinear theory.

For small α, and particularly for the smallest $\alpha = 0.33$, a systematic disagreement is observed. At $\alpha = 0.33$, the experimentally measured g actually becomes negative, indicating a subcritical bifurcation which is in clear disagreement with the simulation and weakly nonlinear theory. The most likely explanation for this disagreement is that the geometry of the electrodes in the experimental cell deviates more from the idealizations of the model as α becomes smaller. The support structure for the centre electrode may become significant. The field term f in the fitting function Eqn. 3.71, which describes the imperfection of the bifurcation, was experimentally found increasing for small α. Also, the result for g at $\alpha = 0.33$ was obtained by averaging over data taken over a range in $\mathcal{P}$, which may have introduced some bias since the experimental values of $\mathcal{P}$ tend to be closer to one, and therefore fractionally more uncertain, for small α. More experiments will be required to sort out this discrepancy.

5.1.2   Dependence on the Prandtl number $\mathcal{P}$

The Prandtl number $\mathcal{P}$ measures the dimensionless ratio of the charge and viscous relaxation times. Large $\mathcal{P}$ limits the influence of the nonlinear advection and time derivative terms compared to the viscous and external driving force terms. Linear
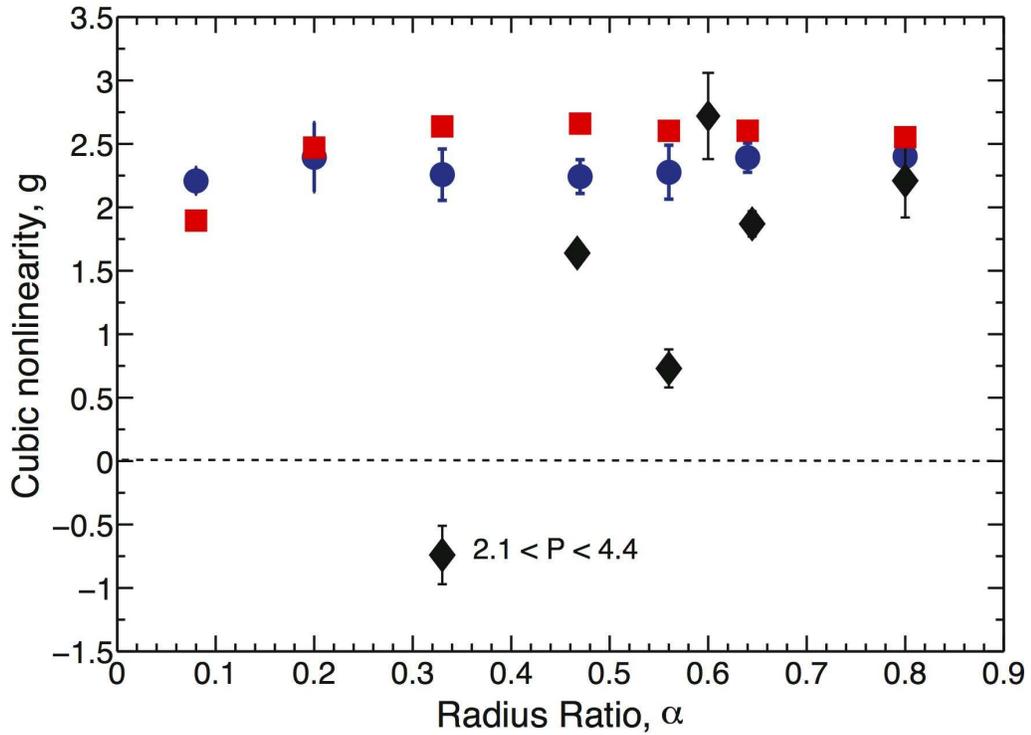
Figure 5.3: The radius ratio dependence of the coefficient of the cubic nonlinearity, g. Numerical data ($\bullet$) for $\mathcal{P} = 10$ with various radius ratios α show a continuous and supercritical bifurcation ($g > 0$) [84]. They agree well with a nonlocal theory prediction, calculated by V. B. Deyirmenjian, for $\mathcal{P} = 123$ shown by red filled squares ($\square$). Black filled diamonds ($\diamondsuit$) are experimental results, from Ref. [54], for various $\mathcal{P} > 1$.
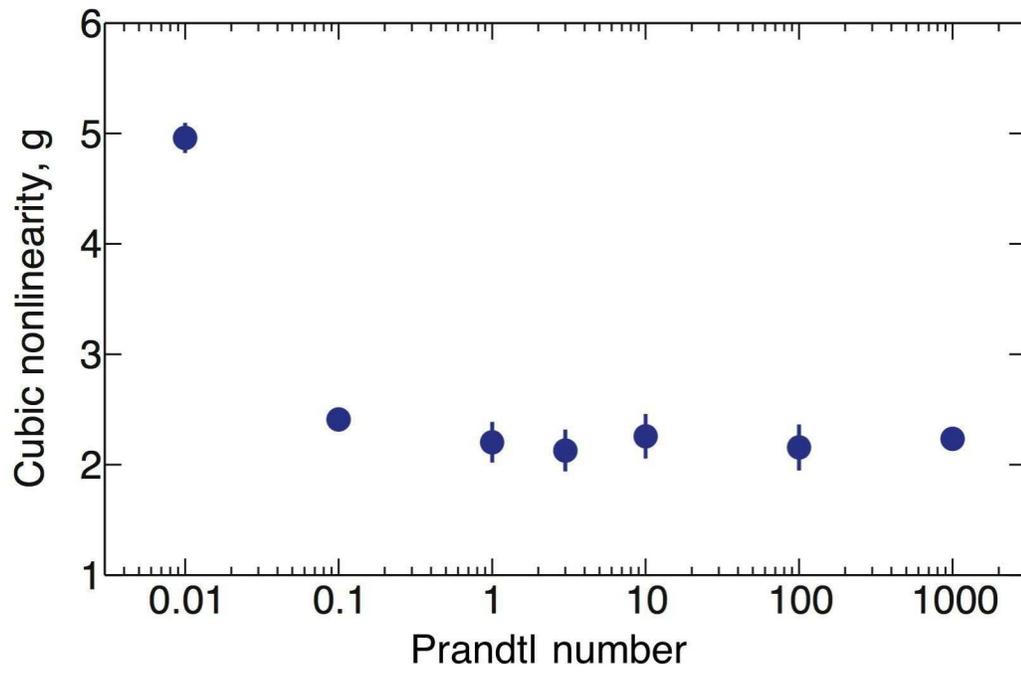
Figure 5.4: Simulation data of the cubic nonlinearity coefficient g over a wide range of $\mathcal{P}$ for a fixed $\alpha = 0.33$. The numerical data show supercritical bifurcations $g > 0$ for various $\mathcal{P}$ and the $\mathcal{P}$-independence of g for $\mathcal{P} > 0.1$.

stability analysis predicts that $\mathcal{R}_c$ should be independent of $\mathcal{P}$ for all α. This result follows from the fact that the base state is quiescent. In particular, linear theory predicts $\mathcal{R}_c \approx 82$ at $\alpha = 0.33$. In agreement with this, the simulation data at $\alpha = 0.33$ consistently shows values of $\mathcal{R}_c$ spread between 80 and 82 for a wide range of $\mathcal{P}$ between 0.01 and 1000.

The Prandtl number $\mathcal{P}$ has an effect on the nonlinear behavior, and in particular on the coefficient of the cubic nonlinearity g for small $\mathcal{P}$. Fig. 5.4 shows g for a range of $\mathcal{P}$ between 0.01 and 1000. This is a much wider range than that achievable experimentally. The smallest value achieved in experiments was $\mathcal{P} \sim 2$. The simulation data for $\alpha = 0.33$ show very little dependence on $\mathcal{P}$ for $0.1 \leq \mathcal{P} \leq 1000$. However, for small $\mathcal{P} < 0.01$, g increases by a factor of $\gtrsim 2$. This is a dramatic change compared to the near independence of g on $\mathcal{P}$ for $0.1 \leq \mathcal{P} \leq 1000$. The simulation data agree with previous theoretical calculations [55]. Experimental results also show the $\mathcal{P}$-independence of g for large $\mathcal{P}$. For example, $g \approx 2$ for $25 < \mathcal{P} < 65$ and $\alpha = 0.64$ [54]. Thus, in general $\mathcal{P}$ is a weak parameter in unsheared convection except for small $\mathcal{P} < 0.1$.

5.1.3   Codimension-two points

Numerous codimension-two (CoD2) points exist in the parameter space of the Rayleigh number $\mathcal{R}$ and the radius ratio α. At such CoD2 points, two adjacent azimuthal modes, m and $m + 1$, become simultaneously unstable at onset. This allows for unusual mode interactions near such points, which may lead to complex dynamics close to onset. The location of CoD2 points can be predicted by linear stability analysis. They appear in Fig. 3.4a at the intersection points of the scallop-shaped curves which map the onset values of $\mathcal{R}$ for each m_c. The dynamics of mode competition close to these CoD2 point has not previously been studied experimentally, or by weakly nonlinear analysis. The present numerical simulation gives us the tools to investigate

the dynamics near onset, close to a CoD2 point [84].

Langford and Rusu previously studied patterns in annular electroconvection using equivalent bifurcation theory [85]. They enumerated the possible bifurcations near CoD2 points. Under the assumption of a supercritical primary bifurcation, they predicted only two possible scenarios for the low lying secondary bifurcations. In one case, there is a smooth transition from the m to the $m + 1$ mode via a stable mixed-mode branch of Z_2 symmetry. This preserves reflection symmetry of the annulus while breaking the azimuthal rotational symmetry. In the other scenario, there is a hysteretic jump between the stable branches for modes m and $m + 1$.

$\alpha = 0.452$, predicted by linear theory [38] to be close to the CoD2 point for $m = 5$ and $m = 6$, was under investigation. Close to this α, for $\mathcal{R}$ slightly larger than $\mathcal{R}_c$, the numerical simulation shows that the amplitudes of the $m = 5$ and $m = 6$ Fourier modes both show positive growth for a long period of time, up to $\approx 150\tau_c$. However, the competition between the two modes is such that one mode eventually decays while the other saturates to a steady state after a long time. Fig. 5.5 shows the complete evolution. Fig. 5.6 shows the end result of the mode competition at $\alpha = 0.452$, for two slightly different values of $\mathcal{R}$ and different random white noise initial conditions. The final state is very sensitive to the initial condition, and it is found to latch into either $m = 5$ or $m = 6$.

The numerical simulation thus shows that, at least for this case, the secondary bifurcation is of the hysteretic type, corresponding to Fig. 3a in Ref. [85]. It is nevertheless possible to observe a mixed-mode. Fig. 5.5a shows the streamfunction of the co-existing $m = 5$ and $m = 6$ state, which does have the expected Z_2 symmetry. However, this mixed-mode state is transient, unstable, and eventually relaxes to a single-mode state. At present, CoD2 points showing stable mixed modes were not observed, although not all values of α, $\mathcal{R}$ and $\mathcal{P}$ have been explored.
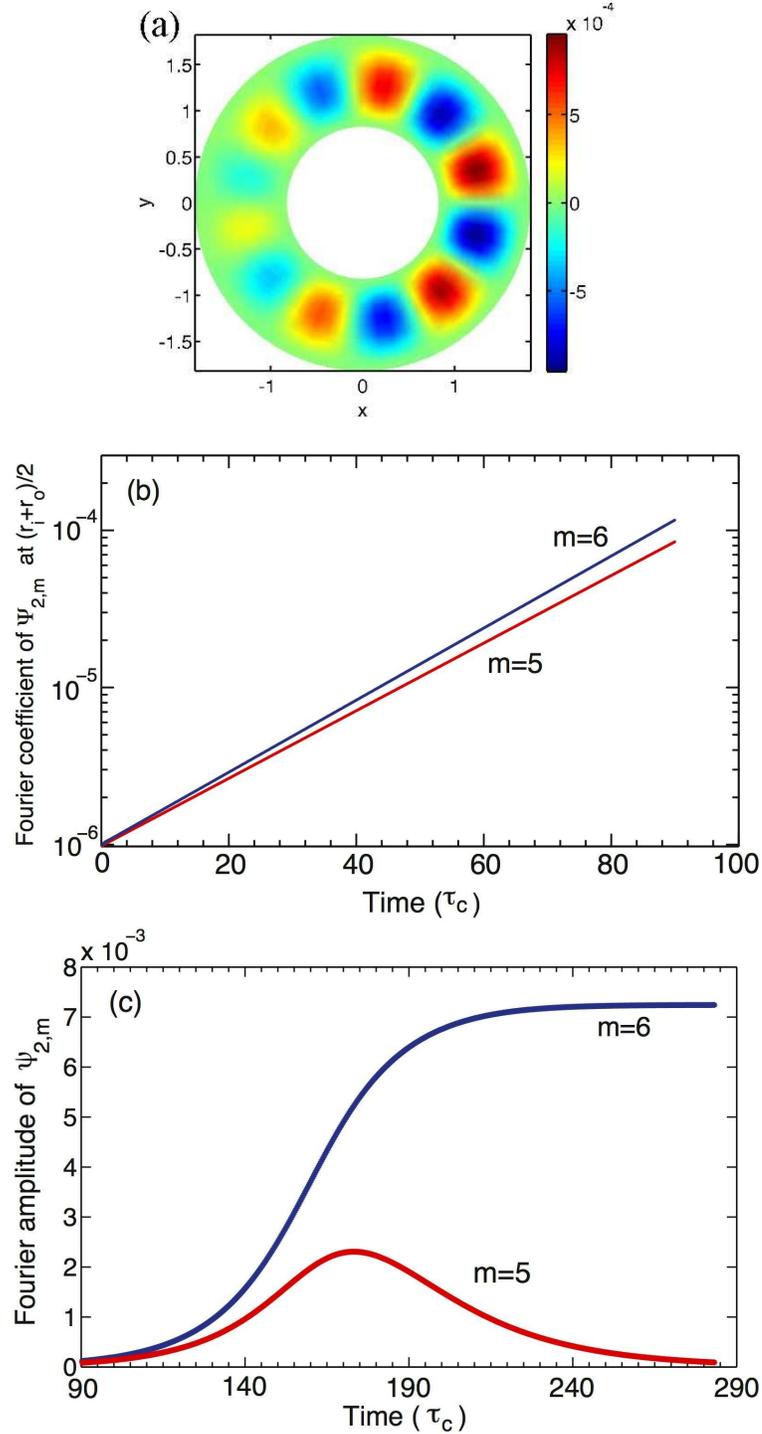
Figure 5.5: Mode competition close to the codimension-two (CoD2) point at $\alpha = 0.452$ and $\mathcal{R} = 87$. (a) The stream function of a transient mixed mode state with $m = 5$ and $m = 6$ components. This state corresponds to the Z_2 symmetric solution predicted in Ref. [85]. (b) The early time growth of the Fourier amplitudes of modes $m = 5$ and $m = 6$, starting from an initial condition of equally large amplitudes for both modes. The growth rates of $\widehat{\psi}_{2m}$ are both ≈ 0.05, for early times $\lesssim 90\ \tau_c$. (c) The full time evolution of the amplitudes of the two modes, showing that mode competition eventually results in one mode suppressing the other.
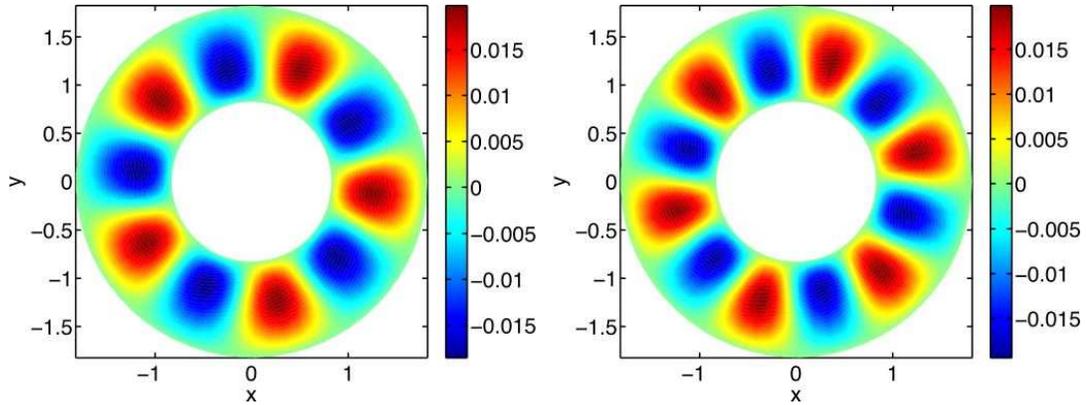
Figure 5.6: Perturbed 2D electric potential ψ_2 near a codimension-two point (CoD2) at $\alpha = 0.452$. The Rayleigh numbers were $\mathcal{R} = 87.006$ for $m = 5$ (left) and $\mathcal{R} = 87.859$ for $m = 6$ (right). Both patterns used different random white noise as the initial condition.

5.2   Sheared convection

An azimuthal shear can provide an additional experimental control parameter for smectic electroconvection by rotating the inner electrode. This 2D Couette shear, unlike the 3D Couette flow, stabilizes the convective instability and exhibits the suppression of fluid motion. Previous experimental and theoretical studies of the sheared electroconvection have focused on the weakly convective state—that is, $\mathcal{R}$ near the onset of convection. The experimental IV data, however, supply no flow fields and lack a complete physical picture of the flow dynamics undergoing various bifurcations. The newly developed simulation code, which complements experiment and theory, provides some intriguing results of sheared electroconvection with electric and flow fields. The numerical findings, the emphasis of this section, reveal new kinds of bifurcations that alter the previous explanations purely based on experimental IV data. The route to chaos in sheared convection was also numerically studied; the new observations suggest some directions for future experiment.

5.2.1   Suppression of the onset of convection

The imposed shear generates a circular Couette flow that equivalently introduces some sink terms in the dynamical equation for vorticity through nonlinear advection. Consequently, it requires higher forcing for convection to take place in sheared case, i.e., $\mathcal{R}_c > \mathcal{R}_c^0$, the latter being the critical onset without shear. Previous experimental and theoretical studies have revealed the delay of $\mathcal{R}_c$ in sheared convection [54]. The linear stability analysis showed that at a fixed α the imposed shear selects a critical mode which is linearly unstable at primary bifurcation [38]; it predicts a decreasing trend of marginally unstable mode m_c from $m_c^0 \to m_c^0 - 1 \to m_c^0 - 2 \to m_c^0 - 3 \cdots$ as Re increases from zero. In other words, the applied shear reduces the number of vortex pairs. Codimensional-two points—two types of symmetries are equally favorable— can appear for a constant α at some specific values of Re. As described previously, similar CoD2 points can also occur at some certain α under no shear.

Table 5.1 lists the numerical data for the suppression of convection due to the shear effect. $\mathcal{R}_c$ was determined by the growth rate of the amplitude of convection via $A(t) = \sqrt{Nu - 1}$. Theoretically, at $\mathcal{R}_c$— the marginally unstable point— the system takes infinite time for convection to set in because so-called critical slowing down occurs [86]. Hence, it is very difficult to observe an increase in convection at the true $\mathcal{R}_c$ in a finite time. Fortunately, very close to $\mathcal{R}_c$, the growth rate is proportional to the dimensionless relative forcing $\epsilon = \mathcal{R}/\mathcal{R}_c - 1$. Hence, $\mathcal{R}_c$—which has infinitely slow growth—was estimated by a linear approximation to the growth rates found at some other Rayleigh numbers bracketing $\mathcal{R}_c$.

The suppression is quantitatively described by $\tilde{\epsilon} = \mathcal{R}_c/\mathcal{R}_c^0 - 1 \, > 0$. The imposed shear alters the critical mode of convection patterns m_c, as shown in Table 5.1; the larger the applied shear, the smaller the critical mode m_c.

Fig. 5.7 shows the numerical data of convective current under small shears: $Re =$
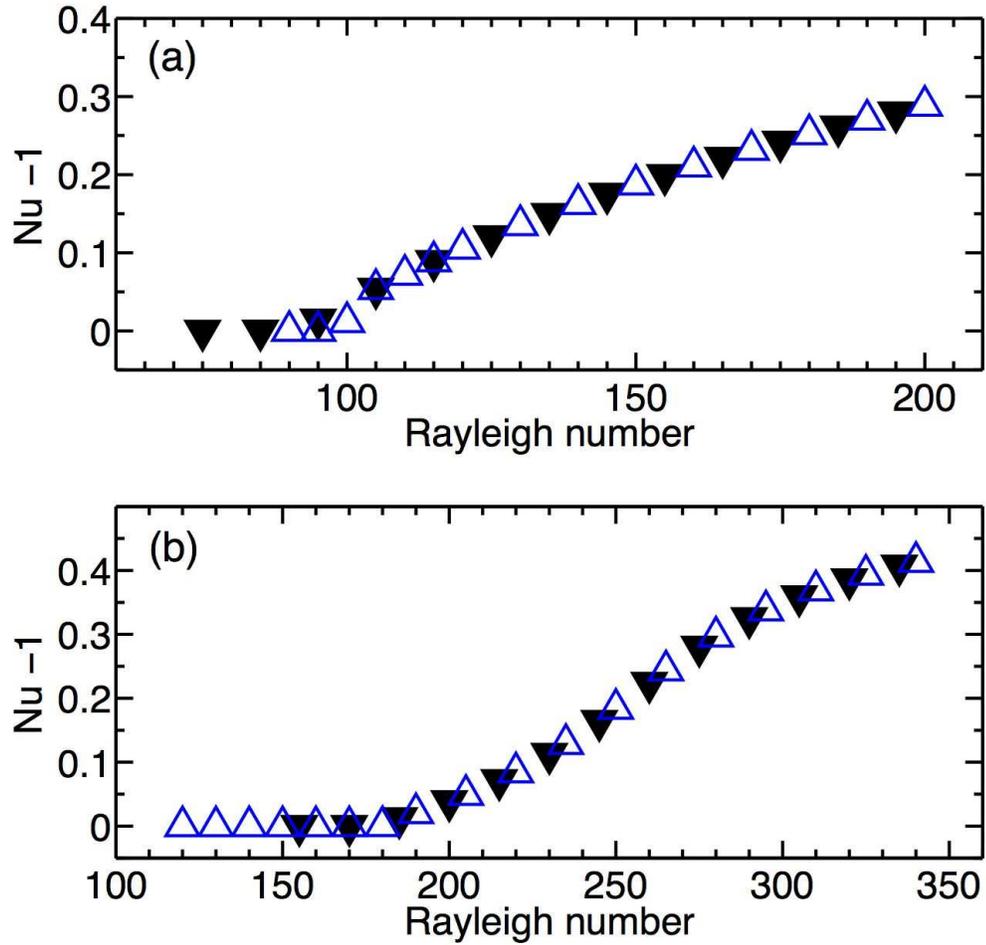
Figure 5.7: Numerical data of convective current $Nu - 1$ vs $\mathcal{R}$ under small shears: (a) $Re = 0.01$, and (b) $Re = 0.06$; both $\alpha = 0.56$, $\mathcal{P} = 75.8$. Data obtained for increasing (decreasing) $\mathcal{R}$ are shown as $\triangle$ ($\triangledown$). The suppression of convection occurs when a shear is applied. The larger the shear rate, the more suppression effect, resulting in higher onset $\mathcal{R}_c$. Both cases of the convective current show their smooth supercritical transitions when ramping $\mathcal{R}$.

Re	$\mathcal{P}$	$\mathcal{R}_c$	m_c	$\tilde{\epsilon}$	range of ϵ
0	10	87.9 ($\mathcal{R}_c^0$)	7 (m_c^0)	0	
0.01	75.8	91.9	7	0.05	$-0.05 \sim 1.10$
0.06	75.8	178.2	6	1.03	$-0.3 \sim 0.94$
0.124	75.8	309.4	6	2.5	$-0.2 \sim 0.6$
0.231	75.8	534.2	6	5.1	$-0.1 \sim 0.87$
0.249	75.8	572.0	6	5.5	$-0.1 \sim 0.27$

Table 5.1: Simulation results of the suppression of the onset of convection under various shears, Re, for $\alpha = 0.56$. $\mathcal{R}_c$ is the critical $\mathcal{R}$ number at the onset of convection under a shear, whereas $\mathcal{R}_c^0$ for non-sheared situations. m_c and m_c^0 are the critical modes at the onset with and without shear, respectively. $\tilde{\epsilon} = \mathcal{R}_c/\mathcal{R}_c^0 - 1$ is the suppression that characterizes the delay of the onset of convection due to the imposed shear. $\epsilon = \mathcal{R}/\mathcal{R}_c - 1$ describes the strength of dimensionless forcing relative to the critical forcing $\mathcal{R}_c$.

0.01, and $Re = 0.06$, at $\alpha = 0.56$, $\mathcal{P} = 75.8$. The $Nu - 1$ vs. $\mathcal{R}$ curves under small shears exhibits supercritical bifurcation, as shown in Fig. 5.7. Above $\mathcal{R}_c$, the films enter a steady convection regime in the range of ϵ between 0 and approximately 1, with stable rotating patterns due to the shear effect. These curves, illustrating a single continuous transition, are similar to those for zero shear, except that $\mathcal{R}_c$ occurs at higher value. However, in the following subsections, we will see more bifurcations readily set with larger Re applied in the same range of ϵ.

5.2.2 Hopf bifurcation and oscillatory convective current

Numerical simulations provide not only the charge flux I but also the dynamics of flow velocity, surface charge, and electric fields. These basic fields supply new insights into the flow dynamics as $\mathcal{R}$ and Re vary. For instance, the numerical results show that the films display oscillatory convection under moderate shears. In addition, the numerical data reveal that all the primary bifurcations are supercritical, even for sheared cases. This finding of supercritical primary transition is in contrast with the previous experimental study of subcritical bifurcation under a sufficiently large shear [1]. This

discrepancy very likely results from the incorrect determination of the critical voltage V_c just from experimental current-voltage (IV) curves for sheared convection. In the previous analysis of experimental data, V_c may have been mistakenly determined to be the voltage at which a sudden increase of current occurs when increasing voltage because of a very tiny convective current just right above the onset. Fig. 5.8 shows the raw experimental data for IV curves in (a), and the corresponding $Nu - 1$ vs. $\mathcal{R}$ in (b), from Fig.2a in Ref. [1]. Before, the critical voltage V_c was thought to be V_c^f (where the current has a noticeable increase) instead of a value close to V_c^*. Instead, the numerical data for electric potential show that this large sudden increase of current (near V_c^f) involves a mode change, whereas the true onset—reflecting the growth of convection and electric potential— is somewhere lower, near V_c^*. This may explain why previous experimental data of suppression $\tilde{\epsilon}$ are always systematically higher than the theoretical predictions for large Re, as shown in Fig. 7 in Ref. [38].

Fig. 5.9 shows numerical data of the convective current, $Nu - 1$, vs. $\mathcal{R}$ in the sheared convection of $\alpha = 0.56, \mathcal{P} = 75.8, Re = 0.124$, the same parameters as in the experiment presented in Fig. 5.8. Under this constant shear, the film undergoes a sequence of bifurcations as $\mathcal{R}$ is slowly increased (data points depicted in $\triangle$): the conduction regime (in black), steady convection (in blue), oscillatory convection (in red) with the bars showing the oscillation amplitude, and then a subcritical bifurcation (shown by an increase of convective current) that involves a mode change. In our simulation, the primary bifurcation shows the growth of perturbed electric potential noise and the growth of the velocity field from the quiescent state. The onset of convection is shown to be $\mathcal{R}_c = 309.4$, while the sudden jump of current is located at $\mathcal{R} \approx 387$. The suppression of onset accordingly is $\tilde{\epsilon} = \mathcal{R}_c/\mathcal{R}_c^0 - 1 = 2.5$ and the critical onset mode $m_c = 6 < m_c^0 = 7$. These numerical data are consistent with previous theoretical calculations, which yield $\tilde{\epsilon} = 2.1, m_c = 6 < m_c^0 = 7$, using a local linear stability analysis [38].
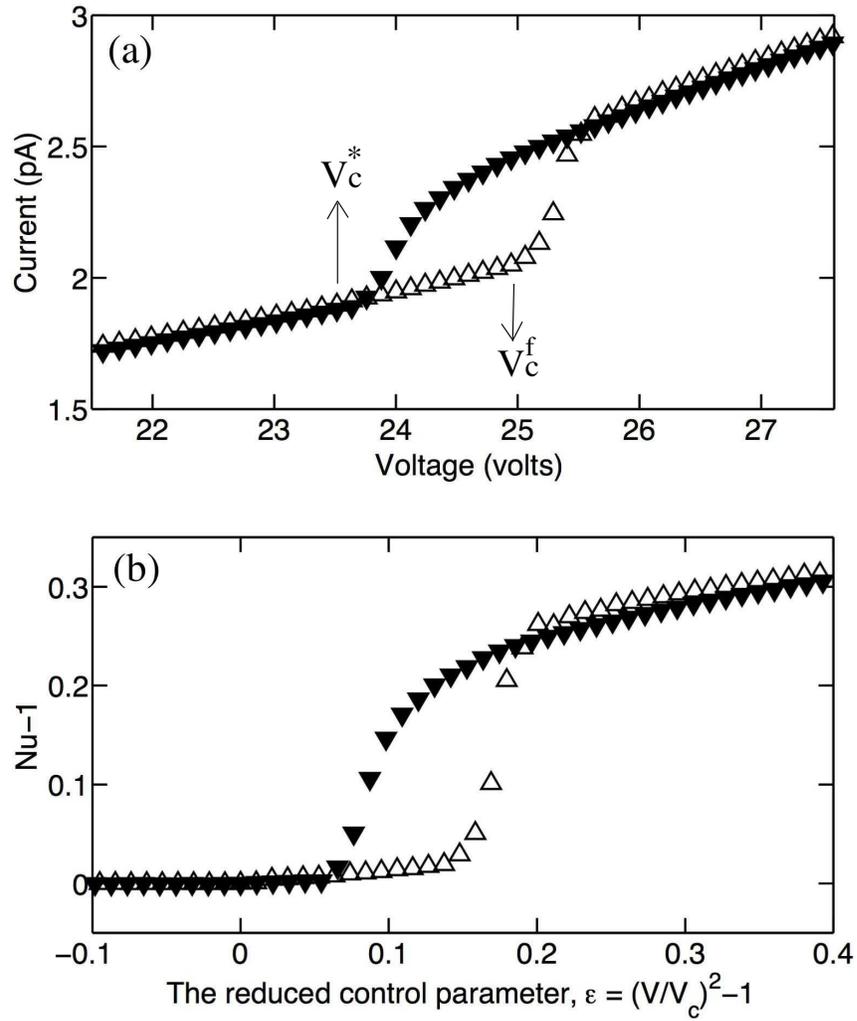
Figure 5.8: (a) Experimental raw current-voltage data from Ref. [1] for $\alpha = 0.56$, $\mathcal{P} = 76$, and $Re = 0.124$. The open (filled) triangles are for increasing (decreasing) voltage. (b) The corresponding measured dimensionless convective current, $Nu - 1$, *vs.* dimensionless control parameter $\epsilon = (V/V_c)^2 - 1$, extracted from the data in (a).
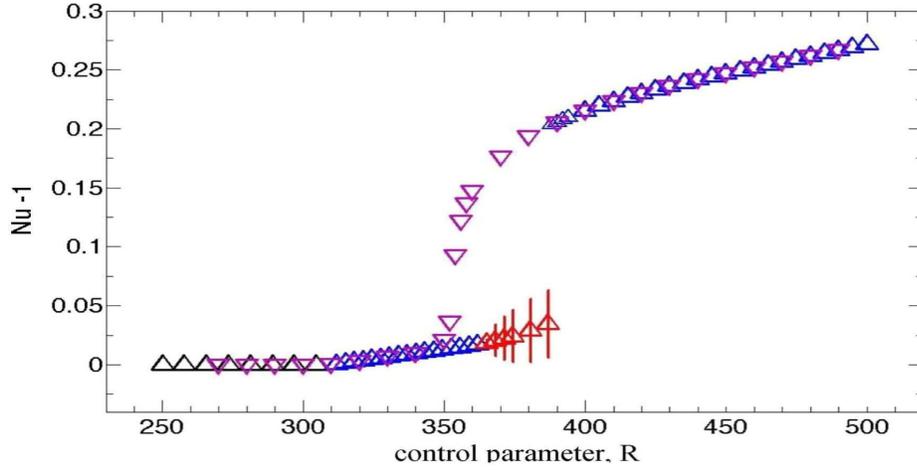
Figure 5.9: Simulation results for convective current, described by $Nu - 1$, as $\mathcal{R}$ changes in the sheared convection with $\alpha = 0.56$, $\mathcal{P} = 75.8$, and $Re = 0.124$. The film undergoes a sequence of bifurcations: as $\mathcal{R}$ is slowly increased (data points shown as $\triangle$), the film undergoes conduction (in black), steady convection (in blue), oscillatory convection (in red) with bars showing the oscillation amplitude, and then a subcritical bifurcation, showing by an increasing jump in current, which involves mode changes. The film exhibits IV hysteresis when decreasing $\mathcal{R}$ shown by $\bigtriangledown$.

In Fig. 5.9, as $\mathcal{R}$ gradually increases beyond the steady sheared convection regime, a Hopf bifurcation sets in leading to periodic motion. The first onset of oscillatory motion under a moderate shear happens around 18% of $\mathcal{R}_c$ above $\mathcal{R}_c$. In this oscillatory regime, the flow velocity and electric fields periodically oscillate, in addition to the overall rotation due to the imposed shear. Fig. 5.10 shows time-series data of oscillating convective current at $\mathcal{R} = 371.3$ and $\mathcal{R} = 386.9$. After $\sim 10 \ \tau_c$, these time-series data reveal periodic oscillations of a one-frequency (1-f) limit cycle. The corresponding phase spaces are also shown in Fig. 5.10 (on the right), using the time-delay method with a sufficiently long time-series data of $Nu - 1$. These oscillation frequencies for $\mathcal{R} = 371.3$ and $\mathcal{R} = 386.9$ are 0.40 and 0.50 ($1/\tau_c$), respectively. Simultaneously, the overall rotational rate due to the imposed shear, measured in the range of $\mathcal{R}$ between 390 and 394, is 2.36 (rad/τ_c) counterclockwise. Fig. 5.11 shows that the fundamental oscillation frequency of the 1-f limit cycle regime changes slightly
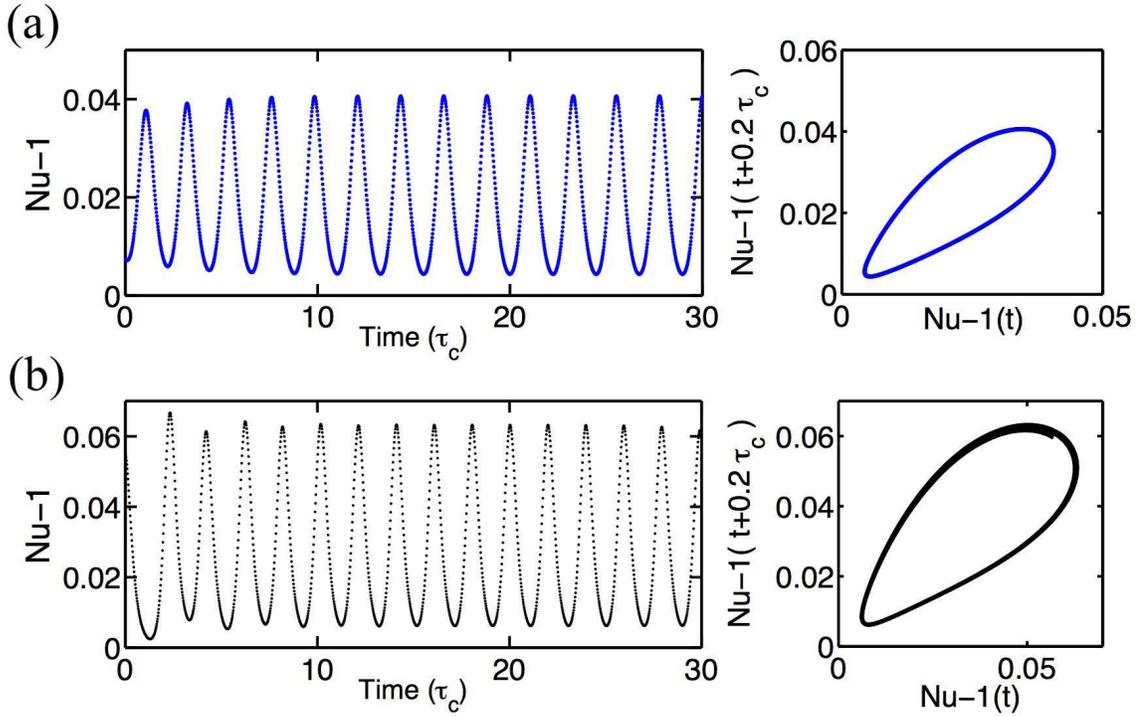
Figure 5.10: Numerical time-series data for oscillatory convective current $Nu - 1$ at $\alpha = 0.56, \mathcal{P} = 75.8$, and $Re = 0.124$ at two different $\mathcal{R}$: (a) $\mathcal{R} = 371.3$ and (b) $\mathcal{R} = 386.9$. Their corresponding phase spaces after 10 τ_c are also shown on the right, using the time-delay method with a sufficiently long time-series data of $Nu - 1$.

between 0.40 and 0.50, without a general trend, as $\mathcal{R}$ increases from 365 to 390.

Numerical data suggest a threshold of Re for the presence of Hopf bifurcation since oscillatory convection was not observed for small imposed shears, such as $Re = 0.01$ and $Re = 0.06$ (discussed in the previous subsection), in a similar dimensionless forcing range. As a future project, more simulations, with different values of Re between 0.06 and 0.124, are required to investigate the strength of this cut-off shear. In summary, a sufficiently large shear Re—acting as the second control parameter in addition to $\mathcal{R}$—can prompt a Hopf bifurcation which takes place in at least two-dimensional phase space, comparing with a smooth supercritical bifurcation in one-dimensional phase space with no applied shear. As a result, a complicated parameter space of patterns can be expected for electroconvection under electric forcing and shear simultaneously. In the next subsection, we will encounter a discontinuous transition which
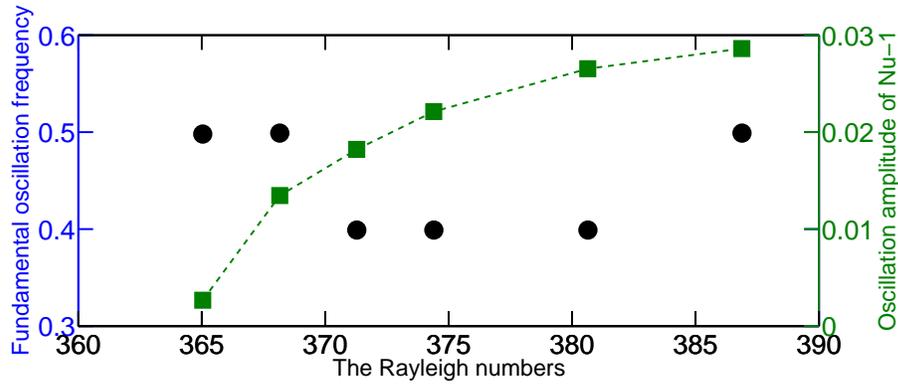
Figure 5.11: The fundamental frequencies (•) and the oscillation amplitudes (■) of $Nu - 1$ as a function of $\mathcal{R}$ in a sheared convective state at $\alpha = 0.56, \mathcal{P} = 75.8$, and $Re = 0.124$.

involves a mode change and enhances charge transport, under a larger shear and after Hopf bifurcation.

5.2.3   The dynamics of mode change under shear

Previous experimental IV data showed a series of bifurcations for a sequence of increasing Re [1], and mode-changing bifurcations were thought to be responsible for a sudden increase of current. A mode change, indeed, can boost the convective current, as shown in Fig. 5.9 near $\mathcal{R} = 387$. The mode-changing transition, as revealed in Fig. 5.12, can be due to a large change in the modes m of perturbed electric potential patterns: $m = 6$ before the subcritical bifurcation (a), whereas $m = 2$ after (b). In contrast to the previous conjecture (purely based on IV data) that m changes discretely by only one vortex pair [1], numerical data show that the new mode can be different by a large number of pairs instead of bifurcating to $m \pm 1$. Fig. 5.13 shows the dynamics of mode competition at a subcritical bifurcation for $\mathcal{R} = 388.0$ in Fig. 5.9. Initially, the $m = 6$ mode dominates and simultaneously oscillates, soon thereafter the $m = 5$ mode dominates and oscillates. However, both modes decrease to steady values. These competing modes are coupled to the adjacent modes $m - 1$ or $m + 1$,

and eventually, when time $> 20\ \tau_c$, Fourier modes $m = 2$ and $m = 4$ reach certain significant steady amplitudes. After the mode change, the film undergoes a transition to a steady convective regime and exhibits current hysteresis when decreasing $\mathcal{R}$ in the range of $342 < \mathcal{R} < 388$. The time series data of the kinetic energy for decreasing $\mathcal{R}$ show over-damped oscillation-like motions. When decreasing $\mathcal{R}$ from 500 back to 340, the originally dominant Fourier modes $m = 2$ and $m = 4$ decay to essentially zero and $m = 6$ decays to a steady state. The intersection of IV for decreasing and increasing $\mathcal{R}$ obtained from simulations lies in the steady convection regime (above the onset $\mathcal{R}_c$) with 6 counter-rotating vortex pairs.

Fig. 5.14 illustrates a more complex subsequence of bifurcations under a larger shear $Re = 0.231$, compared to $Re = 0.124$ shown previously, for the same α and $\mathcal{P}$ in Fig. 5.9. In the ϵ-range between 0 and 0.87, the film undergoes several transitions: first, from conduction to steady convection with the critical mode $m = 6$; second, from steady convection to oscillatory convection with $m = 6$; third, a subcritical bifurcation from the steady oscillatory convection to steady convection with the dominant physical patterns of 1 counter-rotating vortex pair. Fourth, a Hopf bifurcation again from the steady to the oscillatory convection of the dominant mode $m = 1$. Fifth, a subcritical bifurcation from the oscillatory convection $m = 1$ to a steady convection with $m = 2$. Fig. 5.15 shows the corresponding snapshots of physical patterns of the perturbed electric potential $\psi_2^{(1)}$, presenting different states at various $\mathcal{R}$.

The numerical results of convective current $Nu - 1$, shown in Fig. 5.14, are consistent with previous experimental measurements, depicted in Fig. 2g of Ref. [1], for the same parameters. The experiment data showed that $Nu - 1$ undergoes two subcritical transitions, the first one from $\gtrsim 0$ to ≈ 0.2 and the second one from $\gtrsim 0.2$ to ≈ 0.4 for increasing voltage; this agrees with numerical results (shown in Fig. 5.14). However, simulation results offer different explanations of physical convec-
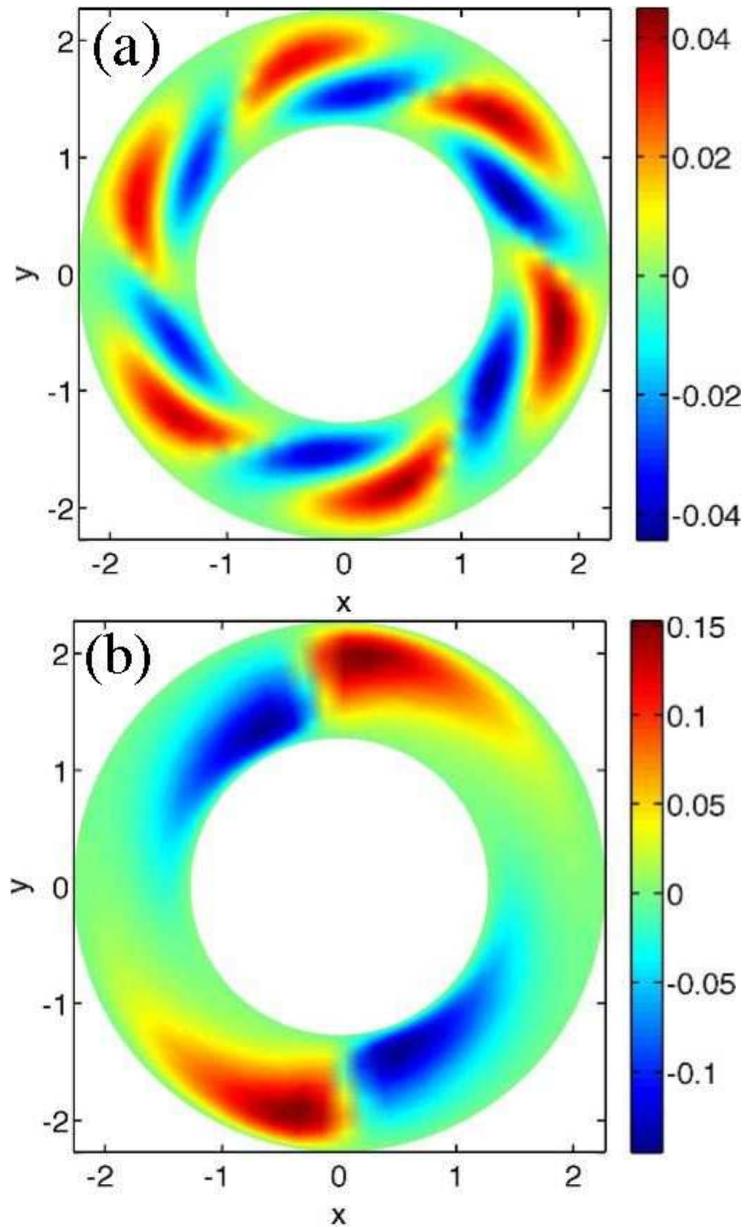
Figure 5.12: Perturbed electric potential, which is total ψ subtracting out the conductive profile, corresponding to Fig. 5.13 at $\mathcal{R} = 388.0$: (a) initially, at $t = 0$, there are 6 counter-rotating vortex pairs, whereas (b) at $t = 30\tau_c$ there are only 2 vortex pairs, which is comprised of a band of Fourier modes shown in Fig. 5.13.
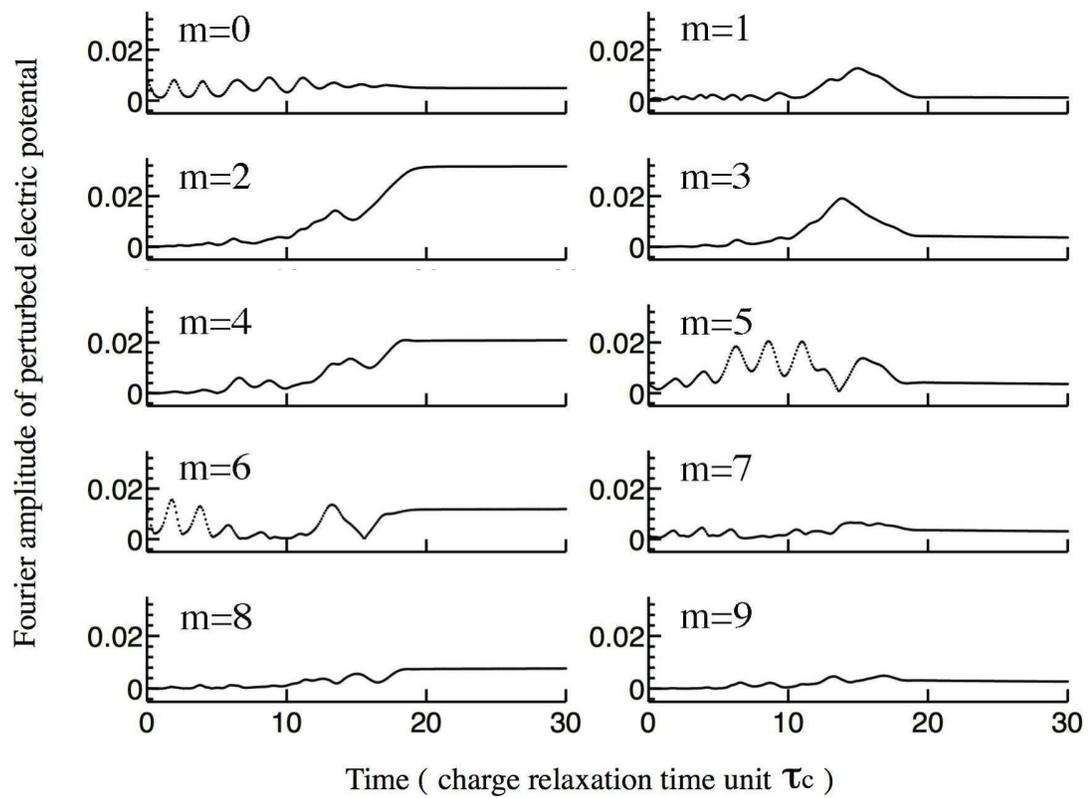
Figure 5.13: The dynamics of a mode change at a subcritical bifurcation for $\mathcal{R} = 388.0$ in Fig. 5.9: the time-series data of Fourier amplitudes of the perturbed electric potential $\widehat{\psi}_{2m}(t)$ at the middle radius.
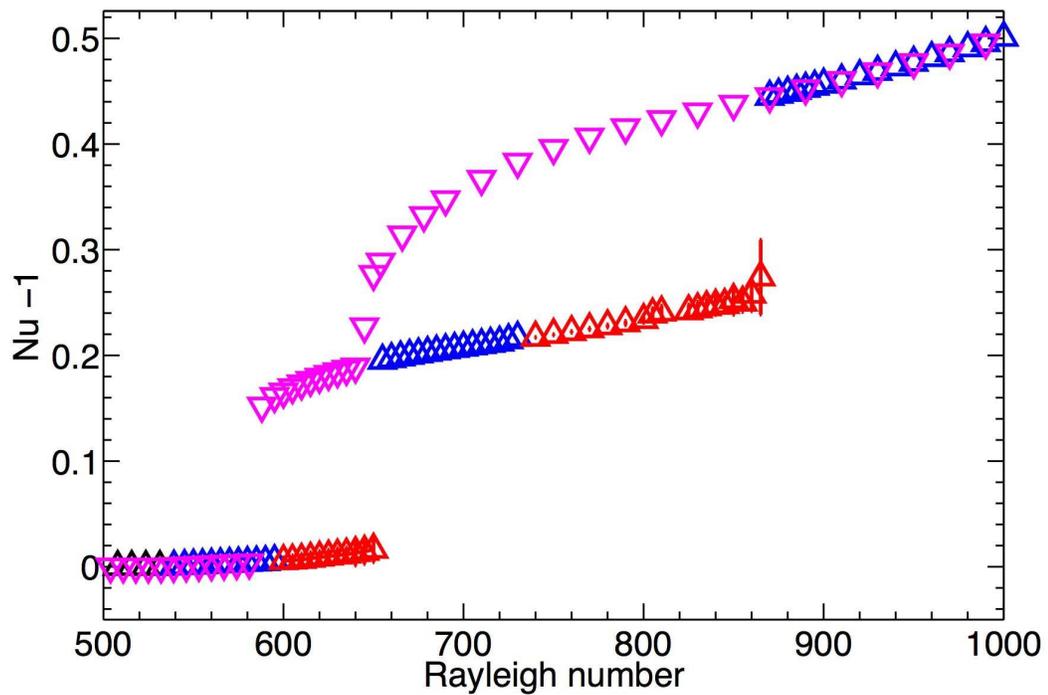
Figure 5.14: A subsequence of bifurcations in a sheared convection for $\alpha = 0.56$, $\mathcal{P} = 75.8$, $Re = 0.231$. Data of convective current obtained for increasing (decreasing) $\mathcal{R}$ are shown as $\triangle$ ($\triangledown$). For increasing $\mathcal{R}$, black $\triangle$ indicates the conduction regime; blue $\triangle$ indicates the steady convection regime; red $\triangle$ indicates the oscillatory regime with the bars showing the amplitude of oscillation.
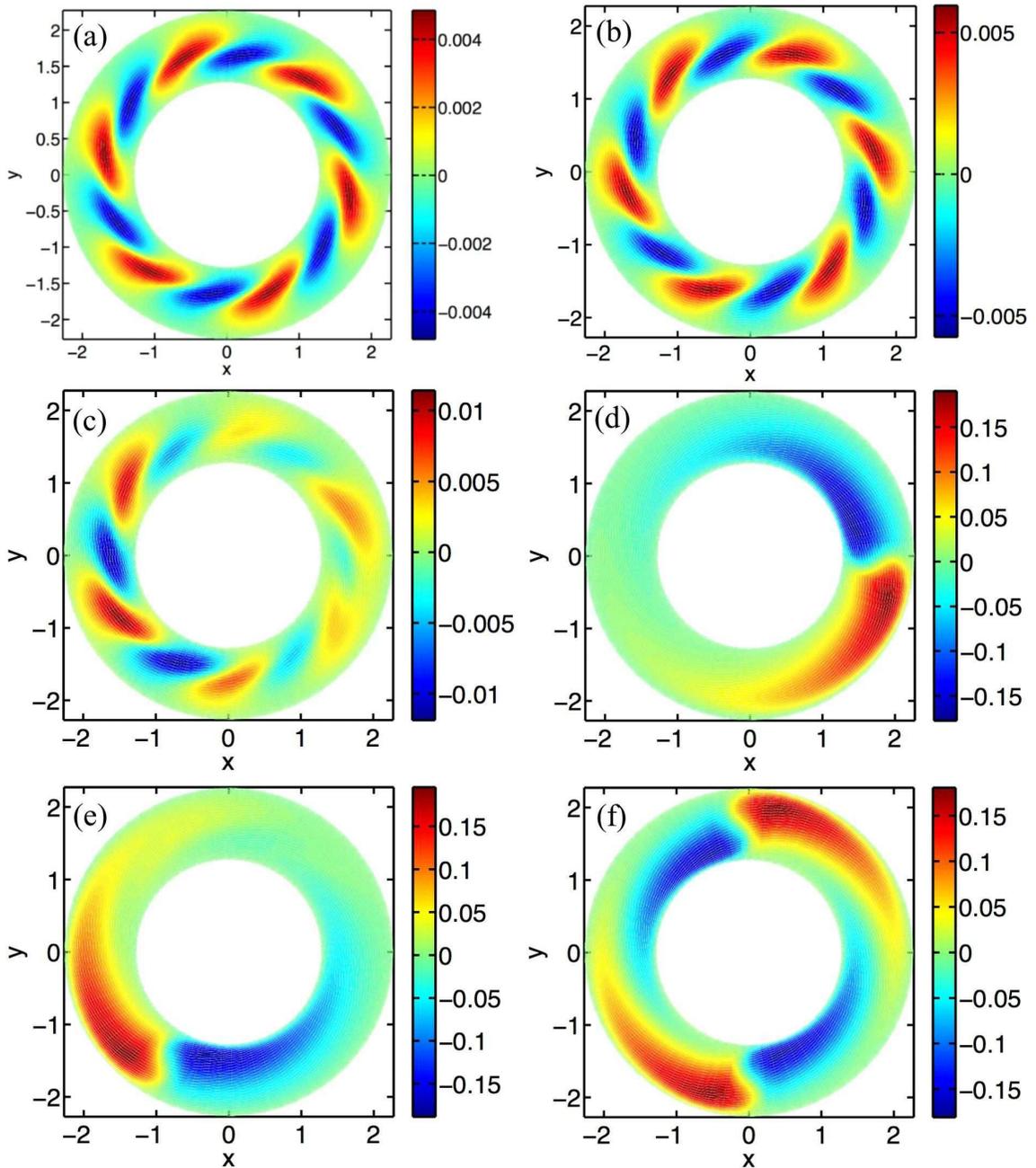
Figure 5.15: Snapshots of the physical patterns of perturbed electric potentials, $\psi_2^{(1)}$, at different $\mathcal{R}$ in a sheared convection for $\alpha = 0.56$, $\mathcal{P} = 75.8$, $Re = 0.231$. These patterns correspond to a variety of states illustrated in Fig. 5.14 when increasing $\mathcal{R}$: (a) steady convection of $m = 6$ vortex pairs for $\mathcal{R} = 550$, at $30\tau_c$; (b) oscillatory convection of $m = 6$ vortex pairs for $\mathcal{R} = 600$, at $30\tau_c$; (c) undulating convection of a mode change for $\mathcal{R} = 650$, at $30\tau_c$; (d) steady convection of $m = 1$ vortex pair, after a subcritical transition, for $\mathcal{R} = 700$, at $30\tau_c$; (e) oscillatory convection of $m = 1$ vortex pair for $\mathcal{R} = 800$, at $20\tau_c$; (f) steady convection of $m = 2$ vortex pair for $\mathcal{R} = 900$, at $20\,\tau_c$, after another discontinuous transition.

tion patterns from the previous ones that are conjectured merely from experimental IV data [1]. Simulation results of the perturbed electric potential revealed Hopf bifurcations and mode-changing subcritical bifurcations, which invoke the interaction of a broad band of azimuthal modes and result in convection patterns of few vortex pairs (see, for example, Fig. 5.12 and Fig. 5.15). Whereas, the previous conjectures suggest that when increasing $\mathcal{R}$, the subcritical bifurcations correspond to mode transitions $m \to m+1 \to m+2 \to \cdots$ [1]. Nevertheless, these conjectures are incomplete because of no flow visualization and no theoretical work yet for these secondary bifurcations. Here, the simulation results, providing complete flow dynamics and local fields, reveal that these subcritical bifurcations can largely change the charge transport and result in new emergent, simple form of order patterns through the nonlinear interactions of several azimuthal modes.

5.2.4 Route to chaos

The sequence of bifurcations, the so-called route to chaos, is an important approach, alternative to the conventional statistical analysis, for understanding turbulent flow [87]. For example, large coherent structures usually found in convective turbulence can be associated with the form of instabilities of steady convection patterns [14]. Each bifurcation out of equilibrium, connected to a symmetry-breaking, provides a new mechanism for momentum or heat transport.

The boundary conditions of a confinement have profound influences in a fluid dynamical system. Recently, many studies have shown that boundary conditions significantly affect the flow phenomenology on the various routes to chaos [88, 89, 90]. For example, a numerical study with one periodic and one stress-free boundary conditions, mimicking a laboratory experiment of electromagnetically forced quasi-2D flows in shallow fluid layers [91], shows a period-doubling cascade to chaos [88]. Some computations with two periodic boundary conditions reveal more complex transitions in-

volving traveling waves and many sequences of quasi-periodic motions [89]. Whereas, simulations on a confined 2D flow in a unit cell with both non-slip boundary conditions reveal the Ruelle-Takens-Newhouse scenario [90]. Its transition sequence consists of a steady state, periodic flow (period-1 limit cycle), two-frequency quasi-periodic flow (2-torus), three-frequency quasi-periodic flow (3-torus), and chaotic flow [92, 93]. This scenario has also been observed in the Rayleigh-Bénard convection (see Ref. [19] for the reviews). Motivated by these physical phenomenon, the transition to chaos was studied in 2D annular electroconvection, which has one periodic and one non-slip boundary conditions.

The numerical results reveal the Ruelle-Takens-Newhouse scenario, illustrated in Fig. 5.16, as route to chaos in sheared convection for $\alpha = 0.47, \mathcal{P} = 16.3$, and $Re = 0.8$. Fig.5.16 shows the attractors of distinct states obtained with the time-delayed method, using the time-series data of $Nu - 1$. It is sufficient to reconstruct the phase space of the attractors just with time-series data [94]. The suppression of onset in our simulation is $\tilde{\epsilon} = 3.96$, compared to the theoretical prediction of $\tilde{\epsilon} = 3.6$ [37], at $\alpha = 0.47, \mathcal{P} = 16.3$, and $Re = 0.8$. The steady convective state exhibits $m = 5$ laminar counter-rotating vortex pairs, which agrees with theoretical prediction. Fig. 5.16a reveals a 1-frequency periodic motion at $\mathcal{R} = 485.6$ with the basic frequency $f_1 \sim 0.60 \ (1/\tau_c)$. In the subsequent motions in the $1f$-periodic state, the basic frequency slightly changes in the range of $0.40 \sim 0.50 \ (1/\tau_c)$ as $\mathcal{R}$ increases. The 2-torus motion at $\mathcal{R} = 639.3$ has the fundamental frequencies $f_1 = 0.70$, and $f_2 = 0.80 \ (1/\tau_c)$. The flow that lies on period-3 torus $\mathcal{R} = 673.4$ has the basic frequencies $f = 0.31, 0.69$, and $1.31 \ (\text{in } 1/\tau_c)$, and at higher $\mathcal{R} = 1190$ a chaotic motion takes place (see Fig. 5.16d).

Our numerical observation, following the Ruelle-Takens-Newhouse scenario of route to chaos, shows this open, dissipative system can become chaotic just after two or three hopf bifurcations, i.e., in finite steps of instabilities. This route is strongly in contrast to the Landau's picture [71] which proposed the transition to turbulent mo-
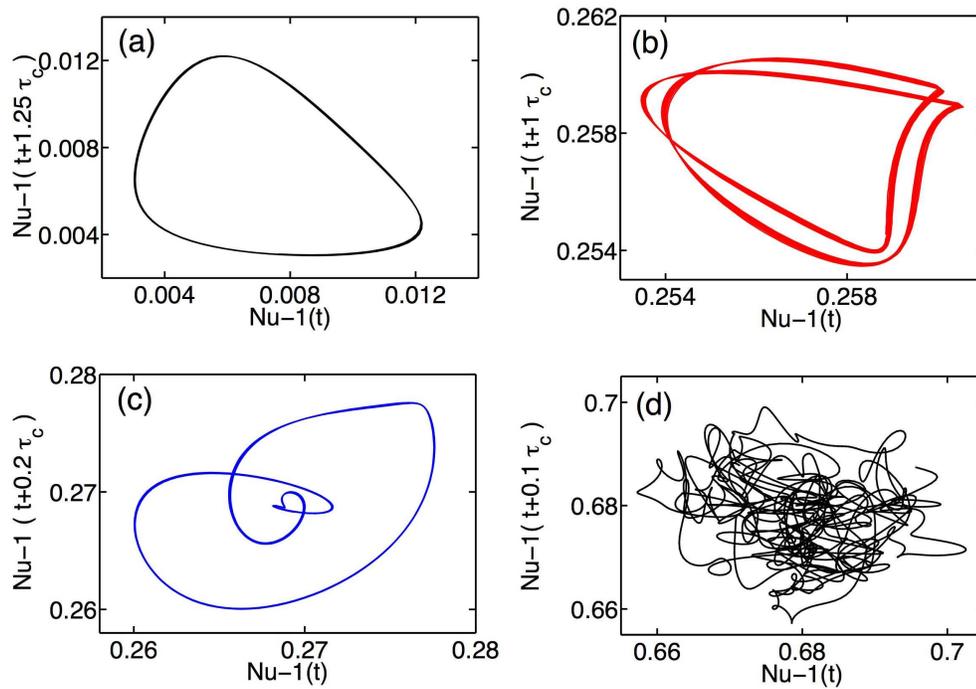
Figure 5.16: Projections of the system attractor of $Nu - 1$ (t) using the time-delayed method in the sheared convection of $\alpha = 0.47, \mathcal{P} = 16.3$, and $Re = 0.8$, showing the Ruelle-Takens-Newhouse scenario for the route to chaos: (a) a 1-frequency limit cycle at $\mathcal{R} = 485.8$, (b) 2-frequency quasi periodic flow (2-torus) at $\mathcal{R} = 639.3$, (c) 3-frequency quasi periodic flow (3-torus) at $\mathcal{R} = 673.4$, and (d) chaotic flow at $\mathcal{R} = 1190$.

tions to undergo an infinite sequence of instabilities and ultimately to reach a broad band of power spectrum.

The observations that the Ruelle-Takens-Newhouse type is not the only approach to turbulence in Rayleigh-Bénard convection imply the possibility of other probable roads to chaos in annular electroconvection. Other common scenarios that have been verified in some convection experiments [19, 95] include period-boubling bifurcations [96], and intermittent non-periodic transition [97]. These various roads to turbulence, with their mathematical descriptions, show that a deterministic chaos appears after some or a sequence instabilities and the actual route is very sensitive to the initial type of bifurcations and the states of a dynamical system. Hence, we may expect that many routes to chaos exist in annular electroconvection because of its broad phase space of $(Re, \mathcal{R}, \mathcal{P}, \Gamma)$. As a research prospect, the combination of experiment and simulation can provide more understanding of the detailed dependence of route to chaos on these experimental parameters. The next section is devoted to the discussions of turbulence in annular electroconvection under strong electric forcing with no applied shear.

5.3 Convective turbulence

Vigorously forced electroconvection exhibits a turbulent state, in which experimental IV measurements show charge transport scaling and highly chaotic time-series data of charge flux with a broad band of frequencies. The charge transport Nu was experimentally investigated under high electric forcing with various films, in particular the influences of Prandtl number and aspect ratios on Nu. The experimental data revealed Nu power-laws scaled with $\mathcal{R}$. These observations were completely new for annular electroconvection and thus motivated more studies with numerical simulations and a scaling theory. This section presents experimental, theoretical, and numerical results of turbulent electroconvection, together with their comparisons; particularly, the results of Nu scaling, and some essential local fields provided by numerical calculations at various high $\mathcal{R}$ numbers.

5.3.1 Charge transport scaling of $Nu \sim \mathcal{R}^{\gamma}$

Experimental IV measurements, which are alternatively described by dimensionless parameters of Nu and $\mathcal{R}$, characterizes the states of electroconvection. Fig. 5.17 shows Nu *vs.* $\mathcal{R}$ data for three aspect ratios Γ, obtained from the IV data. When $Nu = 1$, the fluid is quiescent. When $Nu > 1$, the fluid is convecting. Unsteady flow, which is indicated by large current fluctuation, sets in when $\mathcal{R} \sim O(10^3)$. For $\mathcal{R} \gtrsim 10^4$, the data reveal power law behavior with $Nu \sim \mathcal{R}^{\gamma}$ and values of γ close to either $1/5$ or $1/4$. Detailed experimental results for various Γ and $\mathcal{P}$ are listed in Table 5.2. The Rayleigh number $\mathcal{R}$ range used to fit $Nu \sim \mathcal{R}^{\gamma}$ was between approximately $100\mathcal{R}_c$ and the final data point at the largest accessible DC voltage, 1000 volts. Note that in Fig. 5.17a, the critical Rayleigh number $\mathcal{R}_c$ at the onset of convection is ~ 100, and thus a factor of 10 smaller than the corresponding $Ra_c = 1708$ for Rayleigh-Bénard convection. This is in agreement with the detailed linear stability analysis of annular
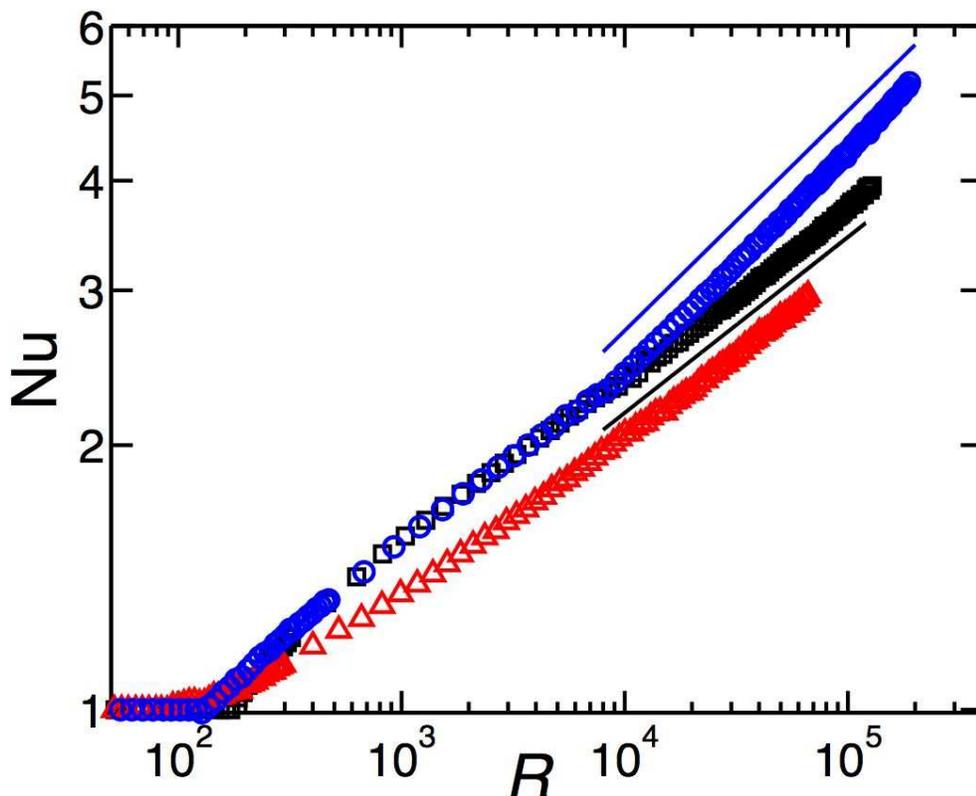
Figure 5.17: Representative plots of Nu vs $\mathcal{R}$ for $\Gamma = 0.33 \pm 0.01$ ($\triangle$), 3.74 ± 0.02 ($\square$), and 6.60 ± 0.02 ($\circ$), analyzed by piecewise drift correction Method A. For these, $\mathcal{P} = 8.8 \pm 0.5$, 21 ± 1, and 36 ± 1, respectively. Least-square fits to the power-law $Nu \sim \mathcal{R}^\gamma$ give best fit values $\gamma = 0.19 \pm 0.01$, 0.21 ± 0.02, and 0.26 ± 0.01, respectively. The solid reference lines in the figure have slopes of $1/5$ (lower one) and $1/4$ (upper one).

electroconvection presented in Ref. [38].

From a total of 46 experiments with various smectic films, the scaling exponents γ were either 0.20 ± 0.03 or 0.25 ± 0.02, depending on $\mathcal{P}$, with the data analysis using piecewise Method A for the conduction drift correction. Consistent with this, the scaling exponents γ were either 0.19 ± 0.03 or 0.24 ± 0.02 with the data analysis by linear Method B. These methods use different approximations to account for conductance drift; they are previously described in detail in Chapter 2, Section 2.5. The error bars quoted cover the scatter in γ and also include the uncertainties in the film thickness, the critical voltage, and the film conductance drift. In Fig. 5.18

Γ	range of $\mathcal{P}$	γ	range of $\mathcal{R}$
0.33	$6 - 9$	0.21 ± 0.02	$8 \times 10^3 - 7 \times 10^4$
1.54	$19 - 28$	0.21 ± 0.01	$1 \times 10^4 - 2 \times 10^5$
3.74	$21 - 25$	0.22 ± 0.02	$2 \times 10^4 - 2 \times 10^5$
6.6	$25 - 41$	0.24 ± 0.04	$2 \times 10^4 - 2 \times 10^5$
6.6	$48 - 61$	0.21 ± 0.01	$2 \times 10^4 - 3 \times 10^5$
11.1	$70 - 74$	0.25 ± 0.02	$1 \times 10^4 - 2 \times 10^5$
11.1	$112 - 120$	0.18 ± 0.01	$2 \times 10^4 - 4 \times 10^5$
11.1	$127 - 136$	0.19 ± 0.01	$2 \times 10^4 - 4 \times 10^5$
16.1	$205 - 241$	0.18 ± 0.02	$8 \times 10^3 - 5 \times 10^5$

Table 5.2: Experimental results of fits to $Nu \sim \mathcal{R}^\gamma$ at high Rayleigh numbers, for different aspect ratios Γ and various Prandtl numbers $\mathcal{P}$ by piecewise drift correction Method A. Results obtained by linear drift correction Method B are consistent. Methods A and B are fully described in Chapter 2, Section 2.5.
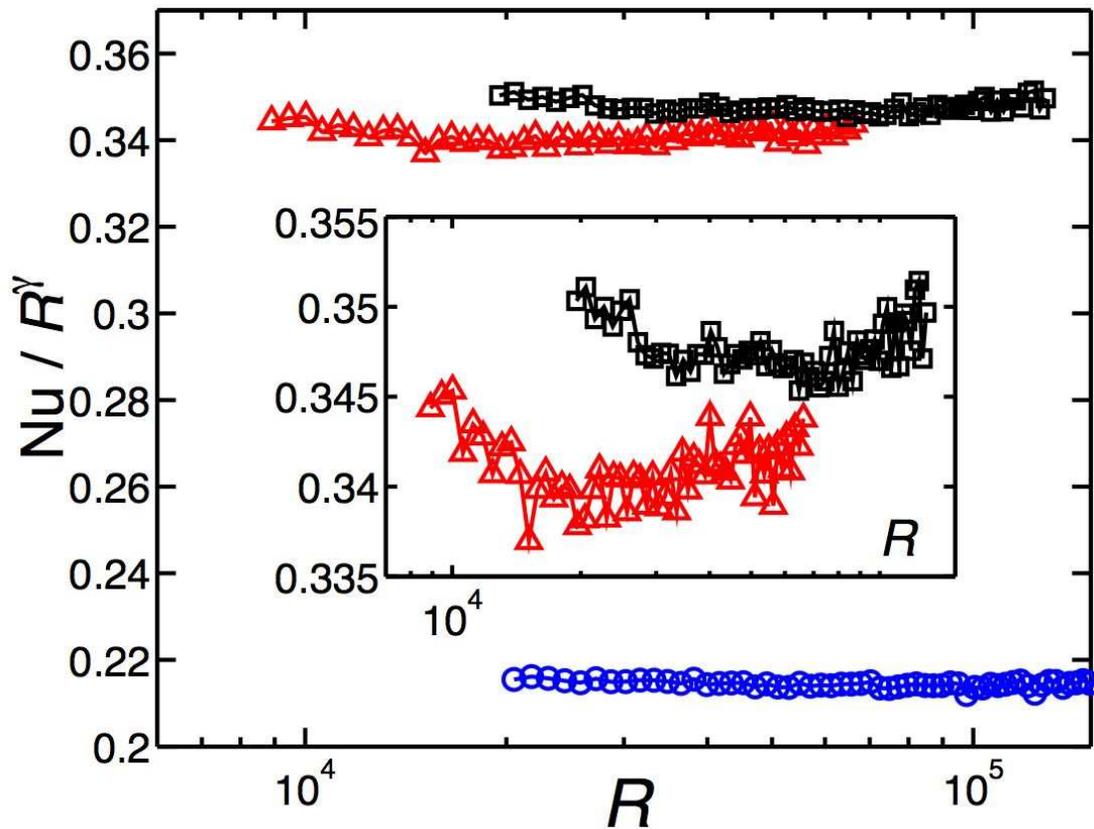

Figure 5.18: Plots of the compensated scaling $Nu\, \mathcal{R}^{-\gamma}$ vs. $\mathcal{R}$ for the same data as in Fig. 5.17. Inset shows a more expanded scale for $\Gamma = 0.33$ ($\triangle$), and 3.74 ($\square$).

compensated plots of $Nu/\mathcal{R}^\gamma$ vs. $\mathcal{R}$ are shown. The best fit exponent γ obtained from experiments was used to compensate the Nu data. Although only about one decade of scaling range is available, the compensated plots show that a local power law is an adequate description of the data.

The scaling theory, as described in Chapter 4, Section 4.3, predicts the $Nu - \mathcal{R}$ scaling exponent γ to be 1/4 or 1/5 depending on $\mathcal{P}$ for the relatively small $\mathcal{R}$ in the turbulent regime. The experimental results, despite spanning in wide parameter ranges of $0.3 \lesssim \Gamma \lesssim 17$ and $5 \lesssim \mathcal{P} \lesssim 250$, show a good agreement with the theoretical predictions of $Nu \sim \mathcal{R}^\gamma$ scaling exponents γ close to 1/4 or 1/5, at electric forcing $10^4 \lesssim \mathcal{R} \lesssim 5 \times 10^5$.

5.3.2 The dependence of Nu on the Prandtl number $\mathcal{P}$

The electric Prandtl number $\mathcal{P}$ defined by Eqn. 3.14 is the dimensionless ratio of the charge and viscous relaxation time scales. $\mathcal{P}^{-1}$ appears as a prefactor in the nonlinear and time derivative terms when the equations of motion are written in dimensionless variables. It is thus reasonable that any dependence on $\mathcal{P}$ vanishes for large $\mathcal{P}$. However, for $\mathcal{P} \sim 1$ the turbulent flow and scalings are expected to depend on $\mathcal{P}$. The relative length scales of the electric potential and viscous boundary layers, which depend on $\mathcal{P}$, enter into the scaling arguments of Grossmann and Lohse [32]. For Rayleigh-Bénard convection, GL theory predicts that Nu should exhibit local power law scalings with Prandtl number, albeit with rather small powers [32, 33]. Rayleigh-Bénard convection experiments suggest that the heat transport is largely independent of the Prandtl number between 4 to 1350. For example, it has been found that $Nu \sim \mathcal{P}^{-0.03}$ at $\Gamma = 1$ [78]. In turbulent electroconvection for $2 \times 10^4 \lesssim \mathcal{R} \lesssim 10^5$, experimental data show that Nu varies by only a factor of 2 over the broad range $5 \lesssim \mathcal{P} \lesssim 250$.

Fig. 5.19 shows a plot for Nu vs. $\mathcal{P}$ for two aspect ratios $\Gamma = 6.6$ and 11.1. At
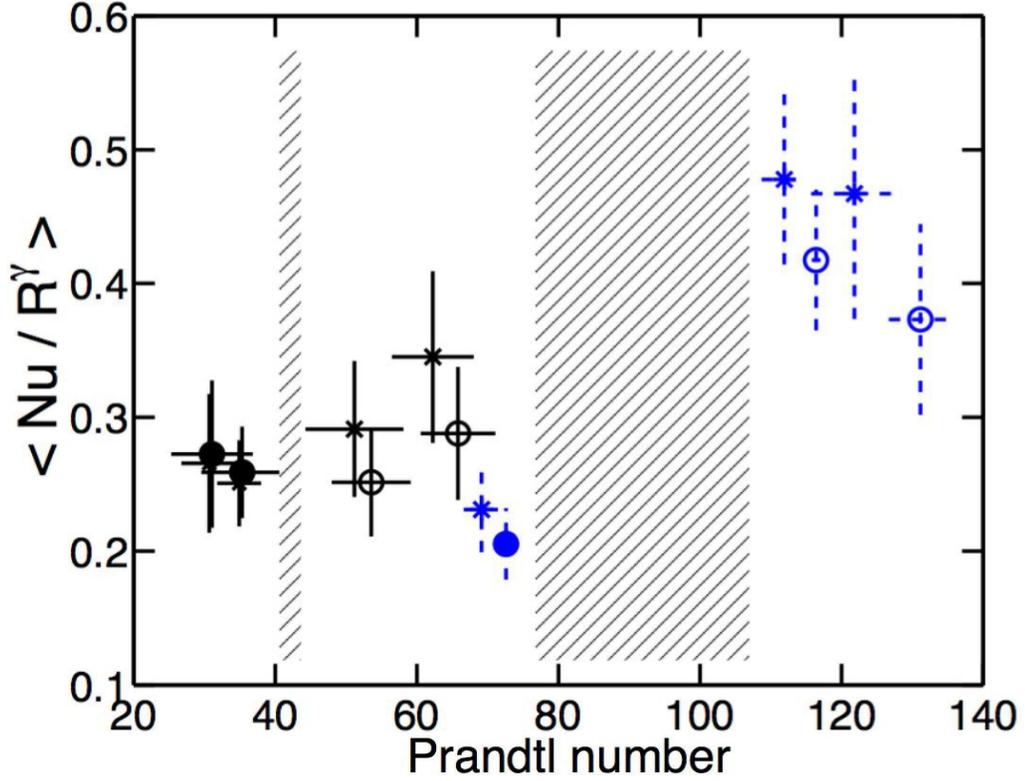
Figure 5.19: Plots of averaged $Nu/\mathcal{R}^\gamma$ vs. $\mathcal{P}$ for $\Gamma = 6.60 \pm 0.05$ (black symbols) and 11.1 ± 0.1 (blue symbols), where γ is taken from the best fit to $Nu \sim \mathcal{R}^\gamma$. Circular symbols $(\circ, \bullet)$ show results obtained by analysis method A, while $(*)$ symbols are obtained by method B. Solid $(\bullet)$ and open $(\circ)$ symbols indicate when the scaling exponent $\gamma \sim 1/4$ $(1/5)$. Note that the crossover between 1/4 and 1/5 exponents occurs at different $\mathcal{P}$ for different aspect ratios Γ, as indicated by the shaded rectangles.

each $\mathcal{P}$, we have averaged the compensated data $Nu\mathcal{R}^{-\gamma}$ over $2 \times 10^4 \le \mathcal{R} \le 10^5$, with γ from the best fit. The data plotted in Fig. 5.19 were obtained from a total of 26 experiments, and results for both analysis methods A (piecewise) and B (linear) for conduction drift approximation are shown.

For a fixed aspect ratio Γ, the data suggest a crossover from one local power law $Nu \sim \mathcal{R}^\gamma$ to another as $\mathcal{P}$ increases. Taking $\Gamma = 6.6$ as an example, the Nu vs. $\mathcal{R}$ scaling for $20 < \mathcal{P} < 40$ gives a γ exponent $\approx 1/4$, while for $50 < \mathcal{P} < 70$, the exponent is $\approx 1/5$. The same indications of a 1/4 to 1/5 crossover of scaling exponents are found for $\Gamma = 11.1$, but for a higher value of $\mathcal{P}$. In the case of $\Gamma = 11.1$, the data

show $\gamma \approx 1/4$ for $70 < \mathcal{P} < 80$ and $\gamma \approx 1/5$ for $100 < \mathcal{P} < 130$. One interpretation of this observation is that the boundaries between different Nu $vs.$ $\mathcal{R}$ scaling regimes depend on the aspect ratio Γ. This has not been previously considered in scaling theories of Rayleigh-Bénard convection, which are specific to the case $\Gamma \sim 1$. In annular electroconvection, we may have to consider a three dimensional parameter space of Nu scaling regimes that depends on $\mathcal{R}$, $\mathcal{P}$ and Γ.

The GL scaling theory applied to annular electroconvection yielded an explicit aspect ratio dependence for the dimensionless charge transport Nu, given by the function $F(\Gamma)$ defined in Eqn. 4.37. Hence, the study of the pure $\mathcal{P}$ effect on the Nu-scaling needs to take the varying aspect ratio into account by dividing the Nu data by the theoretically predicted value of $F(\Gamma)$. Fig. 5.20, shows such a fully compensated plot of $Nu\mathcal{R}^{-\gamma}F^{-1}$ $vs.$ $\mathcal{P}$ for various aspect ratios Γ. The data span $5 \leq \mathcal{P} \leq 250$ and $0.3 \leq \Gamma \leq 17$. All of these data had $\gamma \sim 1/5$. Only a weak dependence on $\mathcal{P}$ remains, amid considerable scatter. A power law fit $\sim \mathcal{P}^{\beta}$ gives $\beta = 0.20 \pm 0.04$ (by the piecewise drift correction method A) or 0.26 ± 0.05 (by the linear drift correction method B). The theoretical prediction is $Nu \propto F(\Gamma)\mathcal{R}^{1/5}\mathcal{P}^{1/5}$ for the regime of low $\mathcal{R}$ and Nu. Thus, the measured value of β is at least consistent with the GL theory applied to annular electroconvection for this specific regime, although the scatter is obviously too large to definitively establish that a power law is present. For the the adjacent regime where $\gamma = 1/4$, the data span less than a decade of $\mathcal{P}$ range, which is insufficient even to look for such consistency.

5.3.3   The dependence of Nu on the aspect-ratio Γ

The scaling theory, described in Chapter 4, Section 4.3.4, explicitly accounts for the aspect ratio dependence, a consideration omitted in the GL theory for turbulent Rayleigh-Bénard convection [32, 33] which only treats the case $\Gamma = 1$. In the formulation of the GL theory for annular electroconvection, the charge trans-
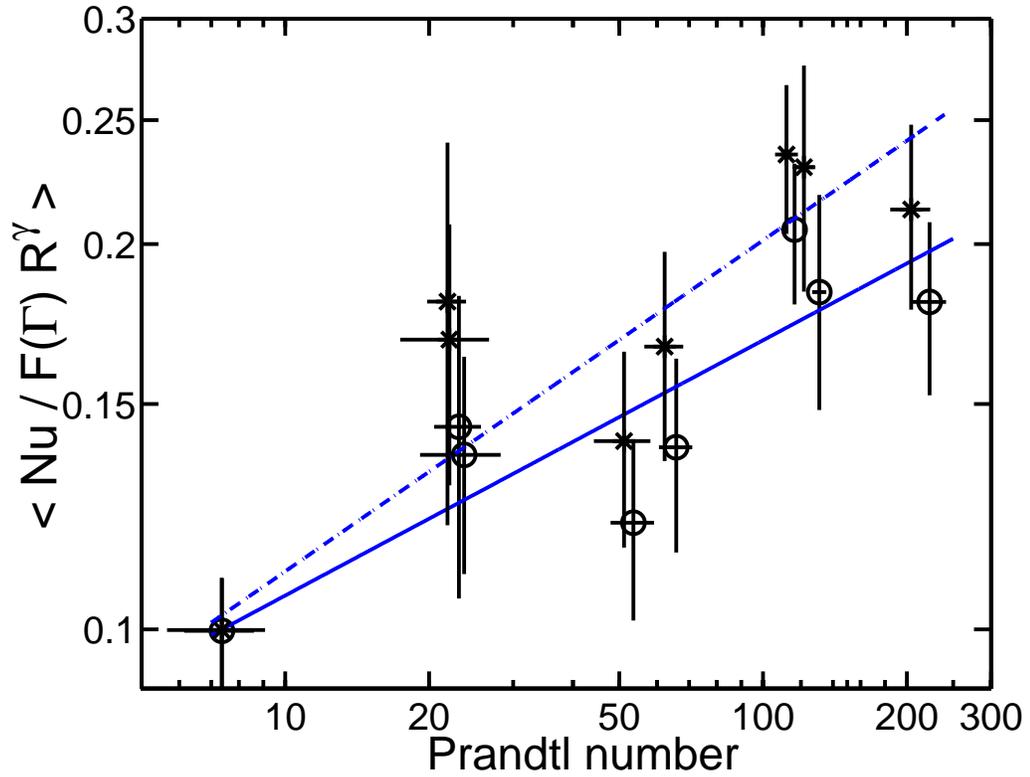
Figure 5.20: The average value of fully compensated $Nu/(\mathrm{F}(\Gamma)\mathcal{R}^{\gamma})$ *vs.* $\mathcal{P}$ on a log-log scale for various Γ. Circular symbols ($\circ$) show results obtained by the drift correction method A, while ($*$) symbols are obtained by the drift correction method B. All of these data had a *Nu vs.* $\mathcal{R}$ scaling exponent of $\gamma \sim 1/5$. The solid (dashed) line is the best fit to $\sim \mathcal{P}^{\beta}$ with $\beta = 0.20$ (0.26), using the drift correction method A (B).

port is modified by an aspect ratio dependent prefactor F(Γ) given by Eqn. 4.37, so that $Nu \propto F(\Gamma)\mathcal{R}^{\gamma}\mathcal{P}^{\beta}$ in the turbulent regime. To make a direct comparison to previous turbulent Rayleigh-Bénard convection experiments, a new function kF is considered; that is F(Γ) multiplied by a normalization constant k, chosen such that kF($\Gamma = 1$) = 1. The appropriate value of k is $\pi/((\pi + 1)\ln(2\pi + 1)) = 0.382$. The function kF(Γ) decreases monotonically with Γ with its greatest variation for $\Gamma < 2$, and is within 2% of its limiting value kF(∞) = 0.764 for $\Gamma > 7$.

The experimental data span the range $0.3 < \Gamma < 17$. Because the data also span the wide range $5 < \mathcal{P} < 250$, some corrections are expected due to changes in the Nu vs. $\mathcal{P}$ scaling, predicted by the theory and also observed in the experiments shown in the preceding section. To separate the aspect ratio dependence of Nu and to compare it with the theoretical prediction $Nu \propto F(\Gamma)\mathcal{R}^{\gamma}\mathcal{P}^{\delta}$, the Nu data are divided by $\mathcal{R}^{\gamma}\mathcal{P}^{\delta}$ and then taken its averaged value over the $\mathcal{R}$ range from 2×10^4 to 10^5. Nu could still depend on Γ independent prefactors which are not captured by a scaling theory. These prefactors can not be separately extracted from the experimental data and may change for the various scaling regimes [33]. To avoid these, the following discussion is restricted to those data for which the Nu vs. $\mathcal{R}$ scaling exponent γ is close to 1/5. The exponents γ is obtained from the power law fits of $Nu \sim \mathcal{R}^{\gamma}$ to the experimental data. We use $\delta = 0.20$ and 0.26 which are obtained by the power law fit of $Nu/(F(\Gamma)\mathcal{R}^{\gamma}) \sim \mathcal{P}^{\delta}$ shown in Fig. 5.20, using the two drift correction methods A and B, as described above. This effectively completes a circle of mutual consistency checks which delivers a self-consistent experimental result for the F(Γ) dependence alone. With one free parameter for all the data, these data are scaled so that F($\Gamma = 1$) = 1, to allow a comparison to similarly normalized Rayleigh-Bénard convection data. The data for six different Γ, obtained from a total of 36 experiments, are in reasonable agreement with the theoretical prediction for kF, as shown in Fig. 5.21. The errors are representative of the scatter in $Nu/\mathcal{R}^{\gamma}\mathcal{P}^{\delta}$ among
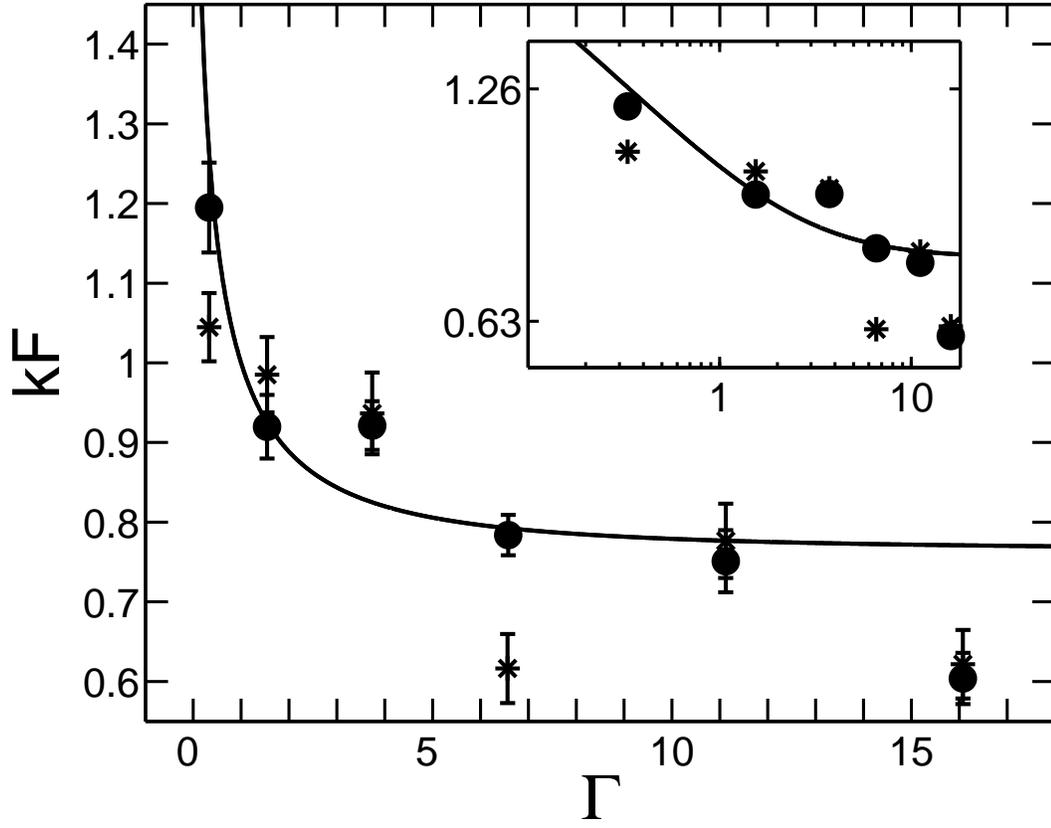
Figure 5.21: Plot of $k\mathrm{F}(\Gamma)$ *vs.* Γ from the scaling theory (solid line), with k chosen so that $k\mathrm{F}(\Gamma = 1)$ is unity. Experimental data for turbulent electroconvection are shown by solid symbols ($\bullet$) by drift correction method A and by ($*$) for method B. The data span $5 \leq \mathcal{P} \leq 250$. The inset shows the same data on a logarithmic scale.

runs for each aspect ratio.

The data at $\Gamma = 6.6$ and 16.1, which deviate most from the theoretical prediction for $k\mathrm{F}$, consist of a few runs which have rather high values of $\mathcal{P}$, about 60 and 220, respectively. This deviation may be due to difficulty of finding the appropriate $\mathcal{P}$ scaling exponent δ. For relatively small $\mathcal{R}$ and high $\mathcal{P}$, scaling theory [33] predicts that Nu becomes independent of $\mathcal{P}$, scaling with $\mathcal{R}^{1/5}\mathcal{P}^0$. It is possible that our few data points with very high $\mathcal{P}$ might fall into the scaling regime $\gamma = 1/5, \quad \delta = 0$ instead of $\gamma = 1/5, \quad \delta = 1/5$, as we have assumed. Thus, the $\mathrm{F}(\Gamma)$ data at $\Gamma = 6.6$ and 16.1 may be significantly underestimated in Fig. 5.21. More experiments with a wider range of parameters would be required to systematically explore the various

scaling regimes, boundaries and crossover effects. To properly investigate these issues, an improved experimental setup (as described in Chapter 6) is required for higher $\mathcal{R}$ forcing and more precise measurements of film conductance for a convecting film.

Data from several turbulent Rayleigh-Bénard convection experiments [29, 98, 99, 100, 101] for various values of Γ are also in broad agreement with the function $k\mathrm{F}(\Gamma)$; Details of this comparison can be found in Ref. [49]. One should only expect the comparison between the aspect ratio dependence for Rayleigh-Bénard convection and the function kF to be reasonable in the limit $\Gamma \to \infty$. Nevertheless, approximate agreement is found between various data, in spite of the difference in geometry, the smaller aspect ratios and the higher range of Rayleigh numbers.

The theoretical predictions using the GL argument are well consistent with the experimental data, which reveal $Nu - \mathcal{R}$ scalings and larger charge transport Nu for smaller aspect ratio Γ for the fixed ranges of $\mathcal{R}$ and $\mathcal{P}$ in the turbulent regime. The next section presents the numerical calculations at high $\mathcal{R}$ numbers, with the main discussions of the geometric effect on the Nu scaling and flow dynamics that is not visualized in experiments. Numerical simulation can avoid the restriction commonly found in most experiments, including Rayleigh-Bénard convection, of merely adjusting one single parameter Γ without varying other parameters, such as $\mathcal{R}$ and $\mathcal{P}$.

5.3.4   Numerical results for flow dynamics and Nu scaling

Previously in Section 5.1, the simulation results for non-sheared convection in the weakly nonlinear regime (for $\mathcal{R} \lesssim 200$) are discussed and compared with previous experimental data and theoretical predictions. In this weakly nonlinear regime, these results of critical onset of convection denoted by $\mathcal{R}_c$, critical mode number m_c, and the nature of primary bifurcation with various parameters show good agreements. Numerical study for annular electroconvection offers some advantages, by presenting the basic local fields and by allowing systematical variations of desired parameters.

The same validated code, as described in detail in Chapter 3, has been extended to simulate electroconvection under high $\mathcal{R}$. In this section, the dynamics of convection patterns and charge distributions—which are not available in experiments—are first shown at various $\mathcal{R}$. Then, the charge transport Nu is discussed as a function of $\mathcal{R}$ for various aspect ratios. Furthermore, the Γ influence on the Nu scaling under high $\mathcal{R} \gtrsim 10^4$ was studied.

Flow dynamics and charge distributions under high $\mathcal{R}$

Fig. 5.22 shows snapshots of streamlines at $\Gamma = 3.10$ and $\mathcal{P} = 10$ for different Rayleigh numbers. As $\mathcal{R}$ is gradually increased, the flow dynamics becomes less ordered and involves more small scales. Fig. 5.22a shows a laminar cellular motion with steady circulation at $\mathcal{R} = 1.5 \times 10^3$ at which the system maintains a reflection symmetry and a rotation symmetry under an angle of $n\pi/2$, where n is an integer. Fig. 5.22b shows that these symmetries are no longer present at higher $\mathcal{R} = 3.8 \times 10^3$ and laminar steady cells in Fig. 5.22a turn to slightly irregular cells with an undulating boundary due to rising positive charged blobs close to the inner electrode. Fig. 5.22c and Fig. 5.22d show more distorted large domain of circulation as well as small scale blobs near the annular boundary, at $\mathcal{R} = 8.1 \times 10^3$ and $\mathcal{R} = 10^4$, respectively. Noticeably, in Fig. 5.22d, there are mainly four pairs of large counter-rotating vortices but sometimes one big circulation consists of two emergent rolls. Even at high $\mathcal{R} = 10^4$, in addition to small-scale vortices close to the annular boundary, the system still maintains large-scale convection patterns. This supports the main assumption of the GL theory— the existence of large scale circulation.

Fig. 5.23–Fig. 5.24 show snapshots of total charge distribution q and flow velocity field at $\Gamma = 3.10$ and $\mathcal{P} = 10$ for the same various $\mathcal{R}$ as in Fig. 5.22. Here, we only show the velocity field for about one-third of grid points so as to generate clear plots. Fig. 5.23a is a steady laminar flow comprising 4 counter-rotating pairs of
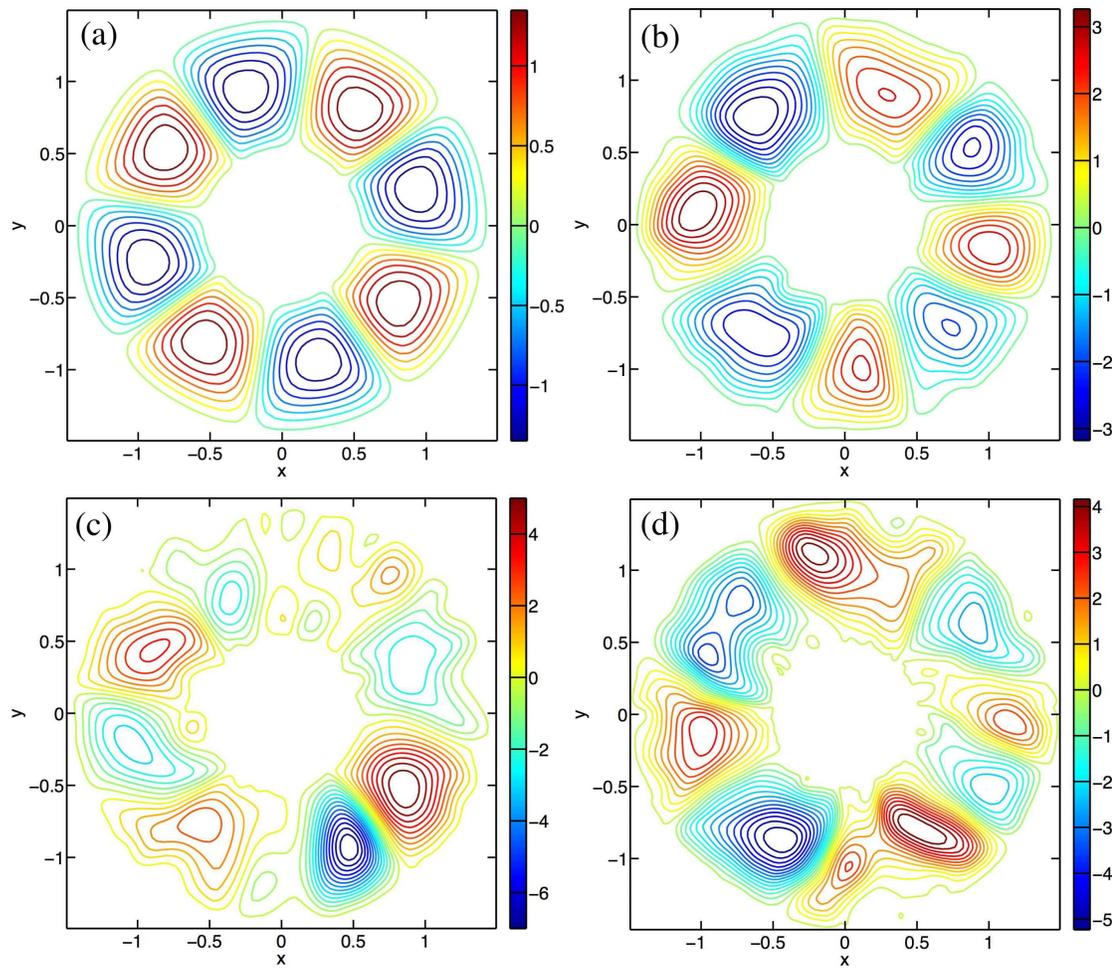
Figure 5.22: Snapshots of iso-streamfunction at $\Gamma = 3.10$ and $\mathcal{P} = 10$ for different high Rayleigh numbers: (a) $\mathcal{R} = 1.5 \times 10^3$ in a laminar steady convection of $m_c = 4$, (b) $\mathcal{R} = 3.8 \times 10^3$, (c) $\mathcal{R} = 8.1 \times 10^3$, and (d) $\mathcal{R} = 10^4$.

positively and negatively charged plumes emitted from the inner electrode and the outer electrode, respectively. Fig. 5.23b shows that at higher $\mathcal{R} = 3.8 \times 10^3$, in addition to the original four plume-like oppositely-charged vortex-pairs, more stalk-like positive and negative charged blobs eject from the annular boundary and these blobs are responsible for a wavy boundary of the streamlines. Fig. 5.24c, presenting the charge and velocity fields at $\mathcal{R} = 8.1 \times 10^3$, illustrates many more tiny plumes of charges emitted from the annular boundary but the overall convection patterns still retains large-scale circulation. Similarly, Fig. 5.24d at $\mathcal{R} = 10^4$ shows that enormous tiny charged blobs around the annular boundary coexist with a few spreading large charged plumes.

The $Nu - \mathcal{R}$ scaling for different aspect ratios

Fig. 5.25 shows simulation results for the charge transport Nu as $\mathcal{R}$ is increased for four different aspect-ratios, with the same $\mathcal{P} = 10$. In an expanded scale, Fig. 5.26 illustrates the simulation results for $Nu - \mathcal{R}$ scaling under higher $\mathcal{R} \gtrsim 10^4$, for the same parameters as in Fig. 5.25. In this figure, we plot a reference power law line, $Nu \sim \mathcal{R}^\gamma$ with the scaling power $1/4$. These numerical calculations of Nu vs. $\mathcal{R}$ in logarithmic scales show their power-law exponents are close to $1/4$, for $3 < \Gamma < 12$ at $\mathcal{P} = 10$. Table 5.3 presents their least squares best fits of $Nu - \mathcal{R}$ scaling for different aspect-ratios. For all these Γ at $\mathcal{P} = 10$, the $Nu - \mathcal{R}$ scaling exponents γ are comparable to 0.25. This $1/4$-scaling exponent is consistent with the experimental results (presented in Section 5.3.1) and the theoretical prediction by the scaling theory (shown in Section 4.3.3).

Fig. 5.27 shows the comparison of the aspect-ratio dependence of $Nu(\Gamma)$ between theoretical prediction and simulation results at three different high-$\mathcal{R}$ numbers. The scaling theory predicts of many local power-laws of $Nu \propto F(\Gamma)\mathcal{R}^\gamma \mathcal{P}^\delta$ with different γ and δ depending on the parameter regime. For $\mathcal{P} = 10$ and in the $\mathcal{R}$-regime of
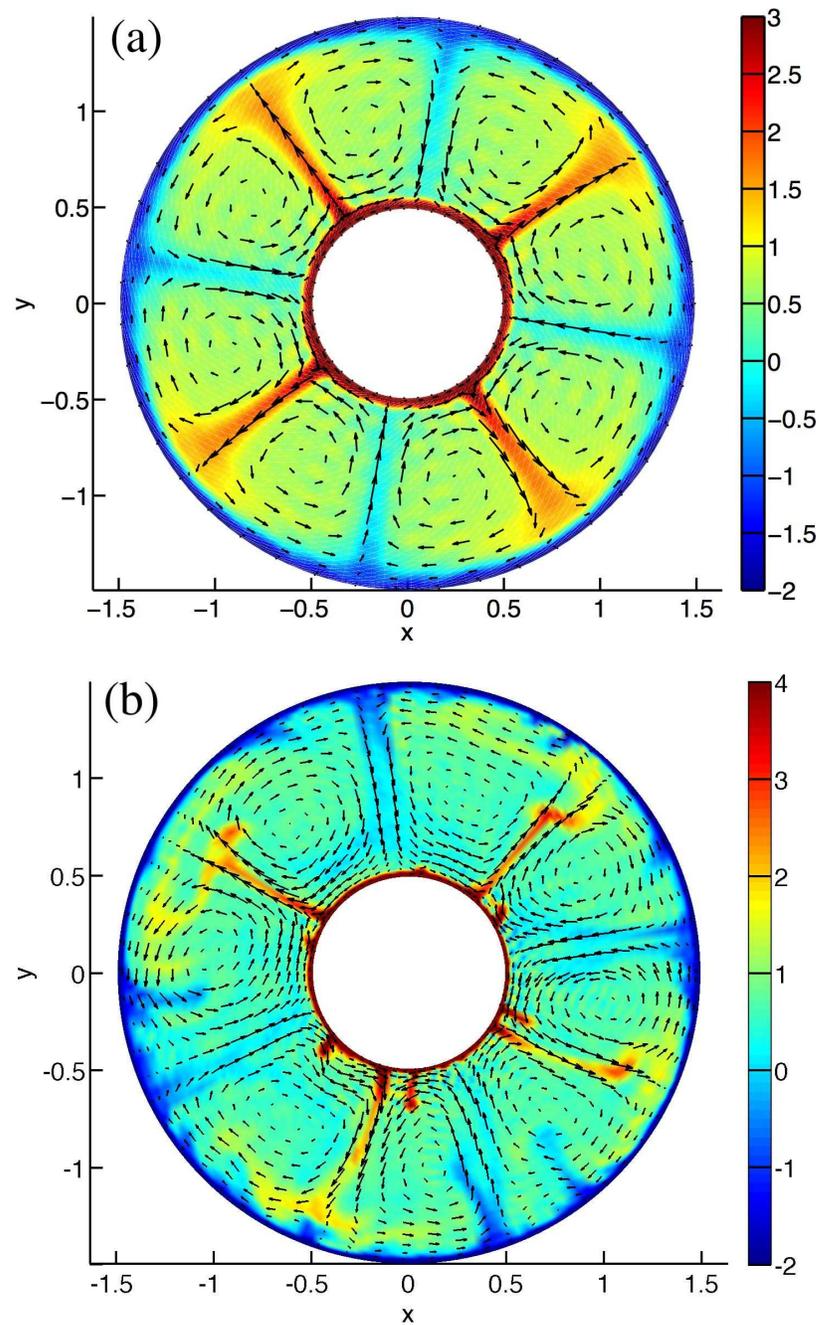
Figure 5.23: Simulation snapshots of total charge (colour) and velocity field (black) at $\Gamma = 3.10$ and $\mathcal{P} = 10$ for different Rayleigh numbers: (a) $\mathcal{R} = 1.5 \times 10^3$, and (b) $\mathcal{R} = 3.8 \times 10^3$.
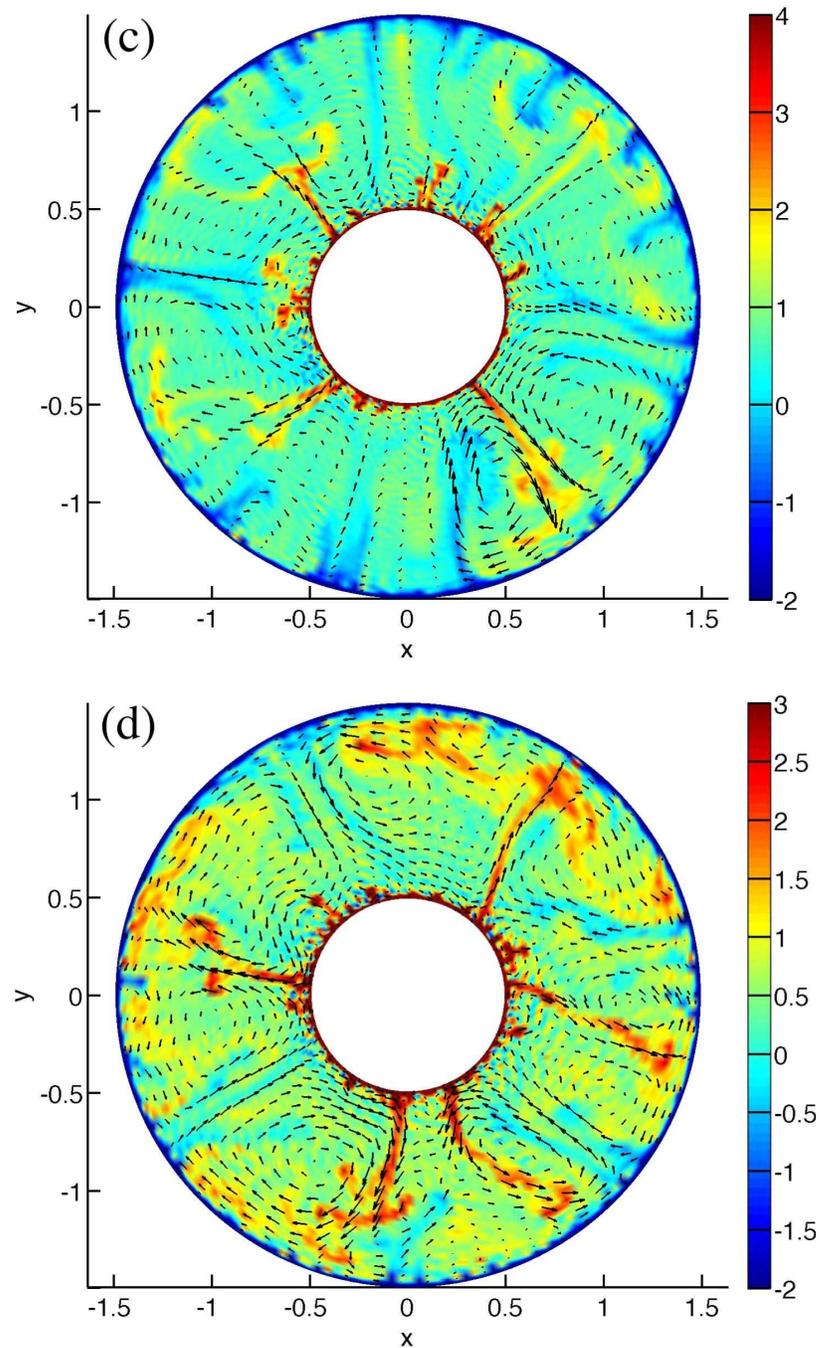
Figure 5.24: Simulation snapshots of the total charge (colour) and the velocity field (black) at $\Gamma = 3.10$ and $\mathcal{P} = 10$, for different high Rayleigh numbers: (c) $\mathcal{R} = 8.1 \times 10^3$, and (d) $\mathcal{R} = 10^4$.
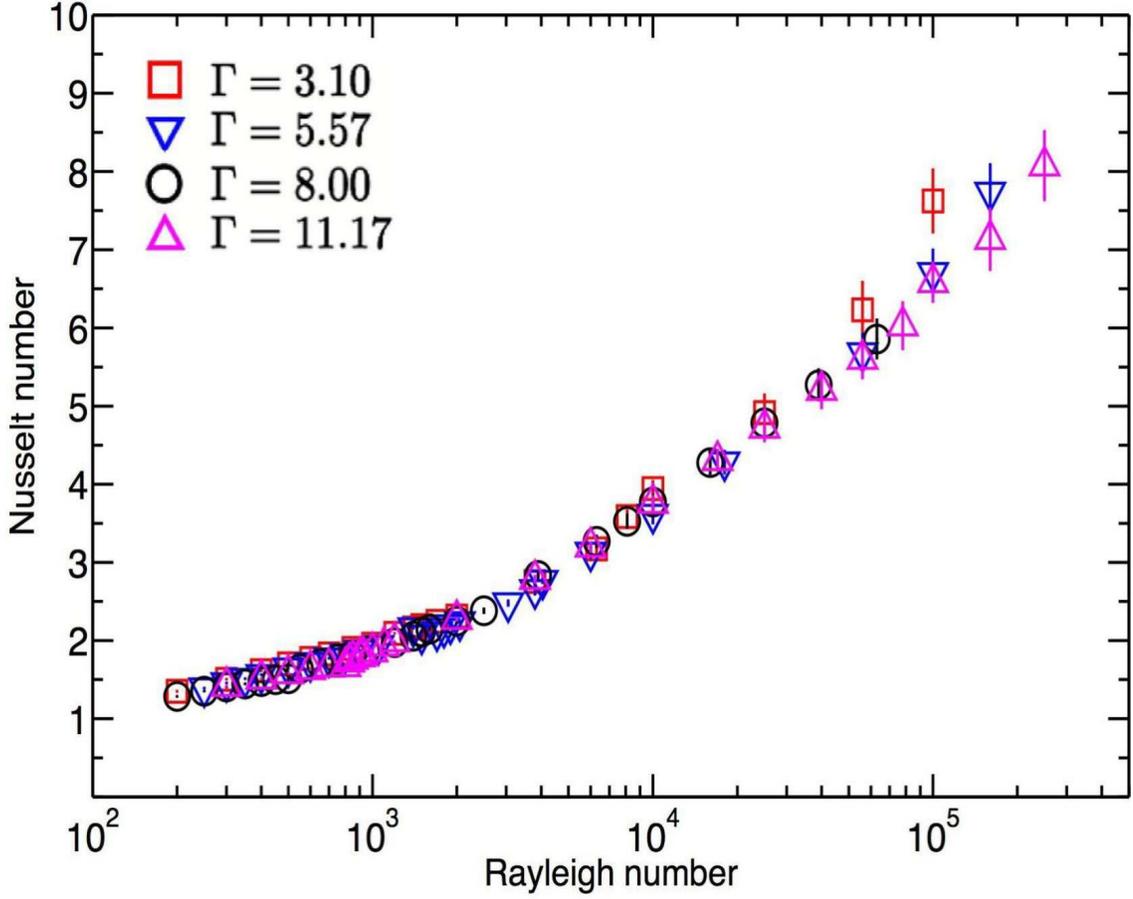
Figure 5.25: Simulation results for the charge transport Nu as $\mathcal{R}$ varies at four different aspect-ratios: $\Gamma = 3.10$ ($\square$), 5.57 ($\triangledown$), 8.00 ($\bigcirc$), and 11.17 ($\triangle$).

Γ	α	$\mathcal{R}_p$	$Nu \sim \mathcal{R}^\gamma$, γ	$\mathcal{R}-$range
5.57	0.47	1700	0.27 ± 0.02	$10^4 - 10^5$
8.00	0.56	1200	0.25 ± 0.02	$10^4 - 6.3 \times 10^4$
11.17	0.64	850	0.24 ± 0.02	$10^4 - 10^5$

Table 5.3: Table of simulation data for high Rayleigh number convection for various Γ at a fixed $\mathcal{P} = 10$ and $Re = 0$. $\mathcal{R}_p$ is the upper-bound of $\mathcal{R}$ for steady laminar convection. The best fits of $Nu \sim \mathcal{R}^\gamma$ and the fitted $\mathcal{R}$ ranges are shown.
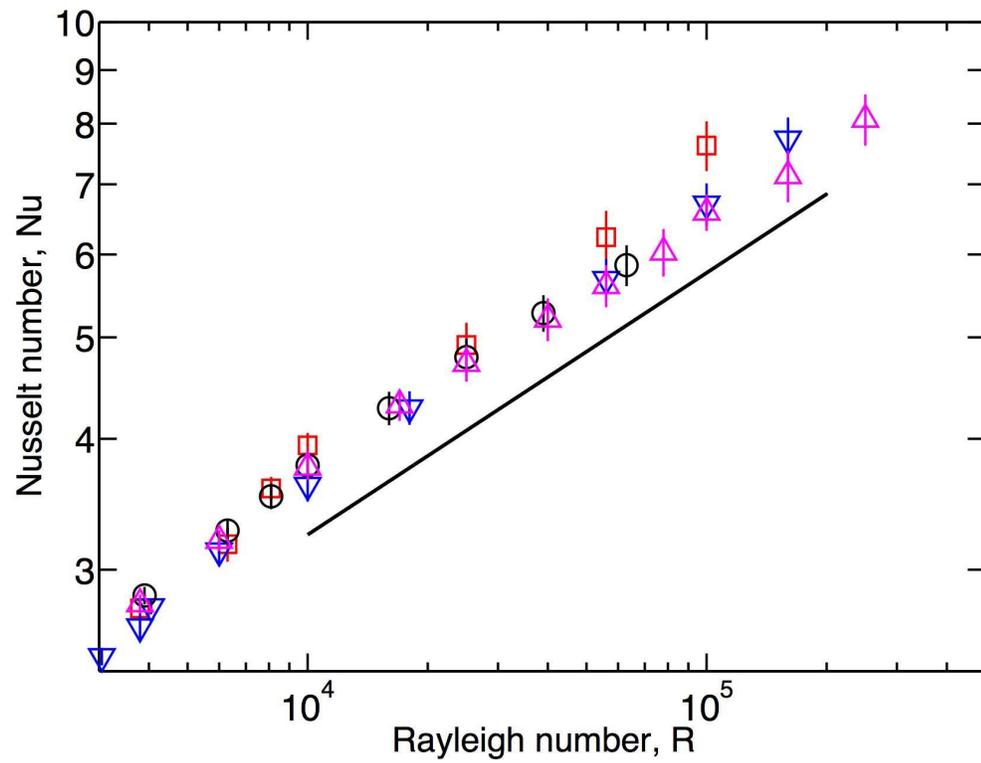
Figure 5.26: Simulation results for $Nu - \mathcal{R}$ scalings, shown by a loglog plot of Nu vs. $\mathcal{R}$ at high $\mathcal{R}$ numbers, for four different aspect-ratios: $\Gamma = 3.10$ ($\square$), 5.57 ($\triangledown$), 8.00 ($\bigcirc$), and 11.17 ($\triangle$). The solid reference line in the figure has a slope of $1/4$ as the scaling power.
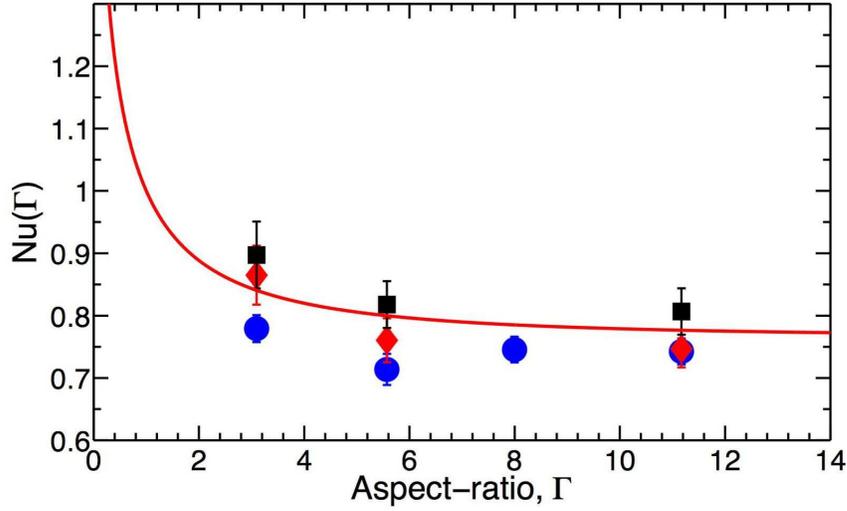
Figure 5.27: Plots of aspect ratio dependence of the charge transport $Nu(\Gamma)$. The solid line is the theoretical prediction of $kF(\Gamma)$ obtained by the scaling theory, fully described in Chapter 4, Section 4.3.4. Simulation results for different high-$\mathcal{R}$ numbers in the turbulent regime are shown by the following symbols: $\mathcal{R} = 10^4$ ($\bigcirc$), $\mathcal{R} = 5.6 \times 10^4$ ($\square$), and $\mathcal{R} = 10^5$ ($\diamondsuit$).

$10^4 - 10^5$, the simulation results of $Nu - \mathcal{R}$ scaling exponents γ are approximately $1/4$ for various aspect-ratios, shown in Table 5.3. Thus, if we assume these data points fall into the same scaling regime, then $Nu(\Gamma)$ is simply the comparison of Nu at the same $\mathcal{R}$ for different aspect-ratios Γ, since $\mathcal{P}$ is a fixed constant. Fig. 5.27 presents the data analyzed with the conventional analysis method such that $Nu(\Gamma = 1) = 1$. More simulation data for small $\Gamma < 2$ would be needed to verify the profound impact on Nu when $\Gamma \lesssim 4$, which is predicted by the scaling theory. Unfortunately, the computational cost of small aspect-ratios $\Gamma < 2.5$ is quite high due to a strong restriction on the time-stepping size. This limitation stems from a highly unstable charge configuration for small $\Gamma < 2.5$ in that relatively larger number of positive charges span in $\sim 0.2\,d$ (film width) near the inner electrode. Nevertheless, simulation data, particularly for higher $\mathcal{R} = 5.6 \times 10^4$ and 10^5, show a consistent agreement with the theoretical prediction, in that the flatness or independence of $Nu(\Gamma)$ for $\Gamma > 5$ with a very gentle trend toward an increase of Nu as Γ decreases from 5 and 2.

Chapter 6

Conclusion

2D annular electroconvection is a rich hydrodynamical process where nonlinearity and complexity manifest themselves. Its unique dimensionality and broad range of accessible parameters make electroconvection complementary to traditional thermal convection experiments in the study of pattern-formation and convective turbulence. As the applied voltage, which acts as the main control parameter, is increased, a sequence of nonlinear instabilities, involving symmetry breaking, arise and shape the system *via* various bifurcations to new emergent states. This thesis work addresses many unsolved and unexplored problems in turbulent convection and in sheared electroconvection and answers these questions by combining experimental, numerical, and theoretical techniques.

The important contributions of this thesis research include the first numerical simulation of 2D annular smectic electroconvection, the first experimental investigation of global charge transport in a liquid crystal film undergoing convective turbulence, and a new theoretical treatment of the charge transport scaling in the turbulent regime, including its aspect ratio dependence. The simulation code was developed from scratch and was validated by benchmarking the critical Rayleigh and mode numbers against previous theoretical and experimental results. Good agreement was

found between these results. The numerical simulation is a crucial new approach for research in smectic electroconvection because it provides the local electrical and hydrodynamic fields which are important for understanding complex nonlinear states of electroconvection. No fluid visualization is available in experiments. The numerical study extends from laminar convection involving ordered pattern-formation, to sheared convection displaying unexpected new bifurcations, and ultimately to turbulent convection under high forcing. These studies considered the impacts of various parameters, such as Prandtl and Rayleigh numbers, the aspect ratio, and the strength of the imposed steady shear. A smectic experiment under a large applied voltage was conducted and the current-voltage scaling in the turbulent regime was observed for the first time. Then, a series of experiments were performed to understand the effect of Prandtl number and aspect ratio on the turbulent charge transport. A theory that explains this turbulent charge transport scaling was established, in a similar manner to the Grossmann-Lohse theory which models the heat transport scaling in turbulent Rayleigh-Bénard convection of unit aspect ratio. The charge transport scaling theory was extended to take into account the aspect ratio dependence and annular geometry of turbulent electroconvection. Experimental, numerical, and theoretical results for turbulent electroconvection are in reasonable agreement with one another. In the following, these results are highlighted and a brief discussion of their implications is given, as well as some opportunities for future research.

Numerical results showed that the annular geometry, characterized by the radius ratio, strongly influences the critical forcing for the onset of convection $\mathcal{R}_c$ and the critical dominant mode m_c. These simulation results of $\mathcal{R}_c$ and m_c are in good agreement with previous experimental data and theoretical predictions. The radius ratio predetermines the base state of the electric field and charge distribution and thus plays a vital role in the pattern selection. The numerical results also revealed that the primary bifurcation in non-sheared electroconvection is supercritical or continuous,

consistent with previous linear stability analyses and most experimental results.

The Prantdl number $\mathcal{P}$ has no influence on the onset of convection but a very moderate impact on the pattern selection with no imposed azimuthal shear. The base state of non-sheared electroconvection is a quiescent flow and $\mathcal{P}$ physically plays no role in the onset of convection. In the weakly nonlinear regime, large $\mathcal{P}$ is a weak parameter; the cubic nonlinearity $g \approx 2$ is nearly constant for $10^{-1} < \mathcal{P} < 10^3$ and increases by a factor of ~ 2 for smaller $\mathcal{P} = 0.01$. In contrast, sheared electroconvection displays a steady Couette laminar flow, and thus $\mathcal{P}$ affects the flow dynamics at the onset and the rotating convection patterns beyond $\mathcal{R}_c$.

The annular geometry allows numerous codimensional-two (CoD2) points where two adjacent azimuthal critical modes are simultaneously unstable. The flow dynamics near a CoD2 point, reached by selecting a specific radius ratio α under zero shear, was investigated for the first time by numerical means. The stable mixed-mode state with Z_2 symmetry which had been predicted by bifurcation theory was not observed. The final steady electroconvection patterns were sensitive to initial conditions and displayed a D_m symmetry.

An imposed azimuthal shear, which introduces some new nonlinear advection terms in the dynamical equations for vorticity and charge density, suppresses the onset of convection. The critical mode m_c at the onset shifts to a smaller value $m_c \leq m_c^0$, where m_c^0 corresponds to the non-sheared case. The applied Couette flow elongates or stretches the convecting vortices, an effect which is very obvious from movies of the simulation results.

Numerical results show supercritical primary bifurcation for sheared convection, in contrast to previous experimental results which were analyzed using IV data alone. Previous experimental observations seemed to show that a large shear could drive the primary bifurcation to become subcritical. The numerical results show clearly that these subcritical bifurcations, which involve a mode change and increase charge

transport, actually take place after the primary bifurcation, and dramatically alter the mode structure of the convection patterns. At these discontinuous transitions, the interaction and competition of a broad band of azimuthal modes profoundly changes the number of counter-rotating vortex pairs in the convection pattern. After the bifurcation, often only one or two azimuthally rotating vortex pairs remain. This phenomenon was not known before from IV measurements alone. Under a moderate shear, oscillatory motions can set in and lead to undulating convection amplitudes in addition to the overall rotation of the pattern, which is due to the global shear. Consistent with this, previous experimental results showed some undulations in time-series data for the electric current. However, the dynamics of the time series was not the main focus of the previous study. The new numerical findings of oscillations therefore suggest a large number of possible future experimental studies. Furthermore, a route to chaos of the Ruelle-Takens-Newhouse type was found in sheared convection. This new finding implies that smectic electroconvection reaches a chaotic state after only a few bifurcations. Future experiments could look for these interesting quasi-periodic and chaotic states.

Experimental IV measurements at high forcing $10^4 \lesssim \mathcal{R} \lesssim 2 \times 10^5$ reveal power laws in the charge transport, so that $Nu \sim \mathcal{R}^\gamma$. The scaling exponents γ are close to 1/4 and 1/5. These experimental results agree with the scaling law prediction which was developed by adapting the Grossmann-Lohse treatment for turbulent Rayleigh-Bénard convection to annular electroconvection, for the parameter space of relatively small $\mathcal{R}$ in the turbulent regime. In agreement with these results, the numerical calculations of $Nu - \mathcal{R}$ scalings show the scaling exponents $\gamma \approx 1/4$ for $\mathcal{P} = 10$, $5 \lesssim \Gamma \lesssim 12$, and $\mathcal{R}$ between 10^4 and 10^5. Furthermore, preliminary experimental results on the effect of $\mathcal{P}$ on the Nu-scalings are consistent with the theoretical prediction of $Nu \sim \mathcal{P}^{1/5}$.

The main feature of our application of the Grossmann-Lohse scaling theory to

annular electroconvection is the aspect ratio dependent prefactor in the scaling-laws, $Nu \propto \mathrm{F}(\Gamma)\mathcal{R}^{\gamma}\mathcal{P}^{\beta}$. Experimental data and simulation results, which showed Γ independence for large $\Gamma > 4$ and an increase of Nu with decreasing $\Gamma < 4$, are consistent with the theoretically calculated $\mathrm{F}(\Gamma)$. These results imply the robustness of the Grossmann-Lohse theory and suggest very similar mechanisms of transport phenomena for 2D and 3D convective turbulence. The findings also suggest that the Grossmann-Lohse theory for turbulent Rayleigh-Bénard convection could be extended to account for the aspect-ratio effects for a confined box and one could possibly construct a fundamental set of Nu-scalings spanning the three dimensional parameter space $(\mathrm{Ra}, \mathrm{Pr}, \Gamma)$.

This thesis suggests several future directions for experiment and simulation on smectic electroconvection. A new electronic design that allows simultaneous measurement of IV data and film conductance could be implemented to improve the experimental accuracy by better accounting for conductivity drift. It would be interesting to explore a broader $\mathcal{P}$ range and a larger $\mathcal{R} > 10^5$ regime. Currently, the highest accessible DC voltage is 1000 volts, but it may still be possible to reach ~ 3000 volts, corresponding to $\mathcal{R} \approx 10^6$, before the dielectric breakdown of the liquid crystal film occurs. The main contribution to the errors in the experiment, especially in the turbulent regime, stems from the drift of the film conductance that is estimated through the IV curve in the conductive regime. The film conductance also affects Nu, $\mathcal{R}$ and $\mathcal{P}$. Thus, it is crucial to accurately determine the film conductance during the course of an experiment. A high-frequency AC voltage superposed on the DC voltage could be used to precisely determine the film conductance, particularly in a convective state. The film conductance could be determined from the high-frequency AC response, while the global charge-transport could be measured under the DC voltage.

The strongest aspect ratio dependence of the charge transport scaling, according

to the scaling theory, is located in the small aspect ratio regime. More simulations with a small aspect ratio $\Gamma < 2$, which will require more computational power, are important to elucidate the form of the Nu scaling and the flow dynamics. The $\Gamma < 2$ flows have only two rotating vortex pairs in the laminar convection regime, but multiscale circulations at higher $\mathcal{R}$ in the turbulent regime.

In the turbulent regime, the current numerical analyses have emphasized the Nu scaling, which is directly related to experimental measurements of electric current. Other analyses using a statistical description of the various local fields could yield additional insight into this 2D convective system. A direct test of the main assumptions entering the GL scaling theory, namely the decomposition of kinetic and electric dissipation rates, could be carried out with simulation data.

The validated simulation code provides some future research opportunities for the study of intriguing physics. For example, the so-called Berry geometrical phase [102, 103] could be identified for the periodic convection pattern. Classical dissipative dynamical systems with continuous symmetries can reveal geometric phases when varying control parameters in a cyclic and adiabatic (very slow) manner, which in turn induces a shift in phase [103]. Similar types of geometry-induced phase shifts appear in quantum-mechanical and classical Hamiltonian systems. However, they have never been experimentally studied in a nonlinear dissipative system. Thus, the code could be modified to investigate this geometric effect, which is manifested as a purely geometric phase shift in the traveling pattern, caused by the adiabatic, cyclic variations of two control parameters, $\mathcal{R}$ and the applied azimuthal shear. Once the correct parameter regime has been identified by simulation, a physical experiment could be performed.

Annular electroconvection exhibits rich nonlinear dynamics and interesting scaling behaviour in the turbulent regime. These were investigated through experiments, theory, and numerical simulations. The thesis work has created new numerical tools,

and explored undiscovered territory in theory and experiment. This has contributed to a better understanding of smectic electroconvection in various nonlinear regimes, and opened up additional opportunities for new and exciting discoveries.

Appendix A

Film thickness determination

The films used contain between tens and few hundred smectic layers, corresponding to thicknesses in the range of 0.06 μm to 0.7 μm. The film thickness is comparable to the wavelength of visible light. In consequence, it can be measured by observing its color under reflection with a known incident light source. The reflected color results from the interference of light reflected from both air-film interfaces (the top and bottom surfaces of the film).

Reflected Intensity

When electromagnetic waves travel through two media, reflection and refraction occur at the interface. The match of the boundary conditions of EM waves at the interface allows one to calculate the reflection and transmission coefficients from Maxwell's equations. In general, the analytic expression for the reflection coefficient for an anisotropic liquid crystal film under an arbitrary incident light beam is complicated. Fortunately, for the smectic A phase, the reflection coefficient of s-polarized light (the polarization is perpendicular to the plane of incidence) has the following simple

form [104]

$$R = \left| \frac{\cos\theta - (n_o^2 - \sin^2\theta)^{1/2}}{\cos\theta + (n_o^2 - \sin^2\theta)^{1/2}} \right|^2,$$

(A-1)

where θ is the incidence angle and n_o is the refractive index normal to the plane of incidence. For smectic A films, the optical axis is perpendicular to the film surface, so n_o is simply the ordinary refractive index.

The intensity of s-polarized light reflected from the thin film with refractive index n_o consisting of N layers is given by [105]

$$I(\lambda, N) = I_o(\lambda) \frac{F \sin^2\phi}{1 + F \sin^2\phi},$$

(A-2)

where

$$F = \frac{4R}{(1-R)^2}, \quad \phi = \frac{2\pi}{\lambda} lN(n_o^2 - \sin^2\theta)^{1/2},$$

(A-3)

$I_o(\lambda)$ is the incident intensity given by the light source, and R is the reflection coefficient described in Eqn. A-1. For 8CB smectic A phase liquid crystal, the layer thickness l is $3.16nm$ and the index of refraction n_o is 1.5375 [37].

Colourimetric Determination

The 1931 Commission Internationale de l'Eclairage (CIE) developed a colourimetric system, a mathematical construction, to specify colour stimuli, human sense, by using tristimulus values for three imaginary primary colours. Tristimulus values are the amounts for each imaginary primary colour which gives any desired colour when additively mixed. Based on experiments, *Colour-matching Functions* were established, where the tristimulus values for individual wavelength of the stimulus for a fixed radiant flux [106]. The CIE 1931 Standard Colourimetric Observer uses the colour matching functions $\bar{x}(\lambda), \bar{y}(\lambda)$ and $\bar{z}(\lambda)$, which can be easily found in colour dynamics

books. For given a colour-stimulus function $\phi(\lambda)$, the tristimulus values X, Y, and Z are

$$X = c \int \phi(\lambda)\bar{x}(\lambda)d\lambda, \quad Y = c \int \phi(\lambda)\bar{y}(\lambda)d\lambda, \quad Z = c \int \phi(\lambda)\bar{z}(\lambda)d\lambda, \quad \text{(A-4)}$$

where c is a normalizing constant. In practice we sum over all colour wavelengths instead of integrating:

$$X = c \sum_{\lambda} \phi(\lambda)\bar{x}(\lambda)\Delta\lambda, \quad etc. \quad \text{(A-5)}$$

Chromaticity Coordinates (x, y, z) are the ratios of each tristimulus value to the sum of the three tristimuli values:

$$x = \frac{X}{X+Y+Z}, \quad y = \frac{Y}{X+Y+Z}, \quad z = \frac{Z}{X+Y+Z}. \quad \text{(A-6)}$$

To specify the chromaticity coordinates of a stimulus is to specify the colour of the stimulus. One can convert any known tristimuli values X, Y, and Z to the well-known color-mapping scheme using three primary colours R, G, B (red, green, and blue) format, with the following transformation [105]:

$$R = +1.1084X + 0.0852Y - 0.1454Z,$$
$$G = -0.0010X + 1.0005Y + 0.0004Z, \quad \text{(A-7)}$$
$$B = -0.0062X + 0.0394Y + 0.8192Z.$$

The main aim here is to determine the chromaticity coordinates of the reflected light from the film. In our experimental conditions, the colour-stimulus function $\phi(\lambda)$ is the spectral intensity $I(\lambda, N)$ in Eqn. A-2 of light reflected from the film. The illuminating light source is a Fostec EKE Tungsten-halogen lamp that operates at a colour temperature of around $3000K$. We assume a black-body radiation spectrum

for the lamp. Hence, the incident light intensity I_o in the Eqn A-2 is

$$I_o(\lambda, T) = \frac{2\pi h c^2}{\lambda^5} \left[\frac{1}{\exp(\frac{hc}{k_B T \lambda}) - 1} \right], \tag{A-8}$$

where h is the Plank constant, k_B is the Boltzmann constant, c is the speed of light, and λ is the wavelength.

The chromaticity coordinates for each N-layer film can be obtained from Eqn. A-6 with the aid of Eqn. A-2. Therefore, the corresponding reflected colour for each N-layer 8CB smectic A film can be read off the CIE colour chart. With this technique, the film's thickness can be determined to within 3 smectic layer spacings, or about $9nm$, when the film's thickness is less than 100 layers, ≈ 0.3 μm thick.

Appendix B

The influence matrix method

In the 2D electroconvection simulation, we have two boundary conditions (BCs) for the streamfunction (its Dirichlet and Neumann BCs) and none for the vorticity. We employed the so-called influence matrix method to solve the problem of doubly-specified boundary conditions. A similar problem arises when solving the Navier-Stokes equations using velocity and pressure as the primitive variables. The pressure field obeys the Poisson equation because the divergence of the velocity is zero at the boundary. In this case, there are two boundary conditions for the velocity field (its value and its divergence) but no condition for the pressure. The influence matrix method was originally introduced for this problem by Kleiser and Schumann [107], and is based on the superposition of specific solutions. Its technique is described in detail below.

In annular electroconvection, the discretization equations for the streamfunction ϕ and vorticity ω at time $k+1$ are described in Chapter 3 , Section 3.3.2 by Eqns. 3.50 and 3.52 or Eqns. 3.54 and 3.55, depending on the time discretization approximations. The no-slip boundary condition for the velocity field doubly specifies the BCs for streamfunction (its values and its derivatives with respect to r) at the inner and outer electrodes, but none for the vorticity field. Written in a more general form, the

time discretization equations for ϕ and ω in terms of Fourier coefficients $\widehat{\omega}_m^{k+1}$, $\widehat{\phi}_m^{k+1}$ are

$$(\mathcal{I} - \Delta\mathcal{L}_{op})\, \widehat{\omega}_m^{k+1} = f, \quad -1 < x < 1, \tag{B-1}$$

$$\mathcal{L}_{op}\widehat{\phi}_m^{k+1} + \widehat{\omega}_m^{k+1} = 0, \quad -1 < x < 1, \tag{B-2}$$

$$\widehat{\phi}_m^{k+1}(r_i) = g_1, \quad \widehat{\phi}_m^{k+1}(r_o) = g_2, \tag{B-3}$$

$$\partial_r\widehat{\phi}_m^{k+1}(r_i) = h_1, \quad \partial_r\widehat{\phi}_m^{'k+1}(r_o) = h_2, \tag{B-4}$$

where $\mathcal{I}$ is the Identity matrix, $\mathcal{L}_{op}$ is the Laplace differential operator defined in Eqn. 3.49, f is a constant calculated with some Fourier coefficients at the earlier time steps k, and Δ is a parameter-dependent constant which depends on the time discretization scheme. For instance, $\Delta = 2\mathcal{P}\Delta t/3$ for the ABBDI2 discretization scheme in Eqn. 3.52, while $\Delta = \mathcal{P}\Delta t$ for the semi-implicit Euler scheme in Eqn. 3.55. The superposition technique in the Influence matrix method allows us to calculate the corresponding boundary conditions for the vorticity field, $\widehat{\omega}_m^{k+1}(r_i) = \zeta_1$, $\widehat{\omega}_m^{k+1}(r_o) = \zeta_2$, in accordance with both Dirichlet and Neumann BCs for the streamfunction in Eqn. 3.37. We decompose the original problem into two sets of equations and look for solutions $(\widehat{\omega}_m^{k+1}, \widehat{\phi}_m^{k+1})$ with the following decomposition:

$$\widehat{\omega}_m^{k+1} = \widetilde{\omega}_m^{k+1} + \bar{\omega}_m^{k+1}, \quad \widehat{\phi}_m^{k+1} = \widetilde{\phi}_m^{k+1} + \bar{\phi}_m^{k+1}. \tag{B-5}$$

One intermittent solution $(\widetilde{\omega}_m^{k+1}, \widetilde{\phi}_m^{k+1})$ satisfies the $\widetilde{P}$-Problem, stated by

$$(\mathcal{I} - \Delta\mathcal{L}_{op})\, \widetilde{\omega}_m^{k+1} = f, \quad -1 < x < 1, \quad \widetilde{\omega}_m^{k+1}(r_i) = 0, \quad \widetilde{\omega}_m^{k+1}(r_o) = 0, \tag{B-6}$$

$$\mathcal{L}_{op}\widetilde{\phi}_m^{k+1} + \widetilde{\omega}_m^{k+1} = 0, \quad -1 < x < 1, \quad \widetilde{\phi}_m^{k+1}(r_i) = g_1, \quad \widetilde{\phi}_m^{k+1}(r_o) = g_2, \tag{B-7}$$

The vorticity field $\widetilde{\omega}_m^{k+1}$ can be first completely solved and then used to calculate the

streamfunction $\widetilde{\phi}_m^{k+1}$.

The other intermittent solution $(\bar{\omega}_m^{k+1}, \bar{\phi}_m^{k+1})$ satisfies the $\bar{P}$-Problem defined by

$$(\mathcal{I} - \Delta\mathcal{L}_{op})\,\bar{\omega}_m^{k+1} = 0, \quad -1 < x < 1, \tag{B-8}$$

$$\mathcal{L}_{op}\bar{\phi}_m^{k+1} + \bar{\omega}_m^{k+1} = 0, \quad -1 < x < 1, \tag{B-9}$$

$$\bar{\phi}_m^{k+1}(r_i) = 0, \quad \bar{\phi}_m^{k+1}(r_o) = 0, \tag{B-10}$$

$$\partial_r\bar{\phi}_m^{k+1}(r_i) = h_1 - \partial_r\widetilde{\phi}_m^{k+1}(r_i), \quad \partial_r\bar{\phi}_m^{k+1}(r_o) = h_2 - \partial_r\widetilde{\phi}_m^{k+1}(r_o). \tag{B-11}$$

The combination of $\tilde{P}$ and $\bar{P}$-problems give the original problem from Eqn. B-1 to Eqn. B-4. The objective here is to calculate the according BCs for vorticity, by solving the $\tilde{P}$-problem first and then the $\bar{P}$-problem.

The $\bar{P}$-Problem can be equivalently transformed into a problem for $(\bar{\omega}_m^{k+1}, \bar{\phi}_m^{k+1})$ where the boundary values $\bar{\omega}$ are determined with the specified Neumann conditions on $\bar{\phi}$. This method introduces the $\bar{P}_0$-Problem:

$$(\mathcal{I} - \Delta\mathcal{L}_{op})\,\bar{\omega}_m^{k+1} = 0, \quad -1 < x < 1, \tag{B-12}$$

$$\mathcal{L}_{op}\bar{\phi}_m^{k+1} + \bar{\omega}_m^{k+1} = 0, \quad -1 < x < 1, \tag{B-13}$$

$$\bar{\phi}_m^{k+1}(r_i) = 0, \quad \bar{\phi}_m^{k+1}(r_o) = 0, \tag{B-14}$$

$$\bar{\omega}_m^{k+1}(r_i) = \zeta_1, \quad \bar{\omega}_m^{k+1}(r_o) = \zeta_2, \tag{B-15}$$

where ζ_1 and ζ_2 have to be calculated according to the Neumann conditions on $\bar{\phi}$ in Eqn. B-11.

The $\bar{P}_0$-Problem is solved by the linear combination

$$\bar{\omega} = \zeta_1\bar{\omega}_1 + \zeta_2\bar{\omega}_2, \quad \bar{\phi} = \zeta_1\bar{\phi}_1 + \zeta_2\bar{\phi}_2, \tag{B-16}$$

where the solutions $(\bar{\omega}_j, \bar{\phi}_j)$, $j = 1, 2$, satisfy the following $\bar{P}_1$ and $\bar{P}_2$-problems as

follows:

$$(\mathcal{I} - \Delta\mathcal{L}_{op})\,\bar{\omega}_{1m}^{k+1} = 0, \quad \bar{\omega}_1(r_i) = 1, \quad \bar{\omega}_1(r_o) = 0, \tag{B-17}$$

$$\mathcal{L}_{op}\bar{\phi}_{1m}^{k+1} = -\bar{\omega}_{1m}^{k+1}, \quad \bar{\phi}_1(r_i) = 0, \quad \bar{\phi}_1(r_o) = 0. \tag{B-18}$$

$$(\mathcal{I} - \Delta\mathcal{L}_{op})\,\bar{\omega}_{2m}^{k+1} = 0, \quad \bar{\omega}_2(r_i) = 0, \quad \bar{\omega}_2(r_o) = 1, \tag{B-19}$$

$$\mathcal{L}_{op}\bar{\phi}_{2m}^{k+1} = -\bar{\omega}_{2m}^{k+1}, \quad \bar{\phi}_2(r_i) = 0, \quad \bar{\phi}_2(r_o) = 0. \tag{B-20}$$

Thus, the Dirichlet BCs for vorticity field ζ_1 and ζ_2 are determined by Eqn. B-11, yielding the algebraic equations:

$$\partial_r\bar{\phi}_{1\,m}^{k+1}(r_i)\zeta_1 + \partial_r\bar{\phi}_{2\,m}^{k+1}(r_i)\zeta_2 = h_1 - \partial_r\widetilde{\phi}_m^{k+1}(r_i), \tag{B-21}$$

$$\partial_r\phi_{1\,m}^{k+1}(r_o)\zeta_1 + \partial_r\bar{\phi}_{2\,m}^{k+1}(r_o)\zeta_2 = h_2 - \partial_r\widetilde{\phi}_m^{k+1}(r_o), \tag{B-22}$$

which can be written $M\Xi = \widetilde{C}$, $\Xi = (\zeta_1, \zeta_2)^T$ and the matrix M is the influence matrix.

The $\bar{P}$-series Problem is time independent, and thus the influence matrix M for each Fourier mode can be calculated first and its inversion can be stored in the preprocessing stage. At each time-cycle, we solve the $\tilde{P}$-Problem in the algorithm and calculate $\widetilde{C}$. Then, we solve for Dirichlet BCs for the vorticity Ξ using $\Xi = M^{-1}\widetilde{C}$. Finally, we solve the original problem with appropriate Dirichlet boundary conditions for both streamfunctions $\widehat{\phi}_m^{k+1}$ and vorticity $\widehat{\omega}_m^{k+1}$ in each Fourier mode and each

collocation points in the radial direction:

$$(\mathcal{I} - \Delta \mathcal{L}_{op})\, \widehat{\omega}_m^{k+1} = f, \tag{B-23}$$

$$\mathcal{L}_{op}\widehat{\phi}_m^{k+1} + \widehat{\omega}_m^{k+1} = 0, \quad -1 < x < 1, \tag{B-24}$$

$$\widehat{\phi}_m^{k+1}(r_i) = g_1, \quad \widehat{\phi}_m^{k+1}(r_o) = g_2, \tag{B-25}$$

$$\widehat{\omega}_m^{k+1}(r_i) = \zeta_1, \quad \widehat{\omega}_m^{k+1}(r_o) = \zeta_2. \tag{B-26}$$

Appendix C

List of symbols

α	Radius ratio
β	The coefficient of thermal expansion
γ	The scaling exponent between Nusselt and Rayleigh numbers
g	The magnitude of the gravitational acceleration
ν	Kinematic viscosity
κ	Thermal diffusivity
L	The height of a convection cell
D	The lateral dimension of a convection cell
Γ	Aspect ratio
ΔT	The temperature difference between the Rayleigh-Bénard convection layers
Ra	The dimensionless Rayleigh number for Rayleigh-Bénard convection (Eqn. 1.1)
Pr	The dimensionless Prandtl number for Rayleigh-Bénard convection (Eqn. 1.1)
Nu	The dimensionless Nusselt number for Rayleigh-Bénard convection (Eqn. 1.1)
$\mathcal{R}$	The dimensionless Rayleigh number for smectic electroconvection
$\mathcal{P}$	The dimensionless Prandtl number for smectic electroconvection
Nu	The dimensionless Nusselt number for smectic electroconvection
J	Heat flux

Re	The Reynolds number based on large scale turbulent circulation
Re	The Reynolds number based on the applied azimuthal shear
I	Electric current
I_c	Electric current due to conduction
V	The applied DC voltage
V_c	The critical applied voltage for the onset of electroconvection
r_i	The radius of the inner electrode
r_o	The radius of the outer electrode
r_i'	The dimensionless form of the inner radius r_i
r_o'	The dimensionless form of the outer radius r_o
d	The film width $d = r_o - r_i$
s	The film thickness
ρ	The mass density of fluid
$\tilde{\rho}$	2D fluid density
η	3D shear viscosity
$\tilde{\eta}$	The 2D shear viscosity of the smectic film
ϵ_0	The permittivity of free space
σ	3D electrical conductivity
$\tilde{\sigma}$	The 2D electrical conductivity of the smectic film
C	The ohmic conductance of the smectic film
$\vec{\mathbf{u}}$	Fluid velocity field
P	Areal pressure
q	Surface charge density
$\vec{\mathbf{E}}$	The electric field in the film plane
ψ	3D electric potential
ψ_2, Ψ	2D electric potential on the film
ϕ	Streamfunction

ω	Vorticity
$\boldsymbol{\omega}$	The rotational frequency applied to the inner electrode
Ω	The dimensionless angular rotational frequency of the inner electrode
$\mathbf{J}$	Electric current density
E_{kin}	Normalized kinetic energy
δ	The Kolmogorov length scale (Eqn. 3.68) or a power-law exponent
m	Azimuthal Fourier mode
m_c	The critical (or most unstable) Fourier mode in the azimuthal direction
ϵ_u	The kinetic dissipation rate of electroconvection
ϵ_ψ	The electric dissipation rate of electroconvection
ϵ_U	The kinetic dissipation rate for Rayleigh-Bénard convection
ϵ_T	The thermal dissipation rate for Rayleigh-Bénard convection
λ_ν	The thickness of viscous boundary layer
λ_T	The thickness of thermal boundary layer
T	Temperature field
$\lambda_{\mathbf{u}}$	The thickness of kinetic boundary layer
λ_ψ	The thickness of electric boundary layer

Bibliography

[1] Z. A. Daya, V. B. Deyirmenjian, and S. W. Morris. Sequential bifurcations in sheared annular electroconvection. *Phys. Rev. E*, 66:015201(R), 2002.

[2] E. Bodenschatz, W. Pesch, and G. Ahlers. Recent developments in Rayleigh-Bénard convection. *Annu. Rev. Fluid Mech.*, 32:709, 2000.

[3] M. C. Cross and P. C. Hohenberg. Pattern formation outside of equilibrium. *Rev. Mod. Phys.*, 65(3):851, 1993.

[4] R. W. Walden, P. Kolodnerl, A. Passner, and C.M. Surko. Traveling waves and chaos in convection in binary fluid mixtures. *Phys. Rev. Lett.*, 55(5):496–499, 1985.

[5] M Bestehorn. Phase and amplitude instabilities for Bénard-Marangoni convection in fluid layers with large aspect ratio. *Phys. Rev. E*, 48(5):3622–3634, 1993.

[6] R. C. DiPrima and H. L. Swinney. Instabilities and transition in flow between concentric rotating cylinders. In H. L. Swinney and J. P. Gollub, editor, *Hydrodynamic instabilities and the transition to turbulence*, page 139. Springer-Verlag, New York, 1981.

[7] A. Buka and L. Kramer, editor. *Pattern formation in liquid crystals*. Springer, 1995.

[8] P. A. Davidson. *Turbulence*. Oxford University Press, 2004.

[9] H. Bénard. Les tourbillons cellulaires dans une nappe liguide. *Rev. Gén. Sci. pures et appl.*, 11:1261–1271 and 1309–1328, 1900.

[10] E. Guyon and I. Mutabazi and J. E. Wesfreid. *Dynamics of spatio-temporal cellular structures: Henri Benard centenary review.* Springer, 2005.

[11] D. J. Tritton. *Physical fluid dynamics.* Oxford, 1988.

[12] F.H. Busse and R. M. Clever. Mechanisms of the onset of time-dependence in thermal convection. In P. A. Tyvand, editor, *Time-dependent nonlinear convection*, page 1. Computational Mechanics Publications, 1998.

[13] J. P. Gollub and S. V. Benson. Many routes to turbulent convection. *J. Fluid Mech.*, 100:449–470, 1980.

[14] F. H. Busse. Transition to turbulence in Rayleigh-Bénard convection. In H. L. Swinney and J. P. Gollub, editor, *Hydrodynamic instabilities and the transition to turbulence*, page 97. Springer-Verlag, New York, 1981.

[15] M. Giglio and S. Musazzi and U. Perini. Transition to chaotic behavior via a reproducible sequence of period-doubling bifurcations. *Phys. Rev. Lett.*, 47:243–246, 1981.

[16] R. P. Behringer, and H. Gao, and J. N. Shaumeyer. Time dependence in Rayleigh-Bénard convection with a variable cylindrical geometry. *Phys. Rev. Lett.*, 50:1199–1202, 1983.

[17] J. Stavans, F. Heslot, and A. Libchaber. Fixed winding number and the quasiperiodic route to chaos in a convective fluid. *Phys. Rev. Lett.*, 55(6), 1985.

[18] J. H. Curry, J. R. Herring, J. Loncaric, and S. A. Orszag. Order and disorder in two- and three-dimensional Bénard convection. *Jour. of Fluid Mech.*, 147:1–38, 1984.

[19] J. P. Eckmann. Roads to turbulence in dissipative dynamical systems. *Rev. Mod. Phys.*, 53:643, 1981.

[20] H. Yahata. Transition to turbulence in the Rayleigh-Bénard convection. *Prog. Theor. Phys*, 68:1070–1081, 1984.

[21] T. Yanagita and K. Kaneko. Rayleigh-Bénard convection: pattern, chaos, spatiotemporal chaos and turbulence. *Physica D*, 82:288, 1995.

[22] A. H. Davis. Natural convective cooling of wires. *Phil. Mag*, 43:329, 1922.

[23] A. H. Davis. Natural convective in cooling in fluids. *Phil. Mag*, 44:920, 1922.

[24] M. V. R. Malkus. The heat transport and spectrum of thermal turbulence. *Proc. R. Soc. Lond. A*, 225:196, 1954.

[25] E. D. Siggia. High Rayleigh number convection. *Annu. Rev. Fluid Mech.*, 26:137–168, 1994.

[26] S. Cioni, S. Siliberto and J. Sommeria. Strongly turbulent Rayleigh-Bénard convection in mercury: comparison with results at moderate Prandtl number. *J. Fluid Mech.*, 35:111–140, 1997.

[27] S. Zaleski. The 2/7 Law in Turbulent Thermal Convection. In P. A. Fox and R. M. Kerr, editor, *Geophysical and Astrophysical Convection*. Gordon and Breach Science Publishers, 1998.

[28] L. P. Kadanoff. Turbulent heat flow: structures and scaling. *Physics Today*, 54:8, 2001.

[29] X. Xu, K.M.S. Bajaj, and G. Ahlers. Heat transport in turbulent rayleigh-bénard convection. *Phys. Rev. Lett*, 84:4357, 2000.

[30] B. Castaing, G. Gunaratne, F. Heslot, L. Kadanoff, A. Libchaber, S. Thomae, X. Z. Wu, S. Zaleski, and G. Zanetti. Scaling of hard thermal turbulence in Rayleigh-Bénard convection. *J. Fluid Mech.*, 204, 1989.

[31] B. I. Shraiman and E. D. Siggia. Heat transport in high rayleigh number convection. *Phys. Rev. A*, 42:R3650, 1990.

[32] S. Grossman and D. Lohse. Scaling in thermal convection: a unifying theory. *J. Fluid Mech.*, 407:27, 2000.

[33] S. Grossman and D. Lohse. Thermal convection for large prandtl numbers. *Phys. Rev. Lett.*, 86:3316, 2001.

[34] S. W. Morris, J. R. de Bruyn, and A. D. May. Electroconvection in a freely suspended film of Smectic-A liquid crystal. *Phys. Rev. Lett.*, 65:2378, 1990.

[35] Zahir Daya. *Electroconvection in suspended fluid film*. MSc. thesis, Dept. of Physics, University of Toronto, 1996.

[36] V. B. Deyirmenjian, Z. A. Daya, and S. W. Morris. Electroconvection in a suspended fluid film: a linear stability analysis. *Phys. Rev. E*, 56:1706, 1997.

[37] Zahir Daya. *Electroconvection in sheared annular fluid film.* PhD thesis, Dept. of Physics, University of Toronto, 2000.

[38] Z. A. Daya, V. B. Deyirmenjian, and S. W. Morris. Electrically driven convection in a thin annular film undergoing circular Couette flow. *Phys. Fluids*, 11:3613, 1999.

[39] P. M Chaikin and T. C. Lubensky. *Principles of condensed matter physics.* Cambridge University Press, 1995.

[40] P.G. De Gennes and J. Prost. *The physics of liquid crystals 2nd ed.* Oxford University Press–New York, 1993.

[41] N. Matsuhashi, M. Kimura, T. Akahane and M. Yoshida. Structure analysis of 8CB liquid-crystalline free-standing film by molecular dynamics simulation. *Advances in Technology of Materials and Materials Processing*, 8:166–171, 2006.

[42] BHD Limited, Broom Road, Poole, England BH12 4NN.

[43] S. Barret, F. Gaspard, R. Herino, and F. Mondon. Dynamic scattering in nematic liquid crystals under dc condition. I. Basic electrochemical analysis. *J. Applied Physics*, 47:2375, 1976.

[44] R. Cocco, F. Gaspard and R. Herino. Study of the control of electrode reactions in a nematic liquid crystal. *J. Chim. Phys. (Paris)*, 76:383, 1979.

[45] S. Barret, F. Gaspard, R. Herino, and F. Mondon. Dynamic scattering in nematic liquid crystals under dc condition. II. Monitoring of electrode processes and lifetime investigation. *J. Applied Physics*, 47:2378–2380, 1976.

[46] A. J. Leadbetter, J. C. Frost, J. P. Gaughan, G. W. Gray and A. Mosly. The structure of smectic A phases of compounds with cyano end groups. *J. Phys. (Paris)*, 40:375, 1979.

[47] W. G. Drisoll. *Handbook of Optics.* McGraw-Hill, New York, 1978.

[48] A. Nemcsics. *Colour Dynamics.* Ellis Horwood, New York, 1993.

[49] P. Tsai, Z. A. Daya, and S. W. Morris. Aspect ratio dependence of charge transport in turbulent convection. *Phys. Rev. Lett.*, 92:084503, 2004.

[50] D. A. Dunmur, M. R. Manterfield, W. H. Miller and J. K. Dunleavy. The dielectric and optical properties of the homologous series of Cyano-Alkyl-Biphenyl Liquid Crystals. *Mol. Cryst. Liq. Cryst.*, 45:127, 1978.

[51] Z. A. Daya, S. W. Morris, and J. R. de Bruyn. Electroconvection in a suspended fluid film: a linear stability analysis. *Phys. Rev. E*, 55:2682, 1997.

[52] Z. A. Daya V. B. Deyirmenjian S. W. Morris J. R. de Bruyn. Annular electroconvection with shear. *Phys. Rev. Lett.*, 80:964, 1998.

[53] S. S. Mao, J. R. de Bruyn, and S. W. Morris. Electroconvection patterns in Smectic films at and above onset. *Physica A*, 239:189, 1997.

[54] Z. A. Daya, V. B. Deyirmenjian, and S. W. Morris. Bifurcations in annular electroconvection with an imposed shear. *Phys. Rev. E*, 64:036212, 2001.

[55] V. B. Deyirmenjian, Z. A. Daya and S. W. Morris. Codimension-two points in annular electroconvection as a function of aspect ratio. *Phys. Rev. E*, 72:036211, 2005.

[56] P. Tsai, Z. A. Daya and S. W. Morris. Charge Transport Scalings in Turbulent Electroconvection. *Phys. Rev. E*, 72:046311, 2005.

[57] U. M. Ascher, S. J. Ruuth, and B. T. R. Wetton. Implicit-Explicit Methods for Time-Dependent Partial Differential Equations. *SIAM Journal on Numerical Analysis*, 32(3):797–823, 1995.

[58] L.S. Tuckerman, and D. Barkley. Bifurcation Analysis for Timesteppers. In E. Doedel, L.S. Tuckerman, editor, *Numerical Methods for Bifurcation Problems and Large-scale Dynamical Systems*, page 435. Springer, 2000.

[59] R. Peyret. *Spectral Methods for Incompressible Viscous Flow*. Springer, 2002.

[60] L. N. Trefethen. *Spectral Methods in Matlab*. Society of Industrial and Applied Mathematics (SIAM), 2000.

[61] J. D. Jackson. *Classical electrodynamics*. John Wiley and Sons, INC., 3rd ed. edition, 1998.

[62] U. Frisch. *Turbulence*. Cambridge University Press, 1995.

[63] G. Grőtzbach. Spatial resolution requirements for direct numerical simulation of the Rayleigh-Bénard convection. *J. Comput. Phys.*, 49:241–264, 1983.

[64] I. S. Aranson and L. Kramer. The world of the complex Ginzburg-Landau equation. *Rev. Mod. Phys.*, 74:99, 2002.

[65] R. Tredicce, G. L. Lippi, P. Mandel, B. Charasse, A. Chevalier, and B. Picque. Critical Slowing Down at a Bifurcation. *Am. J. Phys.*, 72(6):799–809, 2004.

[66] R. Krishnamurti and L. N. Howard. Large scale flow generation in turbulent convection. *Proc. Natl Acad. Sci*, 78:1981–1985, 1981.

[67] G. Zocchi, E. Moses, and A. Libchaber. Coherent structures in turbulent convection: an experimental study. *Physica A*, 166:387–407, 1990.

[68] A. Belmonte, A. Tilgner, and A. Libchaber. Boundary layer length scales in thermal turbulence. *Phys. Rev. Lett.*, 70:4067–4070, 1993.

[69] A. Belmonte, A. Tilgner, and A. Libchaber. Temperature an velocity boundary layers in turbulence convection. *PRE*, 50:269–279, 1994.

[70] X.-L. Qiu and P. Tong. Large-scale velocity structures in turbulent thermal convection. *Phys. Rev. E*, 64(3):036304, 2001.

[71] L. D. Landau and E. M. Lifshitz. *Fluid mechanics*. Pergamon, 1987.

[72] H. T. Rossby. A study of Bénard convection with and without rotation. *J. Fluid Mech.*, 36:309–335, 1969.

[73] S. Horanyi and L. Krebs, and U. Műller. Turbulent Rayleigh-Bénard convection in low Prandtl number fluids. *Intl J. Heat Mass Transfer*, 42:3983–4003, 1999.

[74] F. Heslot, B. Castaing, and A. Libchaber. Transitions to turbulence in helium gas. *Phys. Rev. A*, 36:5870, 1987.

[75] J. Werne, E. E. DeLuca, R. Rosner, and F. Cattaneo. Development of hard-turbulent convection in two dimensions: Numerical evidence. *Phys. Rev. Lett.*, 67(25):3519, 1991.

[76] R. H. Kraichnan. Turbulent thermal convection at arbitrary prandtl number. *Phys. Fluids*, 5, 1962.

[77] X. Chavanne, F. Chilla, B. Castaing, B. Hebral, B. Chabaud, and J. Chaussy. Observation of the ultimate regime in Rayleigh-Bénard convection. *Phys. Rev. Lett.*, 79, 1997.

[78] K.-Q. Xia, S. Lam, and S.-Q Zhou. Heat-flux measurement in high-Prandtl-number turbulent Rayleigh-Bénard convection. *Phys. Rev. Lett*, 88:064501, 2002.

[79] G. Ahlers and X. Xu. Prandtl-number dependence of heat transport in turbulent Rayleigh-Bénard convection. *Phys. Rev. Lett*, 86:3320, 2001.

[80] R. Verzicco & R. Camussi. Numerical experiments on strongly turbulent thermal convection in a slender cylindrical cell. *J. Fluid Mech.*, 477:19–49, 2003.

[81] A. Alonso, M. Net, and E. Knobloch. On the transition to columnar convection. *Phys. Fluids*, 7, 1995.

[82] M. Lesieur. *Turbulence in fluids.* Kluwer, Dordrecht, 1990.

[83] S. Kenjereš and K. Hanjalić. Convective rolls and heat transfer in finite-length Rayleigh-Bénard convection: A two-dimensional numerical study. *Phys. Rev. E*, 62:7987, 2000.

[84] P. Tsai, Z. A. Daya, V. B. Deyirmenjian, and S. W. Morris. Direct numerical simulation of supercritical annular electroconvection. *Phys. Rev. E*, 76:026305, 2007.

[85] W. F. Langford, and D. D. Rusu. Pattern formation in annular convection. *Physica A*, 261:188, 1998.

[86] S. H. Strogatz. *Nonlinear dynamics and chaos.* Addison-Wesley publishing company, 1994.

[87] F. H. Busse. The sequence-of-bifurcations Approach towards understanding turbulent fluid flow. *Surveys in Geophysics*, 24(3):269, 2003.

[88] R. Braun, F. Feudel, and P. Guzdar. Route to chaos for a two-dimensional externally driven flow. *Phys. Rev. E*, 58(2):1927, 1998.

[89] F. Feudel and N. Seehafer. Bifurcations and pattern formation in a two-dimensional navier-stokes fluid. *Phys. Rev. E*, 52(4):3506–3511, 1995.

[90] D. Molenaar, H.J.H. Clercx, and G.J.G. van Heijst. Transition to chaos in a confined two-dimensional fluid flow. *PRL*, 95, 2005.

[91] J. Sommeria. Experimental study of the two-dimensional inverse energy cascade in a square box. *J. Fluid Mech.*, 170, 1986.

[92] S. Newhouse, D. Ruelle, and F. Takens. Occurrence of strange axiomA attractors near quasi periodic flows on T^m, $m \leq 3$. *Commun. Math. Phys.*, 64:35–40, 1978.

[93] D. Ruelle and F. Takens. On the nature of turbulence. *Commun. Math. Phys.*, 20:167–192, 1970.

[94] H. D. I. Abarbanel. *Analysis of observed chaotic data*. Springer, 1995.

[95] H. G. Schuster and W. Just. *Deterministic chaos: an introduction*. Wiley-VCH, 2005.

[96] M. J. Feigenbaum. The transition to aperiodic behavior in turbulent systems. *Comm. Math. Phys.*, 77:65, 1980.

[97] P. Manneville and Y. Pomeau. Intermittency and the Lorenz Model. *Phys. Lett*, 75 A:1, 1979.

[98] G. Ahlers. Effect of sidewall conductance on heat-transport measurements for turbulent Rayleigh-Bnard convection. *Phys. Rev. E*, 63:015303(R), 2000.

[99] J. J. Niemala, L. Skrbek, K. R. Sreenivasan and R. J. Donnelly. High Rayleigh Number Convection. *Nature*, 404:837, 2000.

[100] J. J. Niemala and K. R. Sreenivasan. Confined turbulent convection. *J. Fluid Mech.*, 481:355–384, 2003.

[101] Y. Shen, P. Tong and K.-Q. Xia. Turbulent convection over rough surfaces. *Phys. Rev. Lett.*, 76:908, 1996.

[102] Alfred Shapere and Frank Wilczek. *Geometric phases in physics*. World Scientific, 1989.

[103] A. S. Landsberg. Geometrical phases and symmetries in dissipative systems. *Phys. Rev. Lett.*, 69(6):865–868, 1992.

[104] E. B. Sirota et al. X-ray and optical studies of the thickness dependence of phase diagram of liquid crystal films. *Phys. Rev. A*, 36:2890, 1987.

[105] M. Born and E. Wolf. *Principles of Optical.* Pergamon Oxford, 1975.

[106] R. Feynman. *The Feynman lectures of physics Vol.1.* Addison-Wesley, 1977.

[107] E. H. Hirschel, editor. *Third GAMM conference numerical methods in fluid mechanics.* Vieweg, Braunschweig, 1980.